TURUN
YLIOPISTO
UNIVERSITY
OF TURKU

SOURCES OF VARIABILITY IN METAL ADDITIVE MANUFACTURING

Effects of machine architecture-defined process parameters in PBF-LB AM

Joni Reijonen

TURUN YLIOPISTON JULKAISUJA – ANNALES UNIVERSITATIS TURKUENSIS
SARJA – SER. F OSA – TOM. 50 | TECHNICA – INFORMATICA | TURKU 2024

TURUN
YLIOPISTO
UNIVERSITY
OF TURKU

SOURCES OF VARIABILITY IN METAL ADDITIVE MANUFACTURING

Effects of machine architecture-defined process parameters in PBF-LB AM

Joni Reijonen

TURUN YLIOPISTON JULKAISUJA – ANNALES UNIVERSITATIS TURKUENSIS
SARJA – SER. F OSA – TOM. 50 | TECHNICA – INFORMATICA | TURKU 2024

University of Turku

Faculty of Technology
Department of Mechanical and Materials Engineering
Mechanical Engineering
Doctoral Programme in Technology (DPT)

Supervised by

Professor Antti Salminen
Department of Mechanical and Materials Engineering
University of Turku
Turku, Finland

Dr. Sini Metsä-Kortelainen
DIMECC Oy (VTT Technical Research Centre of Finland Ltd. until 10/2023)
Helsinki, Finland

Dr. Heli Helaakoski
VTT Technical Research Centre of Finland Ltd.
Oulu, Finland

Reviewed by

Assistant Professor Jaime Berez
The University of North Carolina at Charlotte
Charlotte, USA

Professor Johannes Henrich Schleifenbaum
RWTH Aachen University
Aachen, Germany

Opponent

Professor Milan Brandt
Royal Melbourne Institute of Technology
Melbourne, Australia

SBN 978-952-02-0021-3 (PRINT)
ISBN 978-952-02-0022-0 (PDF)
ISSN 2736-9390 (Painettu/Print)
ISSN 2736-9684 (Sähköinen/Online)
Painosalama, Turku, Finland 2024

Dedicated to the advancement of scientific knowledge.

UNIVERSITY OF TURKU
Faculty of Technology
Department of Mechanical and Materials Engineering
Mechanical Engineering
JONI REIJONEN: Sources of variability in metal additive manufacturing: Effects of machine architecture-defined process parameters in PBF-LB AM
Doctoral Dissertation, 174 pp.
Doctoral Programme in Technology (DPT)
December 2024

ABSTRACT

Laser powder bed fusion additive manufacturing (PBF-LB AM) has matured from rapid prototyping into an industrial manufacturing technology used to produce critical end-use parts for demanding applications in the aerospace, nuclear, and other regulated industries. However, the high variability in the mechanical properties of parts produced using PBF-LB AM is a major hindrance to further advancement and wider adoption of this potentially revolutionary manufacturing technology.

The purpose of this dissertation is to identify the root causes of the observed variability in properties of PBF-LB manufactured parts and quantify their impact. This is explored in the context of *machine architecture-defined* process parameters, which have rarely been adequately considered in studies related to PBF-LB material properties. Specifically, the objective is to study the effects of shielding gas flow speed, re-coater blade type, and laser beam focal point position on the quality of PBF-LB manufactured parts. Practical guidance is provided on how these parameters should be considered in additive manufacturing procedure specifications (AMPS) or similar process control approaches aimed at assuring repeatable material properties. Furthermore, the variability in mechanical properties of 316L stainless steel produced using different machines and powders was studied, including exploration of the potential of using standardized post-process heat treatments to reduce variability. Additionally, this thesis presents strategies for in-situ process monitoring for quality assurance purposes.

The results highlight the significant impact of the previously understudied *machine architecture-defined* process parameters on the PBF-LB process. These parameters should be considered essential to the process. Post-processing with hot isostatic pressing reduced variability in most of the studied properties, but at the cost of an associated significant reduction in absolute properties. Co-axial photodiode-based melt pool monitoring and contact-image sensor-based powder bed imaging are effective means of direct and continuous monitoring of the state of the actual fundamental unit processes in the PBF-LB process: the spreading of the powder layer and the selective laser melting of it.

KEYWORDS: Additive manufacturing, laser powder bed fusion, machine architecture, parameters, variability, quality

TURUN YLIOPISTO
Teknillinen tiedekunta
Kone- ja materiaalitekniikan laitos
Konetekniikka
JONI REIJONEN: Vaihtelevuuden lähteet metallien lisäävässä valmistuksessa: koneen arkkitehtuurin määrittämien parametrien vaikutus laser-jauhepetisulatuksessa
Väitöskirja, 174 s.
Teknologian tohtoriohjelma (DPT)
Joulukuu 2024

TIIVISTELMÄ

Laser-jauhepetisulatukseen perustuva lisäävä valmistus on kehittynyt prototyyppien pikavalmistuksesta teolliseksi valmistusteknologiaksi, jota käytetään kriittisten komponenttien tuotantoon vaativissakin sovelluskohteissa esimerkiksi ilmailualalla, ydinvoimateknologiassa ja muilla vastaavilla säännellyillä teollisuuden aloilla. Suuri hajonta valmistettujen kappaleiden mekaanisissa ominaisuuksissa on kuitenkin osoittautunut merkittäväksi haasteeksi tämän valmistavaa teollisuutta mahdollisesti mullistavan valmistusteknologian edistymiselle ja laajemmalle käyttöönotolle.

Tämän väitöskirjan tarkoitus on tunnistaa laatuvaihtelun takana olevat perusilmiöt prosessissa sekä kvantifioida niiden vaikutuksen suuruus valmistettujen kappaleiden ominaisuuksiin. Tätä lähestytään ns. koneen arkkitehtuurin määrittämien parametrien näkökulmasta, joiden vaikutusta prosessiin on tutkittu hyvin vähän ja joiden raportointi aiempien tutkimusten menetelmäkuvauksissa on ollut vaillinaista. Tarkalleen sanottuna, tavoite on selvittää suojakaasun virtauksen, jauheen levittimen tyypin ja lasersäteen polttopisteen paikan vaikutus laser-jauhepetisulatuksella valmistettujen kappaleiden laatuun. Tulokset antavat käytännön ohjeita, kuinka näitä parametreja tulisi käsitellä valmistusohjeissa tai muissa vastaavissa prosessin laadunhallintadokumenteissa. Työssä tutkitaan myös eri konejauhe kombinaatioiden aiheuttamaa hajontaa 316L ruostumattoman teräksen mekaanisissa ominaisuuksissa ja standardoitujen jälkilämpökäsittelyjen mahdollisuuksia hajonnan pienentämiseksi. Lisäksi väitöskirjassa esitetään menetelmiä prosessimonitoroinnin käyttämiseksi laadunvarmistustarkoituksiin.

Tulokset korostavat aiemmin vähän tutkittujen koneen arkkitehtuurin määräämien parametrien merkittävää vaikutusta laser-jauhepetisulatusprosessiin. Tästä syystä niitä tulee käsitellä välttämättöminä parametreina prosessin laadunhallinnassa. Isostaattinen kuumapuristus jälkilämpökäsittelynä vähensi hajontaa useimmissa mitatuissa mekaanisissa ominaisuuksissa, mutta tämä heikensi merkittävästi vastaavien ominaisuuksien absoluuttiarvoja. Koaksiaalinen fotodiodeihin perustuva sulan monitorointi ja kontaktikuvasensoriin perustuva jauhepedin kuvantaminen tarjoavat tehokkaan keinon suoraan ja jatkuvaan laser-jauhepetisulatuksen tärkeimpien yksikköprosessien – jauhekerroksen levityksen ja sen selektiivisen sulatuksen – seurantaan.

ASIASANAT: Hajonta, koneen arkkitehtuuri, laatu, laser-jauhepetisulatus, lisäävä valmistus, parametrit

Table of Contents

Abbreviations

3D	three-dimensional
AM	additive manufacturing
AMPS	additive manufacturing procedure specification
BSD	backscatter detector
CIS	contact image sensor
DAQ	data acquisition
EBSD	electron backscatter diffraction
EDS	energy-dispersive X-ray spectroscopy
EDM	electric-discharge machining
FMO	focus measure operator
HIP	hot isostatic pressing
ICP-OES	inductively coupled plasma-optical emission spectrometry
MPM	melt pool monitoring
Nd:YAG	neodymium-doped yttrium aluminum garnet
OM	optical microscopy
SA	solution annealing
SEM	scanning electron microscopy
SR	stress-relieving
PBF-LB	powder bed fusion-laser beam
PSD	particle size distribution
xCT	x-ray computed tomography

List of symbols and units

α	absorptivity	%
Δf_z	focal shift	mm
$\Delta H/h_s$	normalized enthalpy	-
ΔT	temperature difference	K
λ	wavelength	nm
Θ	divergence angle	mrad
ρ	density	g/cm^3
σ	standard deviation	-

Φ_λ	total radiant flux	W
ω	scanning angle	°
a	laser beam radius	mm
A	elongation at fracture	%
BPP	beam parameter product	mm*mrad
C	specific heat capacity	J/kgK
D	thermal diffusivity	mm^2/s
d_0	laser beam waist diameter	mm
ED	energy density	J/mm^2
f	focal point position	mm
h	hatch distance	mm
L_m	latent heat of melting	kJ/kg
LT	layer thickness	µm
P	laser power	W
p	melt pool penetration	µm
PD	power density	W/mm^2
PD_I	photodiode signal intensity	V
R_m	ultimate tensile strength	MPa
$Rp_{0.2}$	yield strength	Mpa
TED	thermal energy density	-
TED^*	normalized thermal energy density	-
v	scanning speed	mm/s
VED	volumetric energy density	J/mm^3
w	melt pool width	µm
z_R	Rayleigh length	mm

List of Original Publications

This dissertation is based on the following original publications, which are referred to in the text by their Roman numerals:

I **Reijonen, J**., Revuelta, A., Riipinen, T., Ruusuvuori, K., Puukko, P. On the effect of shielding gas flow on porosity and melt pool geometry in laser powder bed fusion additive manufacturing. *Additive Manufacturing*, 2020; 32: 101030.

II **Reijonen, J**., Björkstrand, R., Riipinen, T., Que, Z., Metsä-Kortelainen, S., Salmi, M. Cross-testing laser powder bed fusion production machines and powders: Variability in mechanical properties of heat-treated 316L stainless steel. *Materials & Design*, 2021; 204: 109684.

III **Reijonen, J**., Revuelta, A., Metsä-Kortelainen, S., Salminen, A. Effect of hard and soft re-coater blade on porosity and processability of thin walls and overhangs in laser powder bed fusion additive manufacturing. *The International Journal of Advanced Manufacturing Technology*, 2024; 130: 2283–2296.

IV **Reijonen, J**., Revuelta, A., Metsä-Kortelainen, S., Salminen, A. Effect of laser focal point position on porosity and melt pool geometry in laser powder bed fusion additive manufacturing. *Additive Manufacturing*, 2024; 84: 104180.

Supporting studies

Reijonen, J., Revuelta, A., Nagarajan, H.P.N. Towards data driven quality monitoring: alignment and correlation of photodiode-based co-axial melt pool monitoring signals to part quality in laser powder bed fusion. *IOP Conference Series: Materials Science and Engineering*, 2023; 1296: 012009.

Yang, H., **Reijonen, J**., Revuelta, A. Multiresolution Quality Inspection of Layerwise Builds for Metal 3D Printer and Scanner. *Journal of Manufacturing Science and Engineering,* 2023; 145(1): 101004.

1 Introduction

1.1 Background and motivation

Since its invention in the early 1980s, additive manufacturing (AM) has matured from rapid prototyping into an industrially relevant manufacturing process used in various industries for the production of functional end-use components. The most recent standard for AM terminology identifies seven different technology categories and defines the general principle of AM as the "*process of joining materials to make parts from 3D model data, usually layer upon layer, as opposed to subtractive manufacturing and formative manufacturing methodologies*" [1]. The first AM technology invented was stereolithography (now known as vat-photopolymerization per standard terminology) [2][3]. This technology was limited by definition to the usage of photopolymers as the processed material. The invention by Carl Deckard of the University of Texas at Austin of selective laser sintering [4], an AM technology now more commonly known as powder bed fusion (PBF), extended the processable material groups to other types of technical polymers, ceramics, and even metals. The earliest documented attempts to synthesize 3D objects with selective laser sintering of metal powders using selective laser sintering equipment at the University of Texas at Austin date back to 1989 [5], and the first metallic part (a gear) was made from a powder mixture of copper and tin-lead solder [6].

The next (minor-sounding but fundamental) developmental step in metal AM was the transition from selective laser *sintering* to selective laser *melting* of single-component powders without low melting point binders, patented by Fraunhofer ILT in 1996 [7]. At that time the part densities achievable with this approach were still far from the full density required to reach mechanical properties comparable to conventionally processed structural metals. Nevertheless, the general principle of the process, nowadays known as laser powder bed fusion (PBF-LB), have remained unchanged since then. During the late 1990s and early 2000s the technology was further developed and higher part densities were achieved. A key enabling technology for this was the switch to solid-state infra-red lasers, pioneered at KU Leuven [8]. The change from CO_2 lasers operating at ~10 μm to solid-state lasers operating at a wavelength of ~1 μm significantly increased absorptivity in metals. This, combined with high beam quality focusable to a small focal point and the ever-

increasing output power of the lasers, resulted in the next generation of PBF-LB systems at the turn of the millennium; machines with sufficient energy density to directly melt high melting point structural alloys such as steels and titanium while maintaining practically relevant scanning speeds and achieving solidified part densities of 90–95% [9][10][11]. By 1998 Das et al. [12] were already able to achieve as-built densities of 98.5% with a PBF-LB system with a 250 W neodymium-doped yttrium aluminum garnet (Nd:YAG) laser and high temperature platform pre-heating up to 600°C. They also showed that post-processing with hot isostatic pressing (HIP) allowed the achievement of densities of 99.5% and 99.9% for IN625 and Ti-6Al-4V alloys respectively.

Continued development of PBF-LB technology during the 2000s in the form of new scanning strategies [13], the important transition from Nd:YAG to diode-pumped Ytterbium fiber lasers [14], and other machine improvements such as improved shielding gas flow [15] contributed to the achievement of bulk material densities of over 99% in the as-built condition. Achieving such densities enabled relevant comparisons to the mechanical properties of conventional wrought materials [16][17]. With the possibility of producing nearly fully dense material, the next developments included the application of platform pre-heating to reduce residual stresses [18], the introduction of multi-laser systems [19], and high power laser sources of up to 1 kW to increase productivity [20]. Simultaneously the processable material palette was widened to encompass a variety of structural materials such as steels, titanium, aluminum, and nickel-based alloys.

Together with the aforementioned machine improvements, improvements in fundamental understanding and optimization of the laser melting parameters responsible for the generation of the individual microscopic melt pools that, upon solidification, constitute the macroscopic part [21][22][23] led to an increase in achievable densities up to 99.98% [24], which is practically fully dense.

By 2017 the technology had developed to such a level that a combination of strength and ductility far surpassing that of conventional wrought stainless steel was achieved, as full density combined with the unique finely-textured microstructure generated by the extremely rapid solidification during the process was understood and leveraged [25][26].

However, the maximum achievable material performance is not the only technical criteria for a manufacturing process to be viable for part production. Equally important is the quality of the produced parts. *Quality is inversely proportional to variability* is a modern tenet in statistical quality control [27]. As AM technology, specifically PBF-LB processing of metallic materials, matured and was increasingly used for the production of end-use components, reports of high variability in the mechanical properties of parts produced started to emerge [28][29].

1.2 Objectives

The purpose of this study is to identify the root causes of the observed variability in properties of PBF-LB manufactured parts and quantify their impact. This is explored in the context of *machine architecture-defined* process parameters, which have rarely been adequately described in the Methods sections of studies which report material properties of PBF-LB AM. Such *machine architecture-defined* process parameters include how the laser beam is focused (defined by the optical configuration), how the powder is spread (defined by the re-coating mechanism), and how the process by-products are removed (defined by the shielding gas flow configuration). Specifically, the objective of this thesis is to establish the effects of shielding gas flow speed (Publication I), re-coater blade type (Publication III), and focal point position (Publication IV) on the quality of parts manufactured with PBF-LB AM. Furthermore, the variability in mechanical properties of parts produced using different machines and powders was studied, and the potential of standardized post-process heat treatments to reduce variability was explored (Publication II). The impact of the studied *machine architecture-defined* parameters on part quality is quantified, and practical guidance is provided on how these parameters should be considered in additive manufacturing procedure specifications (AMPS) or similar process control approaches aimed at assuring repeatable material properties. Additionally, this thesis presents strategies for in-situ process monitoring based on the usage of co-axial photodiode-based melt pool monitoring (MPM) and contact image sensor-based (CIS) powder bed monitoring for quality assurance purposes (Publications III and IV). The structure of the Publications covered in the thesis, and which part of the PBF-LB process they deal with, is shown in **Figure 1**.

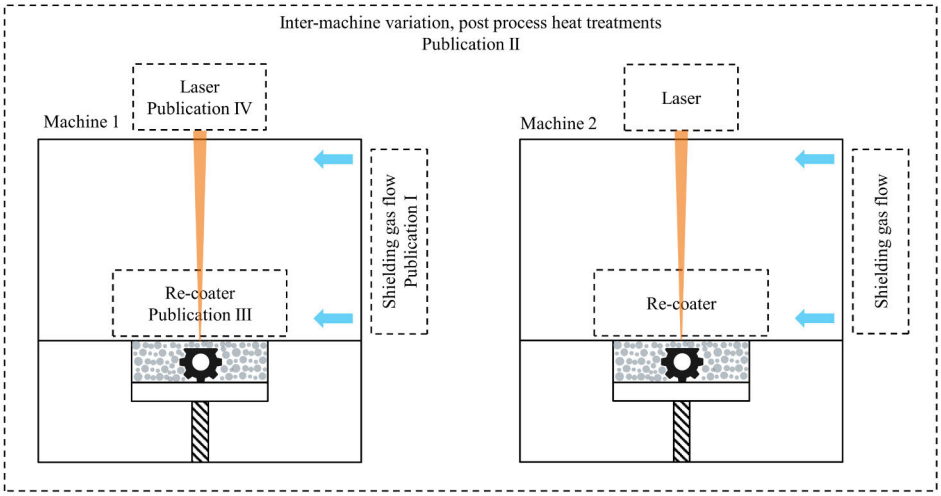

Figure 1. Structure and scope of the four individual publications covered in the thesis, in relation to the laser powder bed fusion process. Image: Joni Reijonen.

1.3 Scope and limitations

This thesis focuses specifically on one AM technology, laser powder bed fusion of metals (PBF-LB/M). All the experiments were conducted on 316L stainless steel, which is one of the most widely used alloys in PBF-LB/M. However, the literature reviewed also covers PBF-LB/M studies of other metal alloys, and although the impact of the studied processing conditions may differ in terms of the significance and severity of the measured responses in different alloys, it is argued that the general trends identified in this thesis apply to a wide range of alloys. This is because the re-coater, focused laser beam, and shielding gas flow are fundamental aspects of the PBF-LB/M process and regardless of the alloy, they always serve the same purpose in the build cycle; the re-coater spreads a layer of powder, the focused laser beam selectively melts it, and the shielding gas flow clears away process by-products.

In all the experiments, the main quality indicator measured was part density, represented as its inverse, i.e., remaining porosity. In this thesis, porosity (i.e. void fraction) includes all defects that manifest as voids in the material; the voids are not classified in detail into different defect types. However, in Publications I and IV, melt pool geometry as measured from polished and etched cross-sections was used to identify the dominant phenomenon responsible for the observed changes in porosity. Publication II extended the studied responses to tensile strength, elongation, and impact toughness, and the root cause analysis to microstructural and fracture surface characterization. The justification for using porosity as the main quality indicator to be measured is that it has been identified as the main contributor to the observed variability in PBF-LB AM of mechanical properties such as tensile

elongation and fatigue life [30]. Furthermore, it is known that deviations from the optimal melting conditions in PBF-LB AM lead to either lack of fusion, excessive keyholing, or Plateau-Rayleigh instability (commonly referred to as balling or humping), all of which manifest as increased porosity in the macroscopic 3-dimensional part [31][32].

1.4 Thesis structure

The thesis is divided into six main chapters. The first chapter is the introduction, which outlines the background, motivation, objectives, scope, limitations, and structure of the thesis. The second chapter introduces the laser powder bed fusion process that is studied in the thesis. A simplified model of the process is outlined, with inputs and outputs, and the *machine architecture-defined process parameters* that are the focus of this thesis are presented in detail. The interplay between the *process* and the *machine* is explored, and common approaches to defining the process energy density are laid out. A state-of-the-art literature review on variation in the mechanical properties of parts produced with PBF-LB AM is undertaken, including the possibility of utilizing certain process monitoring methods for quality assurance. In Chapter 3, the materials used and the methods and design of the experiments conducted to test the hypotheses set out at the beginning of the thesis are explained in detail. In Chapter 4, the experimental results are presented. Chapter 5 discusses the results in respect of the hypotheses and objectives of the thesis, the significance of the results, limitations of the studies, and recommendations for future studies. Chapter 6 provides a summary of the thesis and the main conclusions derived from the results.

2 Laser Powder Bed Fusion

2.1 Process overview

As defined by Hardt [33], any manufacturing process is just "*the interaction of a machine and a material to transform the material to the desired outputs geometry and properties*". And as with any physical transformation, this is achieved through the directed application of *energy* to the *material* via the manufacturing *machine*. Hardt further states that *geometry* (the shape of the part) and (intrinsic material) *properties* are the only outputs which completely define the performance of the part. The only inputs to this simplified, yet comprehensive, *model* of a manufacturing process are the material and machine parameters, as shown in **Figure 2**.

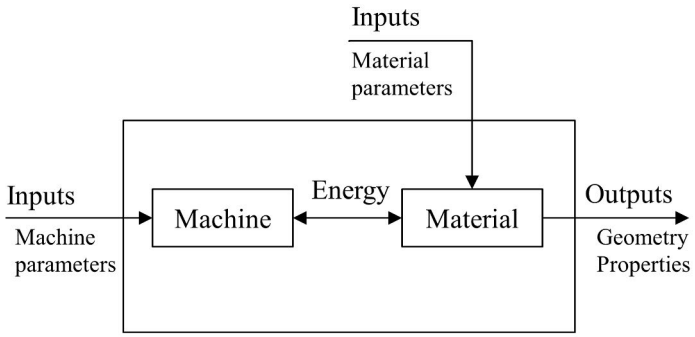

Figure 2. General model of a manufacturing process, adapted with permission from [34].

Control of the manufacturing process, and hence the quality of the outputs, necessitates control of the inputs. The only control the part *manufacturer* has over material inputs is the choice of the material itself and hence, strictly speaking, the only means of real *process control* at the manufacturing stage is via control of the machine inputs. **Figure 3** shows a slightly more detailed and illustrative model of the inputs and outputs specifically applied to the manufacturing process that is the focus of this thesis, namely the PBF-LB AM process. Of the input parameter groups, *the machine architecture-defined* process parameters, marked with dashed outlines, are the focus of this thesis.

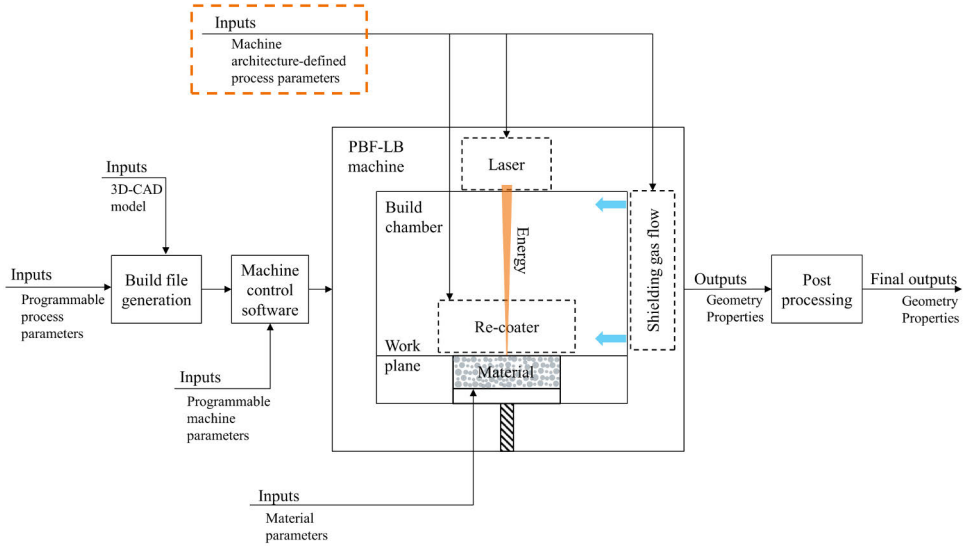

Figure 3. Model of the inputs and outputs of the PBF-LB process. The dashed outlines highlight the focus of this thesis. Image: Joni Reijonen.

2.2 Process parameters

Reduced for simplicity, the laser powder bed fusion process is essentially selective micro-laser welding (with a defined laser power) of metallic powder. A powder layer is spread on the build area, adjacent laser vectors (with a defined hatch distance) are then scanned (with a defined scanning speed) on the (x-y) build plane (with a defined scan pattern) to melt a layer corresponding to a sliced cross-section of the part geometry, followed by lowering of the building platform (with a defined layer thickness) and application of the adjacent powder layer in the (z) build direction. This process is repeated for *N* layers, until the 3-dimensional part is completed inside the formed powder bed. [35] The 3-dimensional part is built on top of a building platform, and the part can be rotated and oriented in any arbitrary orientation in relation to the 3-dimensional space. If the part has a feature which is inclined in relation to the build direction, that feature is called an overhang and may require additional support structures to ensure successful fabrication of the feature, as the powder bed itself does not provide sufficient mechanical support nor a heat-conduction path [36]. In the experimental section of this thesis, the orientation of a part in relation to the build direction is always specified. Also, the orientation in relation to the gas flow direction or re-coating direction is given. The process, along with the fundamental process parameters, is schematically illustrated in **Figure 4**.

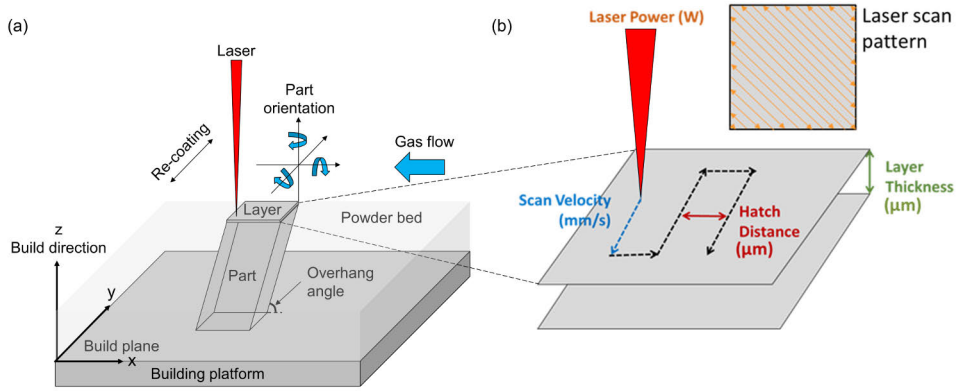

Figure 4. Schematic illustration of (a) the building of a part using the PBF-LB process and (b) the most fundamental, adjustable processing parameters. Image (a): Joni Reijonen. Image (b) is reprinted from [37] under the CC BY 4.0 license.

Process parameters are the set input conditions that can be used to adjust the process. Although the terms process *parameter* and process *variable* are quite often used interchangeably in manufacturing science and engineering, in this thesis, a distinction is made between process *parameters* and *variables*. Input conditions that can be used to adjust the process are called process parameters. These are usually static in nature, or at least have a set-point, and are set to a singular value in an experiment but can be varied between experiments. Examples are all the fundamental process parameters shown in **Figure 4**: laser power, scanning speed, hatch distance, layer thickness, and scanning strategy. A process variable is some actual, physical condition and its *current value state* in the process. In other words, a model state, which may vary within an experiment. Examples of such process variables in the PBF-LB process are the powder bed packing density and melt pool size or temperature.

Usually, to *develop* a set of processing parameters for a given alloy the two most influential parameters, laser power and scanning speed, are first optimized to establish the processing window which results in full density, or at least minimal porosity in the part due to unwanted process defects such as excessive keyholing, lack of fusion, balling, or humping. Keyhole pores form when the laser energy density is too high and a fluctuating keyhole is present, which upon collapse may leave pores in the solidified material [38]. Lack of fusion occurs when insufficient laser energy results in not all the powder being melted, with unmelted regions left between either adjacent tracks or layers [39]. Humping is the breaking of a smooth and continuous molten track into an instable undulation of valleys and peaks, i.e. humps, due to Rayleigh-Plateau instability at high scanning speeds associated with excessive laser power, as a long and overly narrow stream of liquid (i.e. the molten

track) tends to minimize the surface area [40]. Balling is a rather similar phenomenon, which occurs with excessive scanning speed and relatively low laser power, resulting in molten tracks that have poor penetration to the substrate and the melt breaking into separate balls instead of forming a continuous melt pool, as the melt tends to minimize the surface area and form a stream of discontinuous balls [41]. All these processing defects lead to the formation of *voids* in an otherwise *dense* macroscopic 3-dimensional part when it is built from adjacent solidified tracks and layers. In this thesis, regardless of their cause, the combination of all such voids in an otherwise dense material is referred to as *porosity*. In other words, porosity is the measure of the void fraction in the solidified material. A schematic processing map showing the respective areas where each of these process defects occur on the laser power / scanning speed axis is illustrated in **Figure 5**.

An initial assessment of the optimal combination of laser power and scanning speed could even be explored with single-track studies, where single laser vectors are melted on a layer of powder [41]. In such scenarios, laser power and scanning speed are the only inputs. Expanding from this, the hatch distance and scanning strategy can be included in the design of experiments to optimize the process [42]. Usually, the combination of these parameters is optimized for a single layer thickness, and *process parameter sets*, intended for building parts from a certain alloy with a certain layer thickness, are provided to the machine. The reasoning behind this approach may be practical in nature: generally, in PBF-LB machines layer thickness is a *global* parameter, in the sense that it cannot be varied between specimens, while laser power, speed, hatch, and scanning pattern are *local* parameters and can be freely programmatically varied between different locations in the build volume.

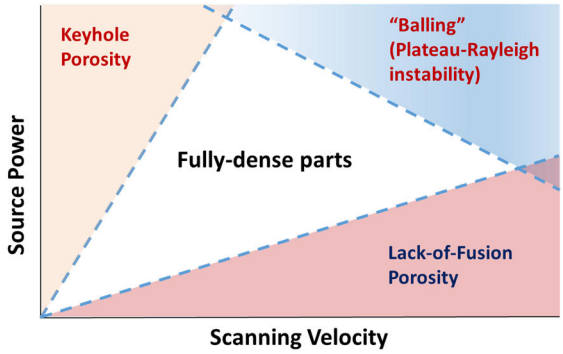

Figure 5. Schematic illustration of the influence of the two most influential adjustable processing parameters in a PBF-LB machine, laser power and scanning speed, on defect formation. Reprinted from [37] under the CC BY 4.0 license.

2.2.1 Essential parameters

Input process parameters which have an impact on the output properties of the parts produced are called essential parameters. From a quality control perspective, it is therefore necessary that such parameters are monitored and controlled during manufacture to assure the quality of the outputs [43]. The first step in establishing a stable and repeatable manufacturing process is to identify all the essential parameters, and analyze their impact on the process and on the output properties. Research on the effects of the main process parameters (laser power, scanning speed, hatch distance, layer thickness, and scanning strategy) on the resulting properties of various alloys is plentiful and their impacts on the process are generally well understood [37][44][45][46][47][48][49][50]. However, these studies on the impact of the most fundamental process parameters have mainly been carried out with the goal of improving or optimizing the process to maximize the values of outputs such as density or mechanical properties. When the focus is on understanding the impact of a certain process parameter, numerous simplifications are made and the number of parameters is reduced to a minimum. Furthermore, most studies intending to establish the impact of a certain process parameter on a certain output property have been performed on a single machine, and whether the results would be the same on a different machine is largely unknown. The hypothesis here is that certain *machine architecture-defined* process parameters have a significant impact on the properties of parts produced.

As already stated in the introduction of this thesis, equally important is to study the *stability* and *repeatability* of the output in realistic production conditions. Studies that do not oversimplify the PBF-LB process and reduce the input parameters to only the four or five most fundamental ones are scarce. Another systematic omittance in the vast majority of studies which have reported mechanical (or other relevant) output properties for PBF-LB processed alloys is a list of the state of *all the essential input parameters* that were used in the manufacture of the test specimens. It has been common practice in previous studies to report only the four or five main parameters, namely the laser power, scanning speed, layer thickness, and hatch distance, along with some (inadequate) description of the scanning strategy applied and a mention of the machine model used. Depending on the source, and more importantly how one counts the individual process parameters in the PBF-LB process, there can be more than 100 [37] of them. However, such counts are always arbitrary, as some parameters cannot be reduced to a single metric value to describe them, such as the scanning strategy or the shielding gas flow in the machine. Nevertheless, the fact remains that significantly more than the four or five main input process parameters shown in **Figure 4** that determine the quality of the output, as shown in **Figure 3**.

2.2.2 Non-essential parameters

In statistical process control adapted from welding and applied to PBF-LB manufacturing, process parameters that have no statistically significant effect on mechanical properties (or on any other relevant output property) which affect the functioning of the part are called non-essential [51]. This means that no control of the state of these parameters is necessary. However, it therefore follows that this category may include certain process parameters that do indeed have an impact on the output properties, but this impact is not yet known or scientifically proven. If proven, such parameters should be transferred to the category of essential parameters. In this thesis, the main hypothesis is that certain *machine architecture-defined* parameters that have been scarcely studied and systematically neglected in the listing of process parameters in the Methods sections of studies reporting PBF-LB material properties are indeed essential parameters.

For experts in the field, it is very hard to come up with examples of non-essential parameters in the case of PBF-LB process other than clearly irrelevant ones, such as whether the light on the build chamber is on or off, or on which day of the week the build job was conducted. The reason for this is that unlike in subtractive or formative manufacturing processes such as CNC machining or sheet-metal forming where the microstructure of the feedstock material sets inherent boundaries for the material properties that are either *retained* or *modified* over these manufacturing processes and hence dictate the final material properties of the manufactured part, in additive manufacturing the material properties are *formed* during the manufacturing process [52]. The microstructure of the feedstock powder is destroyed during melting, and a new microstructure is generated upon solidification during the PBF-LB process. Therefore, any change in the parameters of the manufacturing process is likely to have a significant impact on the resulting structure and properties. This is very similar to welding process control, where the same fundament applies [53]. It is therefore important to carefully study the nature and magnitude of the impact that each process parameter has on the quality of parts produced in order to establish tolerance limits defining how much, if at all, the parameters can vary before quality is compromised.

2.2.3 Additive manufacturing procedure specification

Because of the inherent similarity of welding and PBF-LB AM, the approaches to PBF-LB process control have been mainly adapted from welding. In welding, the essential part of quality control is the Welding Procedure Specification (WPS) [53], in which the essential parameters, along with their values and allowed variation range to produce a weld that meets the set requirements, are defined. In PBF-LB, and in additive manufacturing generally, a similar concept was adopted by the

standardization organizations [54]; although not yet the standardized term, it is often called the Additive Manufacturing Procedure Specification (AMPS). In terms of identifying key process parameters, their impact on the process, and the potential to control the PBF-LB process, the International Aerospace Material Specification AMS7003 [43] is the best standard reference as of today.

There are a few key differences between welding and PBF-LB AM which make process control and quality assurance in PBF-LB AM even more challenging. A welded product involves a *base material* and a *weld material*, both with intrinsic material properties. The weld is a discontinuity in the material and may very well be the weakest link in the structure. Much can be done to design the structure and location of the welds such that the maximum stresses on the part are not at the weld location. However, in PBF-LB AM, there is no base material, only kilometers of weld material which make up the whole product. It is therefore unavoidable that the maximum stresses on the part will be on the weld material, or more specifically the PBF-LB material.

The second key difference is that the main motivation to use PBF-LB in the manufacture of structural parts is the design freedom it provides. This allows for the design and manufacture of highly efficient structures, that is, optimized structures with low mass but high load-bearing capacity from which all unnecessary material that plays no part in conveying loads has been removed. In such *topologically optimized* structures, to maintain the efficiency of the design, the factor of safety cannot be exaggerated [55]. This necessitates low variability in the mechanical properties of the manufactured material.

2.3 Variability in mechanical properties

The observed variability in the mechanical properties of parts produced using PBF-LB is a key challenge for wider adoption and to realize the full potential of the technology.

Early studies by Prater et al. [28] and Brown et al. [29] found statistically significant differences in tensile properties (yield strength, ultimate tensile strength and elongation at fracture) between specimen groups produced using different PBF-LB machines. In their studies, the inter-machine variation was higher than within-batch variation in a set of specimens produced in a single machine; however, the within-batch variation of elongation was also noted to be high, and of a similar level to the inter-machine variation in Brown et al. [29]. The study by Prater et al. included no additional microscopy or SEM analysis of cross-sections and microstructure, and while Brown et al. used SEM to analyze the fracture surfaces of the specimens, neither study was able to draw conclusions on the root causes of the observed variations. The studies aimed to find out whether variation exists and if so, to

measure the magnitude, but they were not designed to enable the researchers to conclude what elements of the input machine settings or the resulting (micro)-structure of the PBF-LB manufactured material caused the variation in mechanical properties. Both urged that further studies be carried out to build on their important findings. Further studies were conducted over the following years, and in one synthesis of the data collected on multiple alloys processed with PBF-LB by Dowling et al. [56] the coefficient of variation was estimated to be 1–6 % for UTS and 9–19% for elongation, compared to around 1–3% in both properties for conventionally produced materials.

Simultaneously, another line of research intended to establish the correlations between process parameter values, the forming melt pool, the solidified microstructure, porosity formation, and the resulting mechanical properties [44][45][46][47][48][57][50], concluded that defects generated during the melting process on various scales in the micro- and macro-structure dictate the properties of the PBF-LB processed material, and that they follow the general process-structure-properties-performance causality of any kind of materials processing. However, it was specifically found that elongation at fracture is highly sensitive to the porosity generated in the PBF-LB process, even when present in small (<0.5%) quantities [58].

Further studies on the variability in properties, such as that by Moran et al. [59] which used computed x-ray tomography to analyze defects, established that there is substantial variation in the number of defects in specimens produced even by a single machine using identical process parameter values, but at different locations in the building platform. They analyzed the spatial dependency of build defects on two different machines and found not only significant within-machine variation, but also that the spatial distribution of defects varied between machine types. Moran et al. already used weakest link fatigue life predictions to show the potential implications of such variations in defects on the dynamic mechanical properties. Berez et al. [60] conducted a comprehensive study utilizing both xCT analysis to quantify defect population and sizes and fatigue testing to conclude that 1) there is high variation in build defects (i.e. size, shape, and amount of porosity) across the build area, leading to 2) extreme variation in the fatigue life (from ~20 000 cycles to run-out, defined as 3.9 million cycles) of PBF-LB produced parts. The coefficient of variation in the fatigue life data set of their study was 194%. The findings from the study by Berez et al. are summarized in **Figure 6**.

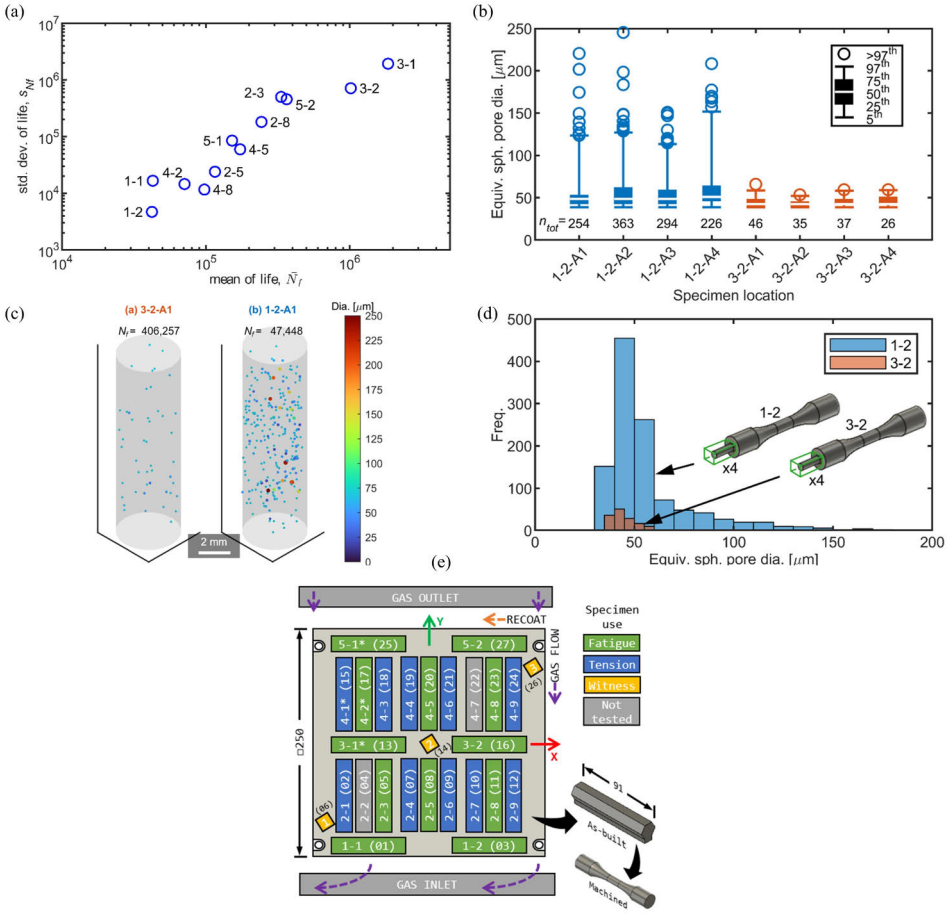

Figure 6. Variation in (a) fatigue life and the corresponding variation in (b) defect size distribution of specimens produced at (e) different locations of the PBF-LB build area but with identical parameter values; (c, d) further details on the pore distributions at the extremes of fatigue life. Reprinted with permission from [60].

Fatigue life is known to be notoriously sensitive to pore distribution, shape, size, and location within the specimen [61]. The study by Berez et al. found that lack-of-fusion defects with sharp edges close to the specimen surface were most detrimental to fatigue life. Compounding the problem, a study by Sanaei et al. [62] found significant variation in defect distributions not only between machines and between locations in the build volume, but also within the specimen geometry. They found higher concentrations of defects near the surface and in thin-walled sections of the specimens.

A pessimistic approach, and one that has been utilized by PBF-LB practitioners to combat this variability, is to freeze everything in the process. From the process parameters to the serial number of the machine, from the location of the part in the

building platform to even the part geometry and orientation. Change any of this, and extensive, costly re-qualification tests are necessary. This, of course, goes against some of the ambitions of AM technology, which are to be flexible both in terms of part designs and manufacturing locations [63].

It seems that everything goes back to the fundamental challenge of the PBF-LB process that has remained since its invention in the 1990s [7]: the reduction and control of pore formation. The question, then, is what causes this high variation in the porosity and hence in the mechanical properties of parts produced with PBF-LB AM? If the input conditions (i.e. the machine, process, and material parameters) remain constant, the output properties should remain constant (within random variation), as previously discussed. Therefore, either there are 1) additional (but at this point unknown) sources of input parameters that do not remain constant between the tested specimens and that have a significant impact on porosity, or 2) the random, stochastic variation in porosity and mechanical properties caused by stochastic phenomena in the PBF-LB process are indeed inherently very high. Scenario 2 would mean that the PBF-LB process, as executed by currently available machines, is unsuitable for distributed manufacturing of critical components with sufficient quality. Hence Scenario 1 needs to be thoroughly investigated, and is the focus of this dissertation.

2.4 Machine architecture-defined process parameters

The main hypothesis of this thesis, synthesized from the analysis presented above, is that certain *machine architecture-defined* input parameters, that have not been identified, nor controlled, or that have been insufficiently described or quantified in the most previous studies, have significant impact on the defect formation in the process and contribute to the observed variability in the output properties. Without the identification and control of all essential process input parameters, a stable and repeatable output of properties cannot be expected.

Therefore, a further distinction in relation to process parameters made in this thesis is that between *process* and *machine* parameters. Process parameters are those that are inherent to the process of PBF-LB, regardless of the individual machine used. It therefore follows that process parameters can be *programmatically* set to be equal between machines. Examples of such parameters are laser power, scanning speed, layer thickness, and scanning strategy. Within the context of this thesis, a PBF-LB machine requires these parameters to run the process, otherwise that machine does not operate based on the PBF-LB process. The scanning strategies of modern PBF-LB machines consists of a very complex combination of parameters

that define the scanning pattern; nevertheless, with sufficient knowledge, they can still be *programmatically* set equally on different machines.

In addition to these programmatically controlled process parameters, certain *machine architecture-defined* process parameters are defined by the architecture of the machine *hardware*, which cannot be adjusted or fully controlled *programmatically*. It therefore follows that such process parameters cannot be set equally on different machines (without changes to the machine hardware), unless the machines are identical (brand, model, and version). Such *machine architecture-defined* process parameters include how the laser beam is focused (defined by the optical configuration), how the powder is spread (defined by the re-coating mechanism), and how the process by-products are removed (defined by the shielding gas flow configuration). These *machine architecture-defined* process parameters, and their influence on part quality, are the focus of this thesis.

2.4.1 Laser beam focal point position

The primary tool of a PBF-LB machine, which drives the physical transformation from *material* to *part*, is the focused laser beam that is used to selectively melt the powder in consecutive tracks and layers which, upon solidification, form the 3-dimensional solid part. The key components of this tool are:

- The laser; i.e. wavelength, beam quality, beam mode, intensity profile, output power, whether it is operated in continuous wave or pulsed mode, and any other property that comes from the laser source.
- The optics; i.e. the transport fiber, collimator, focusing optics, mirrors, windows, scanner, and any other optical component between the laser and the work plane.

Machine hardware defines how the beam propagates and most importantly, the conditions at the *focal point* and at the material interaction plane where the melting takes place (which may or may not be the same point, depending on the focal point position). Quite often in PBF-LB, the processing is done at the focal point, as this is where the beam diameter is at a minimum, the laser power density (W/mm^2) is highest and hence, the least amount of laser power is needed to melt the powder. To control the PBF-LB process is to control how the melting takes place, and this is highly dependent on the characteristics of the laser at the beam-material interaction plane. To simplify, for an ideal Gaussian beam, the key parameters at the interaction plane can be reduced to 1) the laser power, 2) the beam diameter, and 3) the focal point position in relation to the beam-material interaction plane. This is illustrated in **Figure 7**.

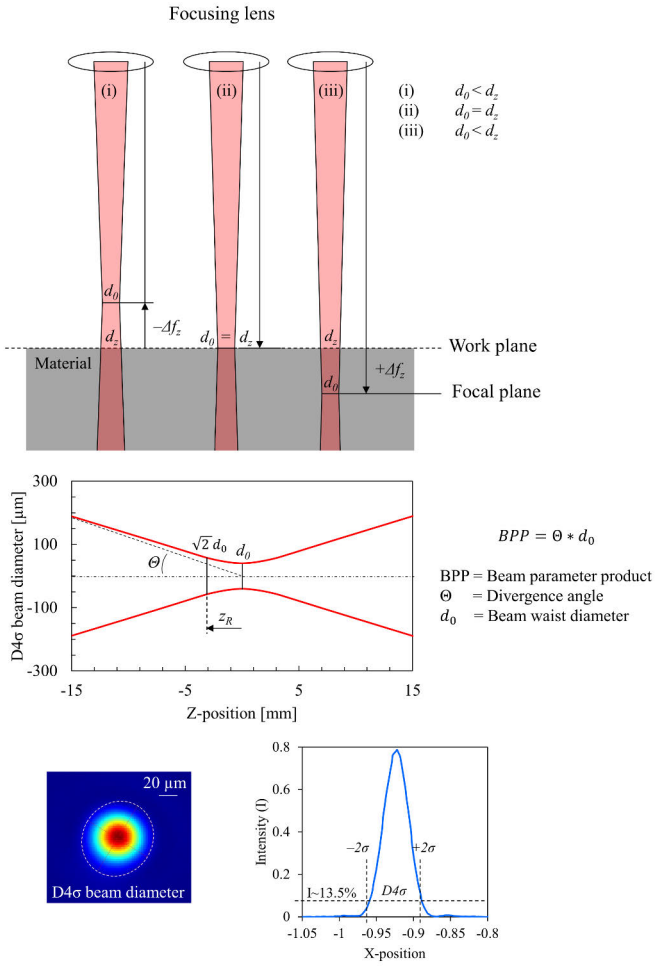

Figure 7. Schematic representation of (a) the focal point position in relation to the work plane and (b-c) determination of the *D4σ* beam diameter d_0, Rayleigh length z_R, and beam parameter product *BPP* from the propagation of a Gaussian beam. Image: Joni Reijonen.

From a process control perspective, laser power is easy to manage as it can be set and controlled programmatically. Also, the focal point position can be adjusted (either manually or, in most modern PBF-LB machines, programmatically) to be the same. Beam diameter, however, is defined by the laser beam and all the optics in between, hence it is a *machine architecture-defined* parameter and unless there are no adjustable beam-shaping components in the system it is fixed to a single setting.

This is the case in an ideal world. However, as optical components are never perfect, all three of these parameters are interconnected. In a real laser processing system, the laser power used will have an influence on both the beam diameter and

the stability of the focal point position due to thermal lensing caused by temperature differences in the optics as the laser interacts with them. Also, any form of dirt, inhomogeneity, or physical degradation (such as a scratch or crack) on an optical component will contribute to thermal lensing and change the beam propagation. Most notably, this manifests as drift in the focal point position of the laser beam. To control the focal drift is to control the quality and cleanliness of the optical components, i.e. aspects of the *machine hardware*. These conditions may be different between individual machines, even if nominally they are of identical make.

The impacts of changes in the laser power and laser beam diameter on the melt pool formation and resulting porosity are well understood [64]. Performing PBF-LB processing with two significantly different beams (in terms of mode, wavelength, diameter, or intensity distribution) is such a fundamental change to the process that it is already questionable whether it can even be called the same process anymore. For example, melting with a wide beam with a top-hat intensity distribution as in [64] will result in a shallow and wide melt pool, with melt pool temperatures below the vaporization threshold at all locations on the beam cross-section, and hence no vaporization will occur. On the contrary, melting with a narrow beam with a Gaussian intensity distribution will lead to vaporization at the center of the melt pool, resulting in deep and narrow melt pools due to keyhole formation [64], along with the associated process by-products and defect formation mechanisms, which will be explained later. To make an analogy to a CNC machine, depending on the tool selected, one can engage in milling or drilling with the same machine, however these are two different processes. In PBF-LB processes, the laser beam is the tool. Beam shaping in PBF-LB has recently become an active research topic [65][66][67][68]. If advanced beam shaping is implemented in future generations of commercial PBF-LB machines, almost any arbitrary beam shape and intensity distribution could be utilized. Characterization and adequate description of the beam used will therefore be of utmost importance to allow for replication.

Some studies on the impact of the focal point position on the melt pool formation and resulting part quality have been conducted previously [69][70][71][72]. However, no studies have aimed to establish an acceptable tolerance limit for variation in the focal point position before part quality is significantly impaired. Furthermore, the setting of the focal point position parameter and confirmation of its stability are rarely reported in PBF-LB studies. This was the topic of Publication IV.

2.4.2 Re-coater blade type

Re-coating is the step in the PBF-LB process where the metal powder is applied to the build area in layers. The thickness of the deposited powder layer is called the layer thickness. In PBF-LB the applied layer thicknesses are typically in the range

of 20–100 µm. The essential processing parameters that define how the powder is spread are the layer thickness, the re-coating speed, the amount of powder applied, and the type of re-coater blade used [73]. The re-coating may be uni- or bi-directional depending on the machine. In bi-directional re-coaters, the blade tip profile is usually symmetric in both directions. This is illustrated in **Figure 8**.

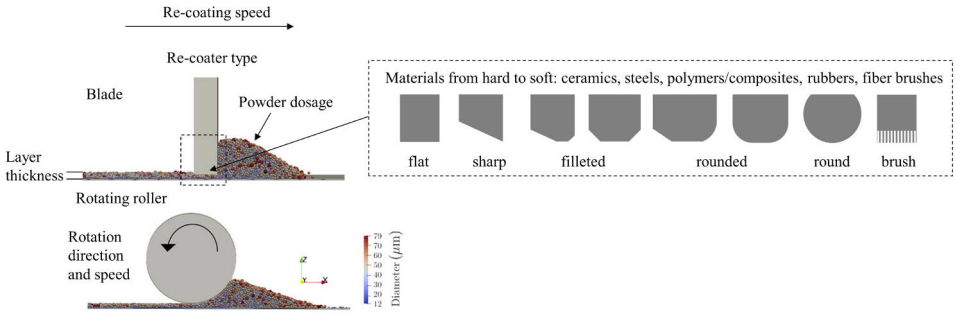

Figure 8. Schematic representation of the re-coating process, related parameters, and examples of typical re-coater blade types used in commercial PBF-LB machines. Modified from [74] under the CC BY 4.0 license.

Layer thickness and linear re-coating speed can be programmatically controlled and are therefore not *machine architecture-defined* parameters in the context of this thesis, as they can be set equally on different machines. The volume of powder applied is also directly or indirectly programmatically controlled in PBF-LB machines, regardless of whether the powder is supplied from a bin under or from a hopper above the processing plane, which are the common approaches. The controllable parameters may not be the same between the approaches, but their only purpose is to set the volume high enough to completely fill the layer. From a control perspective, it is easy enough to set the overdosage factors high enough that in all conditions a sufficient volume of powder is supplied. The excess powder goes to the overflow bins. Therefore, a threshold can be found above which sufficient powder is supplied. Identifying this threshold, and setting the values above it, is an effective means to set the volume of powder applied per layer equally on different machines. It was shown by Jansen et al. [75] that as long as sufficient powder is provided, increasing the powder dose factor further has no effect on the effective powder layer thickness. Therefore, this parameter is not considered a *machine architecture-defined* parameter in the context of this thesis.

The final parameter to consider is the type of re-coater blade itself. Any type of blade (material and geometry) can be used. Typically, in commercial PBF-LB machines, the blades used can be categorized as either hard, soft, brush, or rotating roller [73][76]. The re-coater blade type may be fixed by design or it may be

changeable, depending on the machine model. The blade tip geometries used vary from sharp to filleted and from flat to round. Given the variety of re-coating blade types, it is crucial to study whether the re-coater blade type has a significant effect on the quality of the spread of the powder layer and, correspondingly, on the quality of parts produced. The need for further research on the impact of the powder re-coating strategy on the final part properties was highlighted in a comprehensive review by Capozzi et al. [73].

Only a few experimental studies have been conducted on the impact of the re-coater blade on the resulting part properties. Dańa et al. [77] reported that using a ceramic (hard) blade was less suited for building thin features such as support structures, as the unyielding hard blade is liable to deform the part, and also to disturb the powder bed when in contact with the part surface during re-coating. Shamsdini et al. [78] found that parts built using a carbon fiber brush had significantly reduced elongation at fracture compared to parts built using a ceramic blade. Fox et al. [76] compared the tensile strength of parts produced using carbon fiber brush, steel, and rubber blades, and found no statistically significant (N=36) differences in tensile strength. Unfortunately, this study did not report on elongation at fracture, although it was noted that the usage of a rubber or carbon fiber brush resulted in increased porosity compared to usage of a steel blade. As experimental studies on the topic were scarce, this was studied in Publication III.

Furthermore, despite being a very fundamental element of the process, the type of re-coating blade used and the related re-coating parameters are rarely reported in PBF-LB studies. Illustratively, even in the reviewed literature which had re-coater blade type as an intended variable [77][78][76], the re-coating speeds used were not reported in the Methods sections.

2.4.3 Shielding gas flow configuration

In the PBF-LB process, a protective inert gas atmosphere (typically argon or nitrogen) is utilized in the build chamber to prevent oxidation of the melt pool, and to enable the processing of highly reactive materials in fine powder form. Instead of filling the chamber with inert gas, in modern PBF-LB machines the gas is circulated in one way or another to generate a cross-flow of shielding gas. The purpose of this flow is to carry away the process by-products generated in the melting process. This is schematically shown in **Figure 9**. The process by-products include 1) the metal vapor plume generated by vaporization in the melt pool, 2) the condensate from this when the vapor cools down and solidifies, 3) denudated powder particles ejected from the vicinity of the melt pool by the vapor-induced entrained gas flow, which are called cold spatters if not melted by the laser or 4) hot spatters if melted, and 5) droplets ejected from the melt pool that are also referred to as hot spatters.

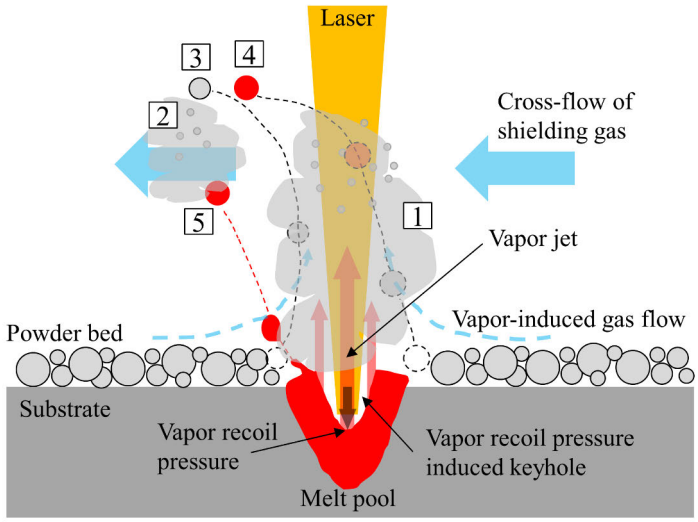

Figure 9. Schematic representation of the process by-products generated in the PBF-LB process and their removal by the circulating shielding gas flow: 1) vapor plume, 2) metal condensate, 3) denudated (cold) powder particles, 4) denudated (hot) powder particles melted by the laser, and 5) (hot) spatter ejected from the melt pool. Image: Joni Reijonen.

If the shielding gas flow lacks sufficient momentum to remove the process by-products from the build area, they can cause various unwanted changes in the processing conditions that lead to defect formation. Negative effects of insufficient shielding gas flow on porosity and mechanical properties have been identified in earlier studies [15][79][80][81]; however, these studies did not come to definitive conclusions on the root causes that link shielding gas flow speed to porosity formation, hence this was studied in Publication I. The following impacts of insufficient shielding gas flow have been identified:

- The presence of metal vapor, metal condensate, or hot or cold spatters will attenuate and scatter the propagating laser beam. Whether attenuation or scattering dominates depends on the composition and size distribution of the particulate material on the beam path. [80][82]
- Hot spatters and the condensate from the metal vapor have very high temperatures, and hence have extremely high affinity to the pick-up of residual oxygen or other impurities from the build chamber atmosphere [83]. When these by-products land on unfused locations on the build area, a concentration of impurities may be transmitted to the part at that specific location when the laser fuses it.

- All process by-products, but most notably large spatters, will change the powder bed conditions at the location where they land. When this happens in an as yet unfused area of the layer, when the laser then comes to melt the area in question the powder bed conditions are different from the spread, undisturbed nominal powder layer. Large spatters especially have been shown to cause defects, as they change the conditions at the location where they land [84].
- If the process by-products reach the laser beam entry glass at the ceiling of the build chamber, they can stick to it and contaminate the window. Any dirt on optical components will change the behavior of the focused laser beam propagation.

From a control perspective, the shielding gas flow is a challenging parameter. The flow conditions in the build chamber are defined by a) what gas is used, b) the flow rate, and c) how it is distributed. Fixing the gas type is easy, for example by selecting to use argon with a certain purity grade. Fixing the mass flow rate of the gas means very little without consideration of *how the gas flow is distributed*, which is much more challenging to define and control as it depends on the geometry of the flow path. In a simplified scenario such as a straight pipe of uniform flow with a well-defined and planar cross-section, the volumetric flow rate is defined as $Q=v*A$, where v is the flow speed and A the cross-sectional area of the flow path. However, in a real PBF-LB system the geometry of the shielding gas flow path, especially the inlets and outlets of the gas to the build chamber, can be of practically any shape and dimensions that the machine designers can come up with. To generate identical shielding gas flow conditions between two machines would require that the shapes and dimensions of all the components that are part of the gas flow cycle be identical. The shielding gas flow is therefore a primary example of a *machine architecture-defined* process parameter in the context of this thesis. **Figure 10** shows examples of the variety of shielding gas flow designs in some of the commercial PBF-LB machines available. Furthermore, even within the same machine type, the machine manufacturers may have made upgrades to the shielding gas flow design over the years, as shown in the white paper published by GE Additive [85] for their Concept Laser M2 model. There the gas flow configuration was re-designed to provide more laminar flow across the build volume and remove the circulation zone above the build plate in the earlier design.

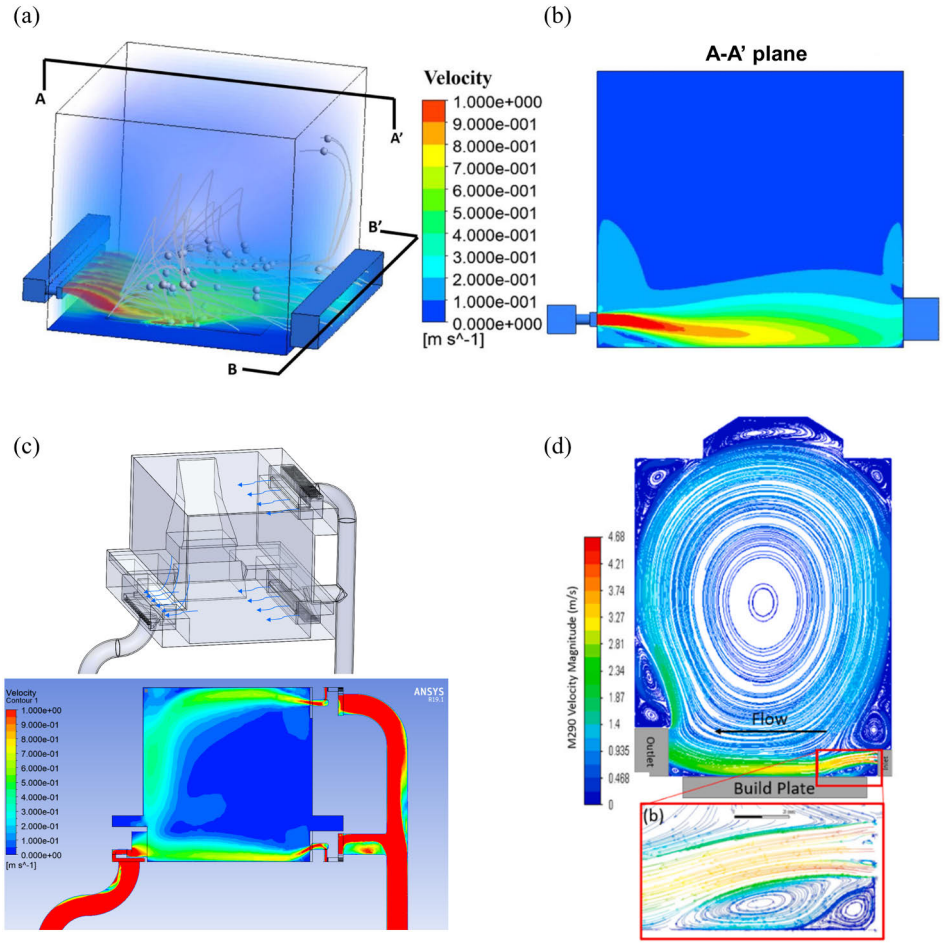

Figure 10. Shielding gas flow designs of (a, b) the Renishaw AM 250, reprinted with permission from [86], (c) the SLM Solutions SLM 125 HL model from 2014 (image: Joni Reijonen), and (d) the EOS M 290, reprinted with permission from [59].

A comprehensive, quantitative description of the shielding gas flow parameter requires a complete computational fluid dynamics model of it. However, for practitioners, something more compact and practical is needed. What is important regarding flow is first that there is sufficient flow rate, i.e., momentum, above the build area to remove the process by-products. Secondly, the flow should be laminar to avoid turbulence and re-circulation of process by-products in the build chamber. The flow should be such that when the by-products are removed in one location, they are not re-entrained to the beam path in another location. [86] Within a machine (once the geometry of the flow path is fixed), the flow is essentially controlled by the circulation pump power, which defines the mass flow rate of the gas. The control

parameter, for the operator of the PBF-LB machine, varies based on the machine brand and model. In some cases, the set value is a pressure difference over two specific measuring points in the flow cycle. In others, it is the pump power and in others the flow speed, as measured at a specific location on the flow cycle. Whatever the set reference point for the control, what is ultimately adjusted is the pumping power. As pressure loss over the system may not remain constant (most notably due to filter clogging over the build cycle), the best approach in terms of control would be to measure the flow speed in the build area and ensure it remains constant. As nothing physical can be in the build area during the build cycle, the next best thing would be to measure the flow speed at a couple of specified locations in the piping and ensure that they remain constant (within set limits), regardless of the filter condition.

Regardless of the approach towards controlling the shielding gas flow speed, providing some parameter or description characterizing it should be required in studies related to PBF-LB; however, in most studies, none is provided. Furthermore, the impact of the shielding gas flow speed on the melting process and resulting part properties is not well understood, hence it was selected as a topic for Publication I.

2.5 Interplay between process and machine

Although earlier a distinction was made between *process* and *machine* parameters, they are not separate, but interconnected. Even if the *controllable process parameters* are kept constant and set equally on two different machines, the *machine architecture-defined* process parameters may have an impact on what the set value actually is during processing. The reverse is also true, in that the selection of a *process* parameter value can have an impact on the *machine* parameter. This is perhaps best clarified with a couple of examples.

The first example concerns the interconnectedness between laser power, the most influential parameter in the process, and the shielding gas flow. The laser power parameter which is set and programmatically controlled is the output power from the laser source. However, this does not equal the power that is conveyed to the melt pool. Even if assuming equal optical losses in the machine components and equal absorptivity at the powder bed, laser power may be attenuated or scattered by anything that is in the optical path of the laser beam and the work plane. In the case of PBF-LB processing, this would be the process by-products; spatters, denudated powder, the vapor, and the condensate from it. How much these by-products prevent the laser power from reaching the work plane is highly dependent on the effectiveness of the shielding gas flow in removing them from the beam path, and the shielding gas flow conditions that are present at the build chamber are *machine architecture-defined*. To ensure that the laser power that reaches the work plane and

contributes to the melting process remains constant would therefore require, among other conditions, that the shielding gas flow conditions also remain constant. This interplay also works the other way around, as was shown by Bidare et al. [87] utilizing schlieren imaging. Higher laser power will generate a more intense vapor plume, and hence more momentum is required from the shielding gas flow to be able to clear away the plume to the same extent as with lower laser power. This is shown in **Figure 11**, where (a) shows a vapor plume without, and (b) with a cross-flow of shielding gas flow. **Figure 11** (c) show how the vapor plume is larger and extends higher before the cross-flow is sufficient to clear it away when laser power is increased from 100 W to 200 W while applying a constant cross-flow of shielding gas.

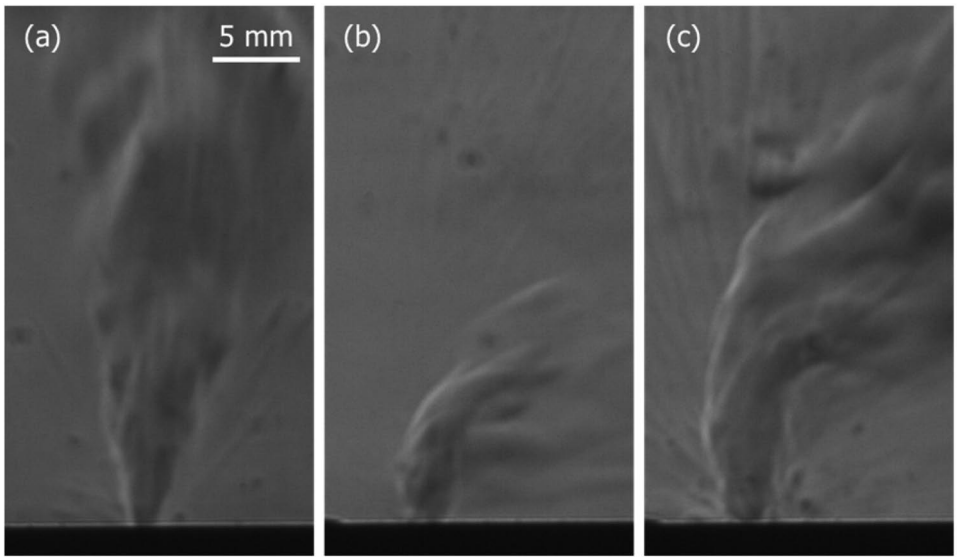

Figure 11. Long exposure time schlieren imaging of the vapor plume generated in a PBF-LB process: (a) 100 W laser power without cross-flow of shielding gas, (b) 100 W laser power with 10 l/min cross-flow of shielding gas and (c) 200 W laser power with 10 l/min cross-flow of shielding gas. In (b, c) the cross-flow of shielding gas is from left to right in the images. Reprinted from [87] under the CC BY 4.0 license.

The second example also concerns the interconnection between laser power, a *process parameter*, and beam quality, beam diameter, and focal point position, which by definition are *machine architecture-defined parameters* and should be fixed for a given combination of laser source and optics. However, as explained previously, focal shift due to thermal lensing changes the properties of the focused laser beam, and the severity of thermal lensing is, quite naturally, dependent not only on the quality of the optics but also on the laser power [88]. For the SLM 125 HL system

used in this thesis, this variation was demonstrated by analyzing the beam with three different power levels (60W, 100 W, and 400 W) to determine the beam quality (*BPP* = 0.46−0.50 mm*mrad), Rayleigh length (z_R = 2.84−3.11 mm), focal point diameter (d_0 = 72.6−78.5 µm), and focal point position in relation to the nominal work plane (z_0 = −0.75−0.06 mm). Therefore, strictly speaking, all the other properties of the beam only remain constant if the laser power remains constant. When the laser power is changed, the beam quality, Rayleigh length, focal point diameter, and position change along with it.

The third example also ties the laser power, via the shielding gas flow, to the *machine architecture-defined* re-coating, which, as explained previously, defines the conditions of the spread powder layer. A change in laser power changes the number and velocity of the cold and hot spatters formed in the process [89][90]. The more spatters, the higher the number of spatters that will not be removed by the shielding gas flow and instead redistributed on the unfused areas of the powder bed [86]. These spatter particles alter the conditions of the powder layer at the locations where they land. Laser power hence has an indirect influence on the powder layer properties, which by definition should be controlled by the re-coating step in the build cycle.

Because of such interplay between the process and the machine in real-world applications, simplified *ideal* process models will inherently suffer from an inability to predict process outputs with high accuracy. This is because *ideal* models do not consider the *real* imperfections of the machine that executes the process as inputs. Such simplified models are therefore incapable of capturing variations in the process inputs and hence also in the resulting outputs. They are therefore inherently useless for quality assurance and control. Nevertheless, this does not preclude researchers from developing simplified process models in an attempt to *understand* the fundamentals of the process.

2.6 Simplified energy density models

This chapter briefly introduces the most common, simplified *spreadsheet* level process models of the energy input to the PBF-LB process. In one way or another, they all try to reduce the main input parameters to a single parameter that describes the energy density in the process, while the *predicted* output response is usually melt pool geometry, although correlations to other output properties have also been studied. The approaches were originally developed and studied in the context of (laser) welding, except for the volumetric energy density *VED*, which is a concept specifically introduced for the PBF-LB process. It is the only one of the models that considers hatch distance and layer thickness; the others are basically just models of a singular melt pool (i.e. weld).

For this thesis, line energy (*LE*) was used in Publication I in the design of experiments as guidance when selecting laser power scanning speed pairs to produce various types of melting conditions, from conduction to transition and keyhole mode. As only laser power and scanning speed were varied, the most simplified metric, line energy, is enough to characterize the changes in input energy.

Power density (*PD*), energy density (*ED*), volumetric energy density (*VED*), and normalized enthalpy ($\Delta H/h_s$) were considered in Publication IV, where the laser beam diameter at the work plane and hatch distance were also varied. Publication IV assessed how well the simplified energy density metrics correlate with melt pool geometry in situations where the focal point position (and hence beam diameter at the work plane) is varied. In addition to the analytical models of energy density, a non-analytical energy density metric named normalized thermal energy density (TED^*) is introduced in this thesis. This metric is based on the melt pool monitoring system (see chapters 2.7.2 and 3.2.3), specifically the wide-spectrum photodiode signal output as a descriptor of the total energy density in the process, divided by the beam area term. This metric is completely different in nature to the analytical ones, as it is a measurement-based metric. Therefore, it lacks predictive power, but instead provides the power to detect variations during the process, which is much more valuable in the scope of this thesis. Furthermore, as it is based on direct and continuous measurement of the output emissions of thermal energy from the melt pool, it is free of assumptions and simplifications, and inherently also incorporates non-constant and highly non-linear input energy conditions, which are not captured by the simplified analytical equations. The normalized thermal energy density is intended as a metric for *quality assurance*, not as a predictive design metric.

Line energy [J/mm], a concept so old and simple it requires no reference:

$$LE = \frac{P}{v} \tag{1}$$

, where P is laser power and v is scanning speed.

Power density [W/mm^2] as defined, for example, in [91]:

$$PD = \frac{P}{\pi a^2} \tag{2}$$

, where a is laser beam diameter (at the work plane).

Energy density [J/mm^2] as defined in [92]:

$$ED = \frac{PD}{v} = \frac{P}{v\pi a^2} \tag{3}$$

Normalized enthalpy [-] as introduced by Hann et al. [93]:

$$\overline{\Delta H} = \frac{\Delta H}{h_s} = \frac{\alpha P}{\rho(C\Delta T + L_m)\sqrt{\pi a^3 v D}} \quad (4)$$

, where α is absorptivity, ρ is density, C is specific heat capacity, ΔT is the difference between initial and melting temperature, L_m is the latent heat of melting, and D is the thermal diffusivity of the processed material. The normalized enthalpy essentially introduces material properties to the *ED* equation and relates the heat dissipation in the material to the input energy.

Volumetric energy density [J/mm^3] as defined in Thijs et al. [94]:

$$VED = \frac{P}{vhLT} \quad (5)$$

, where h is hatch distance and LT is layer thickness. As the volumetric energy density considers the hatch distance and layer thickness, it is essentially an addition of the hatch distance and layer thickness to the line energy, and hence represents not only the heat input along a single weld [J/mm], but rather the energy input to the volume of the material [J/mm^3].

The energy density models presented above are not the only such models developed in attempts to predict the melt pool geometry based on the input laser and material parameters. Naderi et al. [95] and Weaver et al. [96] have recently studied the fidelity of other, slightly more elaborate scaling laws that have been proposed for the PBF-LB process. These scaling laws are still analytical models which all consider the dimensionless parameter $\Delta H/h_s$ and model the energy balance in the process based on simplifications, omitting many of the relevant physical processes involved and treating most, in some cases all, of the inputs and outputs as constants. Therefore, they lack the ability to capture *variation*s in the process, and for quality assurance purposes, control of variance is key. Naderi et al. [95] and Weaver et al. [96] highlighted this, as the errors in the predicted melt pool depths were generally on the order of 50−100% when modelling the absorptivity as a constant. The errors were reduced to around 35% when a non-constant absorption coefficient was included in the model.

Therefore, in this thesis a new approach to characterizing the energy balance of the process is taken, called the normalized thermal energy density, defined as:

$$TED^* = \frac{k*\Phi_\lambda}{\pi a^2} = \frac{PD_I}{\pi a^2} = \frac{TED}{\pi a^2} \quad (6)$$

, where Φ_λ is the total radiant flux emitted from the object surface as a function of wavelength as derived from Planck's Law. This radiation is measured by a co-axial photodiode in the melt pool monitoring system, hence the photodiode output signal intensity (PD_I) represents the total electromagnetic radiation that was emitted by the object (the melt pool). The spectral responsivity of the photodiode used, and attenuation of the signal by e.g. optics between the source and the sensor (represented by the factor k), have an impact on the spectral emissions that the sensor captures; nevertheless, the sensor output is an aggregate representation of it. This aggregate representation of the spectral radiance from the melt pool, e.g., the thermal energy density emitted from it, is called *TED*. TED^* is *TED* normalized by the size of the emitting object, represented in this case by the laser beam area at the work plane πa^2.

Using a blackbody calibration source, one could calibrate a system to be able to convert the photodiode signal output to physical, real temperature; however, in this thesis the photodiode output (voltage) divided by the beam area is used as the metric. Hence, the metric only has arbitrary units. Further development of the metric could include conversion of the photodiode signal output to absolute temperature, allowing SI-metric value units for the thermal energy density *TED* to be derived. This conversion could be done following the approach proposed by Lane et al. [97], for example.

2.7 Process monitoring for quality assurance

As discussed in the previous chapters, the available, controllable input parameters in the machines may not always provide sufficient control of the relevant processing conditions, as the control parameters are surrogates, or intermediate to what needs to be controlled. In the PBF-LB process, the fundamental unit processes that need to be controlled are the properties of the deposited powder layer and the melt pool. For example, the operator cannot set a value for a *melt pool geometry* or *temperature profile* input parameter, even though these are the conditions that truly determine the output from the process. To influence these conditions, the operator has to adjust the laser power or scanning speed (and possibly other parameters) instead. Similarly, *packing density* and *homogeneity of the powder layer* are fundamental properties of the deposited powder layer that we would like to control; however, the operator can only adjust the intermediate re-coating parameters. To acquire more direct information on these fundamental process conditions, the utilization of in-process monitoring techniques has been pursued.

Several process monitoring techniques have been applied to the PBF-LB process, with varying levels of success and technological maturity [98]. In this thesis, two approaches are presented in more detail as they were applied in the experimental part of this thesis. These are powder bed imaging and melt pool monitoring.

2.7.1 Powder bed imaging

The acquisition of images of the powder bed utilizing optical cameras was one of the earliest approaches to monitoring the PBF-LB process. Using such images, two important process conditions can be monitored: the appearance of the spread powder layer, and after selective laser melting, the appearance of the melted surface of the part. Among others, Abdelrahman et al. [99] and Lu et al. [100] used optical cameras positioned off-axis in relation to the powder bed to monitor the surface quality of the melted parts. The main challenges with cameras positioned off-axis are related to the acquisition of undistorted images, at high resolutions, and covering the entire build area while maintaining uniform illumination conditions.

Line cameras provide a promising solution to many of these challenges. Line cameras can be mounted on-axis in relation to the powder bed by integrating them directly into the moving re-coater system. In this manner, undistorted, high-resolution images with constant illumination over the build area can be obtained. Fischer et al. [101] used such an approach to obtain high resolution (5.97 µm/px) images while maintaining a practically relevant re-coater speed (100 mm/s). From the acquired powder bed images, their first study [101] analyzed the part surfaces as a function of the laser parameters, while in their second study the images were used to train neural networks to identify defects in the spread powder layers [102].

Pedersen et al. [103] demonstrated the use of a contact image sensor (CIS), taken from an office flatbed scanner, for powder bed imaging. Tan-Phuc Le et al. [104][105][106] took the approach further by performing comprehensive studies on the use of a CIS for powder bed imaging. They developed quality metrics based on image analysis conducted on the images acquired of the powder layers and melted surfaces. Their setup was able to capture high-resolution (1200 dpi) images in color. However, they reported that it took approximately a minute to image each layer. The slow capture frequency of the consumer-grade CIS they used was the main drawback of their setup, as it would severely increase build times in actual production. To overcome this limitation, Yang et al. [107] then integrated an industrial-grade high-speed CIS into a PBF-LB machine to acquire high-resolution (1200 dpi, i.e. 21 µm/px) images at a high (95 mm/s) linear transverse speed. This corresponded to less than 2 s to image the whole layer of the SLM 125 HL PBF machine used. This setup was used in Publication III of this thesis, and the details are provided in Chapter 3.2.3.

2.7.2 Melt pool monitoring

The most fundamental unit process to monitor in the PBF-LB process is the selective laser melting of the deposited powder layer. One could argue that even flaws in the deposited powder layer, if severe enough to result in flaws in the actual part, would also somehow show as deviations in the melting process. Hence the monitoring of the fundamental unit, the melt pool, could capture all the relevant process events simultaneously. Therefore, significant efforts have been directed towards monitoring the conditions at the melt pool, an approach collectively called melt pool monitoring (MPM). The melt pool emits radiation at various wavelengths on the electromagnetic spectrum, and to monitor this radiation various cameras have been utilized, from "normal" cameras sensitive to visible wavelengths to infrared thermal cameras which capture more than visible light. Many of today's commercial MPM systems utilize photodiodes as their main sensors due to their high temporal sampling frequency, wide available spectrum, and lower cost than camera-based systems. Importantly, they offer all of this combined with significantly smaller data sizes compared to cameras, as photodiodes provide only a one-dimensional numeric output.

The foundational work on the usage of both cameras and photodiodes mounted on-axis in the optical path of the PBF-LB system to monitor and even control the process via a feedback loop back to the laser parameters was conducted by the group led by Jean-Pierre Kruth in KU Leuven [108][109][110]. For data analysis and visualization, they also developed the approach of mapping the photodiode signal intensity to a 2D grid along with the simultaneously recorded scanner x-y position, to essentially generate layer-based images of the signal. This approach has some limitations and Reijonen et al. [111] preferred to work with the time-based raw signal and assign it to all the parts on the build area at the data-structure level for further analysis. This approach was utilized in Publication IV of this thesis, and details of the MPM setup used are explained in Section 3.2.3.

Mercelis [108] has previously shown that the photodiode signal response is sensitive to various deviations in the melting conditions, and that when the optical setup is such that the field-of-view of the sensor is larger than the melt pool, the photodiode output correlates with the melt pool area in addition to temperature. This is understandable, as photodiodes are essentially photon counters, and both the size of the emitting object and its temperature will influence the number of photons emitted. The third important factor in terms of the photodiode signal response is any optical obstacles, such as fumes and spatter in the case of the PBF-LB process, between the emitting source and the sensor [112][113]. Stutzman et al. [114] linked this to the removal of the by-products, showing that the shielding gas flow speed has an influence on a narrow band photodiode signal. Most recently, Reijonen established the relationships between shielding gas flow speed and photodiode signal

for narrow and wide-spectrum bands at various laser speed and power combinations [115].

As the photodiode signal response is sensitive to 1) melt pool temperature, 2) melt pool area, and even 3) shielding gas flow conditions, it provides an excellent method of monitoring all the important conditions present at the melt pool. The photodiode signal may therefore provide a means for quality assurance that is sensitive not only to the conditions of the set input process parameters, but also to stochastic variations in the melting conditions caused by factors that are not captured by the deterministic process models presented in Section 2.6. Therefore, instead of using one of the energy density parameters *LE, PD, ED, VED*, or $\Delta H/h_s$, the actual energy density emitted from the melt pool, as captured by the photodiode, could provide a more comprehensive singular metric to characterize the melt pool conditions. The potential of utilizing process monitoring for quality assurance has also been recognized by standardization organizations [116]. In this thesis, powder bed monitoring with a contact image sensor was utilized in Publication III and melt pool monitoring with co-axial photodiodes in Publication IV to study their potential to capture process deviations caused by *machine architecture-defined* process parameters, and link them to output part quality.

3 Materials and Methods

3.1 Materials

316L (1.4404) stainless steel was the material used to conduct all the experiments. Depending on the publication, the specific powder lot and hence particle size distributions of the powders varied slightly. The powder was included as an intended variable only in Publication II, where two separate powders with different particle size distributions (PSD) and chemical compositions (although nominally according to the same 316L standard) were used. A summary of the powders used in the studies is provided in **Table 1**. Details of the properties of the two powders used in Publication II are shown in **Figure 12**. The chemical compositions are included as provided in the powder material certificates, and as measured from solidified material processed with the PBF-LB machines from the powders, denoted as EOS/SLM-EOSp/SLMp.

All specimens were produced on stainless steel building platforms with thicknesses of between 18 and 25 mm.

Argon was used as the shielding gas in all the experiments. The oxygen content in the build chamber was maintained at < 1000 ppm and the over pressure in the build chamber at 12 mbar over atmospheric pressure.

Table 1. Properties of the powders used in the studies.

Powder lot	Publication	Supplier	Production method	D_{10} / D_{50} / D_{90}
201500481	I	SLM Solutions	Gas atomization	23.4 / 37.6 / 59.7 µm
2019001005	II	SLM Solutions	Gas atomization	16.7 / 26.1 / 40.4 µm
S191901	II	EOS	Gas atomization	21.4 / 32.5 / 48.8 µm
UK85952	III, IV	Carpenter Additive	Gas atomization	19.4 / 30.5 / 47.7 µm

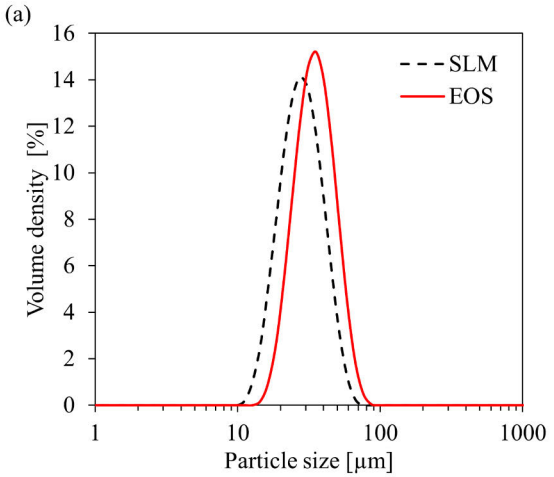

(d)

	EOS			SLM		
Element	**Powder**	**EOS-EOSp**	**SLM-EOSp**	**Powder**	**SLM-SLMp**	**EOS-SLMp**
Fe	63.5	Bal.	Bal.	66.1	Bal.	Bal.
Cr	17.9	18.0	17.8	17.7	17.6	17.6
Ni	14.0	14.2	13.9	12.6	12.5	13.2
Cu	≤0.01	0.03	0.02	-	0.02	0.02
Mn	1.5	1.36	1.44	0.5	0.48	0.47
Si	0.25	0.24	0.23	0.67	0.73	0.73
Mo	2.7	3.00	2.98	2.3	2.43	2.46
Al	-	0.003	0.003	-	0.003	0.003
W	-	0.02	0.02	-	0.02	0.02
V	-	0.048	0.027	-	0.027	0.027
Ti	-	0.002	0.003	-	0.003	0.003
Co	-	0.012	0.027	-	0.013	0.027
C	0.005	<0.010	<0.010	0.016	0.010	0.010
S	0.005	0.003	0.004	0.005	0.006	0.004
P	<0.01	0.013	0.013	0.008	0.010	0.010
N	0.07	0.066	0.066	0.09	0.084	0.085
O	-	0.058	0.051	0.03	0.026	0.023

Figure 12. (a) Particle size distributions, (b–c) particle morphologies, and (d) chemical compositions of the two different powders used in Publication II.

3.2 PBF-LB experiments

3.2.1 Equipment

A commercially available PBF-LB machine model SLM 125 HL from SLM Solutions GmbH (model year 2014) was used in all the experiments. The laser source was an IPG-YLR-400-SM fiber laser with a central wavelength of 1070 nm. The

nominal maximum output power of the laser was 400 W. Upon leaving the process fiber, the laser beam was directed to an IPG Photonics P30-002384 F=70 mm collimator to produce a 25 mm diameter collimated beam. This beam was focused with a Scanlab VarioScan 40 dynamic focusing unit and positioned on the work plane with a Scanlab Intelliscan 25 galvanometer scanner. The nominal maximum build volume of the system was 125x125x125 mm.

For Publication II, a commercially available PBF-LB machine model EOS M 290 from EOS GmbH was used in addition to the SLM 125 HL to compare the properties of parts produced on different machines. The EOS M 290 is also equipped with a 400 W Ytterbium fiber laser, which uses an F-theta lens instead of a dynamic focusing unit to maintain the focus position at the work plane throughout the whole build area. Both machines have a nominal 80 µm laser beam focal point size. The nominal maximum build volume of the EOS M 290 system is 250x250x325 mm.

For Publication I, a VELOCICALC 9565 hot-wire anemometer coupled with a 964 probe from TSI Incorporated was used to measure the shielding gas flow velocities above the SLM 125 HL system building platform. The equipment is reported to have a measurement accuracy of ±3% of the reading or ±0.015 m/s, whichever is greater. This was used to establish the correlation between the flow speed at the build area and the reference value that is used for controlling the shielding gas flow speed, which in the case of the SLM 125 HL system used in the experiments is the gas flow speed as measured at the inlet pipe, after the circulation pump.

For Publication II, post-process heat treatments were conducted on the specimens after the PBF-LB process. All specimens were first stress-relieved (SR) while still attached to the building platform at 650°C for 2 h in an argon atmosphere, followed by air cooling. One part (1/3) of the specimens was solution annealed (SA) in accordance with the AMS 2759 standard, namely at 1066°C for 1 h in an argon atmosphere, followed by air cooling. Second part (1/3) of the specimens was subjected to hot isostatic pressing (HIP) at 1150°C for 4 h in a 100 MPa argon atmosphere, followed by furnace cooling to 180°C at a rate of 100°C/min. The third set of parts (1/3) were left in the stress-relieved condition, in order to have equal shares of identical specimens in the SR, SA, and HIP conditions.

In Publication III, two different commercially available re-coater blade types were compared. The first was the standard polymer composite blade (i.e. soft) used in the SLM 125 HL system (part number: 843000902), which has a rounded tip profile. The second was the standard high speed steel blade (i.e. hard) used in EOS M 290 machines (part number: 2200-4073), which has a sharp tip profile.

For Publication IV, the laser beam diameters and intensity distributions at the work plane corresponding to the different focal point positions studied were measured with a model FBP-1KF-5.3-3x focus beam profiler from CINOGY

Technologies GmbH. The data was collected with RayCi Pro version 2.7.8 software from the same company. A spectrometer (Ocean Insight HR4PRO with an extended wavelength range of 200−1100 nm) was used to conduct spectral analysis on the melt pool monitoring systems' sensor locations to verify which wavelengths at what intensities were collected by each sensor. The data was collected using OceanView software version 2.0.

Electric discharge machining was used after all the experiments to remove the specimens from the building platform.

3.2.2 Experimental designs

In this chapter the experimental PBF-LB build layouts, specimen geometries, and processing parameters, i.e. the experimental designs that were conceived to test each of the hypotheses in the publications, are presented. Unless otherwise stated for a specific publication where one or more of the following were intended variables, the following nominal processing conditions using the SLM 125 HL machine apply:

1. Shielding gas flow speed was set close to maximum, with the objective of producing similar, high flow speeds in all cases. The adjustable control in the machine is the shielding gas flow circulation pump speed, which was between 84−94 % of full power in the experiments. The flow speed was monitored with a flow meter placed at the inlet pipe, after the circulation pump. The filter conditions have an impact on the flow, hence the variation in the pumping speeds.
2. No post-process heat treatments were applied.
3. A bi-directional, soft polymer-composite re-coater blade with a rounded tip profile was used.
    - The re-coater motor speed was set to 1000 rpm (corresponding to ~217 mm/s linear spreading speed).
    - Layer thickness was set to 30 µm.
    - Powder dosage factors, which determine the volume of powder deposited on each layer, were set to:
        - DPC factor = 17.
        - Minimum number of grooves = 1.7.
        - Overdosage factor = 1.25.
4. The focal point position was set to 0 mm.

In modern PBF-LB machines, the scanning strategy is a complicated parameter to define in sufficient detail that someone else could replicate the experiment. The difficulty comes from it not being a single value nor a constant within a build, as it is typically rotated between layers and changes along the cross-section and position of the part based on a logic or algorithm usually defined by the machine OEM. For all the experiments conducted with the SLM 125 HL machine in this thesis, the build files were generated with Materialise Magics software coupled with the SLM Solutions Build Processor. The default parameter set file developed by the machine OEM for the 316L material, with 30 µm layer thickness and utilizing the so-called Stripes scanning strategy, was used as the basis in the design of all the experiments.

In the context of this thesis, scanning strategy refers to all the extra parameters that define the scanning sequence and orientation of the laser vectors, both within a part and between parts. Laser parameters refer to the laser power, scanning speed, hatch distance, and focal point position. In addition to the so-called core vectors that are used to melt the bulk of the material, there are separate vector types for different features of the parts such as borders, up-skin, down-skin, supports, etc. In total, the parameter set file used contained 18 vector types, and for all of them the individual laser melting parameters are defined. In total, there are over 300 settings in the parameter file that could be modified.

In the experiments for this thesis, only the core vector parameters were varied, with the parameters of the other vector types kept constant. Unless explicitly stated, whenever laser power, scanning speed, hatch distance, or focal point position are discussed, they refer to the values of the core vector parameters. From the over 300 settings in the parameter file that could be modified, only four of them were varied as intended variables studied for this thesis: laser power, scanning speed, hatch distance, and focal point position. Other modifications, if any, made to the standard parameter set are explicitly mentioned when describing the experiment in question.

Figure 13 illustrates the main concept of the scanning strategy used. The scanning sequence between parts on the building platform always progresses from left to right, that is, against the shielding gas flow. Within a part, the borders are scanned first, then the fill contour, and finally the core. The core vectors are bi-directional. Between layers, the scanning orientation of the core vectors is rotated. The algorithm behind the layer rotation is, to the authors' knowledge, proprietary information of the machine OEM, and hence not reported here. However, the purpose of the rotation is to reduce residual stresses and porosity, and some angles in relation to the shielding gas flow direction are prohibited. The output is a seemingly randomized orientation between the layers, with the angles in relation to the positive y-direction always falling in the range $-45° < \omega < +45°$.

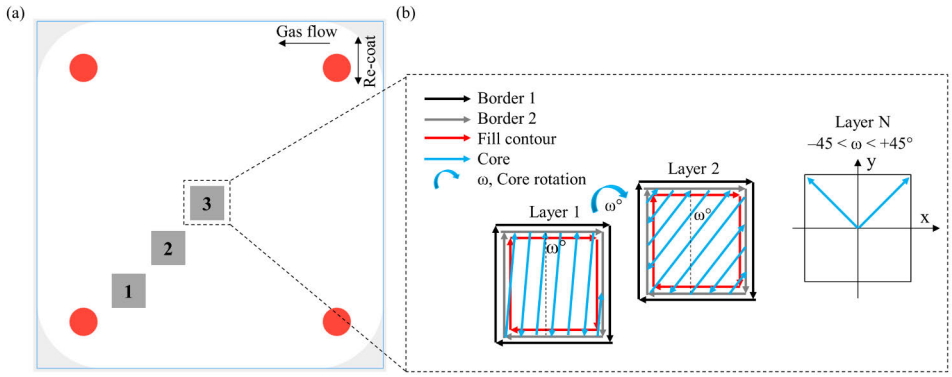

Figure 13. Illustration of (a) the scanning sequence between parts on the building platform and (b) the scanning strategy within a part used in the experiments. Image: Joni Reijonen.

Unless otherwise stated for a specific experiment, the following nominal laser parameters for the other vector types utilized apply:

1. Border vectors:
    - Number of borders: 2
    - Border distance: 0.09 mm
    - Laser power: 100 W
    - Scanning speed: 400 mm/s
    - Focal point position: 0 mm
2. Fill contour vectors:
    - Number of fill contours: 1
    - Fill contour distance: 0.1 mm
    - Laser power: 125 W
    - Scanning speed: 500 mm/s
    - Focal point position: 0 mm

Another minor-sounding yet crucial aspect of the scanning strategy that is defined by the scanner hardware and its control software is how the start and end points of the vectors are treated. In laser scanning of any kind using galvanometer scanners, the basic commands are JUMP and MARK. With a JUMP command, the laser is OFF, and the scanner mirrors move to the defined x-y position. Next comes the MARK command, which involves movement at the defined scanning speed from the start to end x-y position while the laser is ON. As it takes time for the scanner

mirrors to accelerate to the set scanning speed in the beginning and then decelerate at the end, without any compensation the scanning speed would not be constant at the beginnings and ends of the vectors. As laser power remains constant, the energy density increases, leading to excessive keyhole porosity at the start/end points [117]. To avoid this, several strategies can be applied; in this thesis, the Sky Writing strategy developed by Scanlab for their scanners was used in all the experiments. **Figure 14** illustrates how Sky Writing works. In short, additional run-in and run-out phases are added before and after each MARK command to allow sufficient time for the scanner to reach the set speed before the laser is activated.

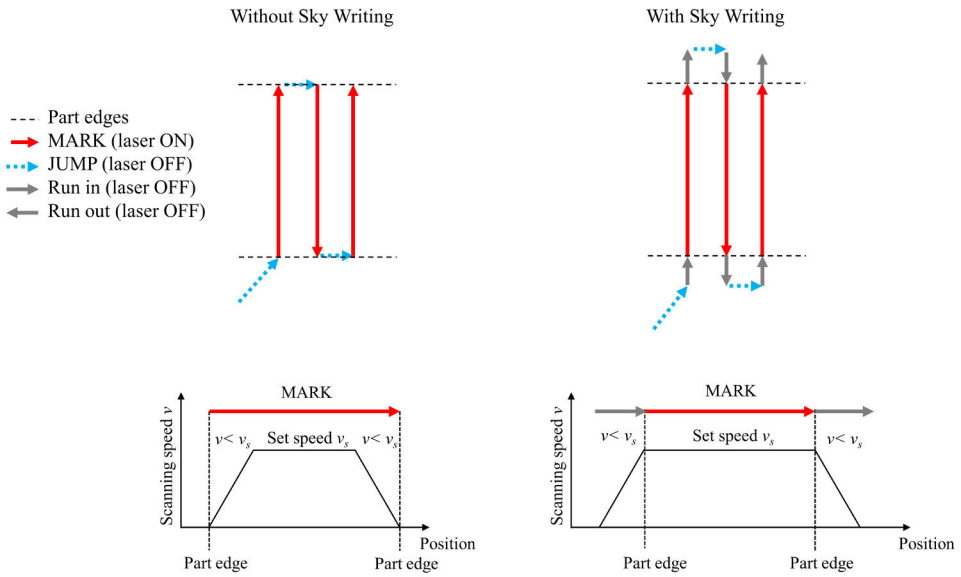

Figure 14. Illustration of the so-called Sky Writing setting used to add run-in and run-out phases at the beginning and end of each MARK vector to ensure constant scanning speed during the laser melting. Image: Joni Reijonen.

Publication I

For Publication I, an experimental build job was designed to study the effect of the shielding gas flow speed on melt pool geometry and part porosity. The build layout is shown in **Figure 15**. A stair step-type test specimen was designed to test multiple gas flow speeds on a single build job. The shielding gas flow speed was varied along the build height in six steps (4.0, 3.5, 3.0, 2.5, 2.0, 1.0 m/s). With each gas flow setting, 100 layers (i.e. 3 mm at 30 µm layer thickness) were processed. During each gas flow setting, three single scan tracks were produced on the stair-step feature (see

Figure 15 (c)) for melt pool dimensional analysis. An elevated platform pre-heat temperature of 200°C was used. The re-coater motor speed was set to 1200 rpm.

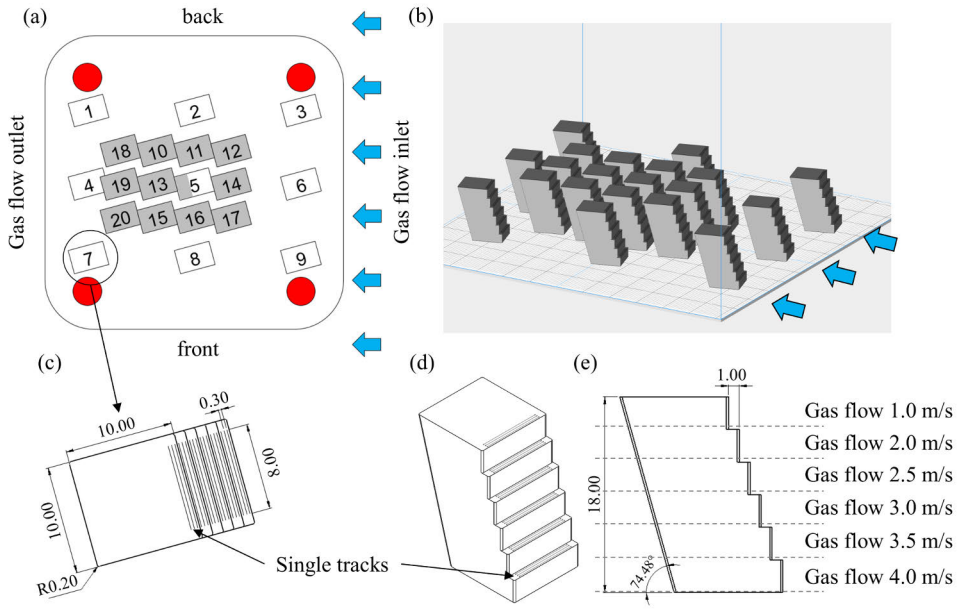

Figure 15. Build layout for Publication I: (a–b) specimen placement on the building platform, (c–e) specimen geometry, dimensions, single track positions, and gas flow steps.

For specimens 1–9, constant laser parameters were applied, as the location on the building platform was the intended variable. For specimens 10–20 the laser parameters were varied within a wide range of energy densities. Specimen number 5 (marked as grey/white in **Figure 15**) was used for both the location and energy density variation series. **Table 2** shows the varied parameters for each specimen. The simplest of the energy density metrics, line energy P/v, was used in Publication I, as only the laser power and scanning speed were variables in the single tracks.

The laser parameters for specimens 10–20 were selected based on observations by Trapp et al. [118] to produce conduction (<0.1 J/mm), transition (0.1–0.3 J/mm), and keyhole (>0.3 J/mm) mode melting conditions.

Table 2. List of specimens and corresponding process parameters in Publication I.

ID	Power [W]	Speed [mm/s]	Hatch [mm]	Line Energy [J/mm]	Purpose in relation to gas flow speed hypothesis
1−9	175	750	0.12	0.23	Effect of location on platform
5	175	750	0.12	0.23	Effect in transition mode
10	100	500	0.12	0.20	Effect in transition mode
11	100	750	0.12	0.13	Effect in transition mode
12	100	1000	0.12	0.10	Effect in conduction mode
13	175	500	0.12	0.35	Effect in keyhole mode
14	175	1000	0.12	0.18	Effect in transition mode
15	250	500	0.12	0.50	Effect in keyhole mode
16	250	750	0.12	0.33	Effect in keyhole mode
17	250	1000	0.12	0.25	Effect in transition mode
18	70	500	0.08	0.14	Effect in transition mode
19	50	500	0.08	0.10	Effect in conduction mode
20	30	500	0.08	0.06	Effect in conduction mode

Publication II

For Publication II, two PBF-LB machines and two different powders were used to produce a total of four identical sets of specimens, as listed in **Table 3**. The experiment was designed to 1) quantify the variability in mechanical properties when the machine and powder are varied and 2) assess whether standardized post-process heat treatments can reduce the variations in part properties. The build layouts and specimen geometries are shown in **Figure 16**. The additively manufactured blanks for the machining of the final test specimen geometries were 11x110 mm cylinder bars for tensile and 57x12x12 mm square bars for impact testing respectively. A default scanning strategy and process parameters intended for use with 316L stainless steel material by the respective machine manufacturers were used. The purpose was to use the process parameters recommended by the machine manufacturer as-is, with no attempt to set identical conditions for both machines. For the EOS machine, this included:

- Process parameter set: 316L_SurfaceM291 1.10
- Re-coater blade type: ceramic, part number 2200-4073
- Platform pre-heat temperature: 80°C
- Layer thickness: 20 µm.

For the SLM Solutions machine it inlcuded:

- Process parameter set: 316L_SLM_MBP3.0_30_CE1_400W_Stripes_V1.1
- Re-coater blade type: polymer-composite, part number 843000902
- Platform pre-heat temperature: 100°C
- Layer thickness: 30 µm.

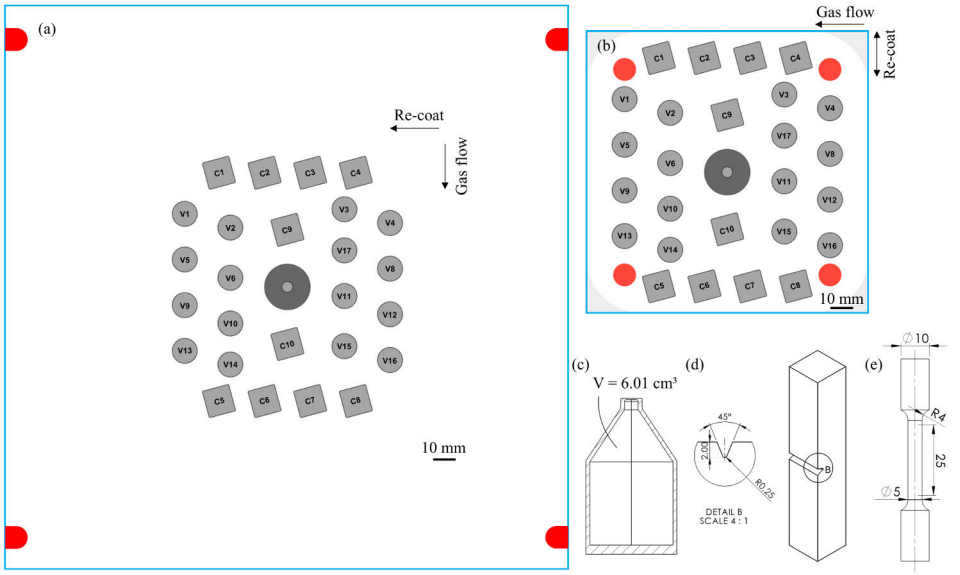

Figure 16. Build layouts in Publication II: specimen placement on the (a) EOS M290 and (b) SLM 125 building platform, and (c-e) test specimen geometries and dimensions of main features.

Table 3. List of specimens and corresponding process parameters in Publication II.

Build ID	Part IDs	Specimen type	HT Conditions	Powder	Purpose in relation to heat-treatment hypothesis
SLM-347	V1−16	Tensile	SR, SA, HIP	SLMp	SLM machine, SLM powder
SLM-347	C1−10	Impact	SR, SA, HIP	SLMp	SLM machine, SLM powder
SLM-347	SLM-347	Powder canister	SR	SLMp	SLM machine, SLM powder
SLM-348	V1−16	Tensile	SR, SA, HIP	EOSp	SLM machine, EOS powder
SLM-348	C1−10	Impact	SR, SA, HIP	EOSp	SLM machine, EOS powder
SLM-348	SLM-348	Powder canister	SR	EOSp	SLM machine, EOS powder
EOS-1	V1−16	Tensile	SR, SA, HIP	EOSp	EOS machine, EOS powder
EOS-1	C1−10	Impact	SR, SA, HIP	EOSp	EOS machine, EOS powder
EOS-1	EOS-1	Powder canister	SR	EOSp	EOS machine, EOS powder
EOS-2	V1−16	Tensile	SR, SA, HIP	SLMp	EOS machine, SLM powder
EOS-2	C1−10	Impact	SR, SA, HIP	SLMp	EOS machine, SLM powder
EOS-2	EOS-2	Powder canister	SR	SLMp	EOS machine, SLM powder

Publication III

For Publication III, an experiment was designed to study the impact of the type of re-coater blade used on the porosity and processability of challenging geometrical features. Two otherwise identical build jobs were carried out, with the re-coater blade as the only intended variable. The challenging features in the specimens were thin walls (wall thickness 2.0, 1.5, 1.0, 0.7, 0.5, and 0.3 mm) and overhangs (inclination of 45°, 40°, 35°, 30°, and 25° relative to the building platform). Three specimens with thin walls were included in the build job and placed at different (0°, 45°, and 90°) orientations in relation to the re-coating direction. Two specimens with overhangs were included in the build job, and they were placed at two different (0°, 90°) orientations in relation to the re-coating direction. The build layout, along with the specimen geometries and orientations, is shown in **Figure 17**. An image showing the re-coater tip profiles of the blades used is also included.

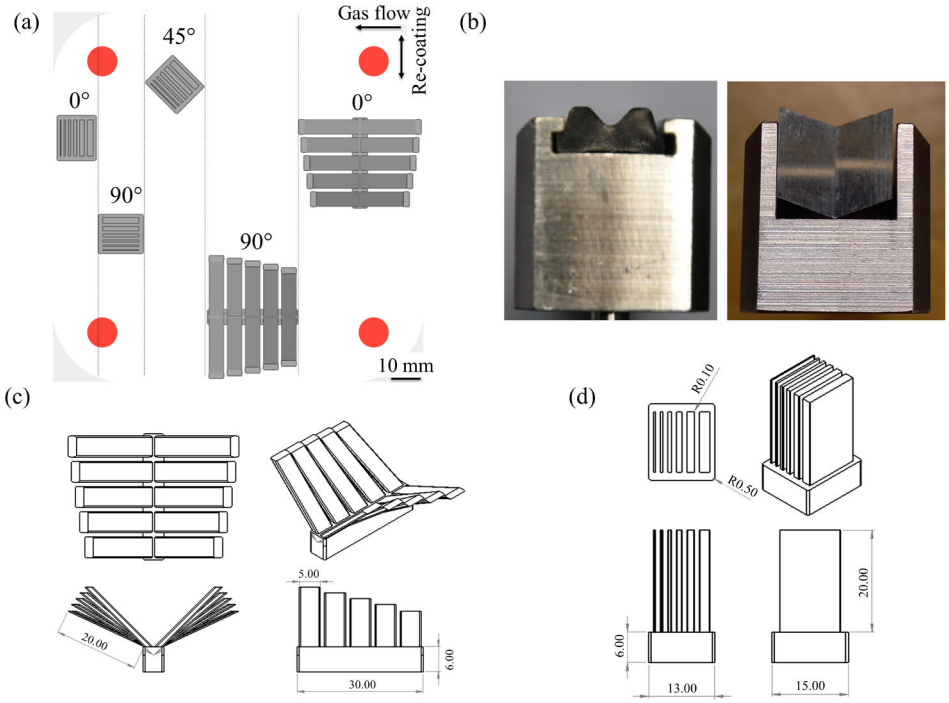

Figure 17. Build layout in Publication III: (a) specimen placement and orientations on the building platform, (b) tip profiles of the soft and hard re-coater blades used, and (c–d) specimen geometries and main dimensions. The dashed lines in (a) indicate separate sections for each specimen in relation to the re-coating direction, so that any collision between the re-coater and one of the specimens would not harm the others.

Table 4 lists all the specimens in the experiment. The core laser melting parameters were kept constant in the experiment, with the laser power set at 200 W, scanning speed 800 mm/s, and hatch distance 0.12 mm for all specimens. An elevated platform pre-heat temperature was not used. The re-coater motor speed was reduced to 448 rpm as necessitated by the powder bed imaging setup (see Section 3.2.3) to acquire high-resolution, non-distorted images.

Table 4. List of specimens and corresponding process parameters in Publication III.

Build ID	Part ID	Re-coater blade type	Geometry	Feature sizes	Orien-tation	Purpose in relation to re-coater blade hypothesis
461	1	soft	Thin walls	0.3, 0.5, 0.7, 1.0, 1.5, 2.0 mm	0°	Thin walls parallel to re-coating direction
461	2	soft	Thin walls	0.3, 0.5, 0.7, 1.0, 1.5, 2.0 mm	45°	Thin walls at 45° angle to re-coating direction
461	3	soft	Thin walls	0.3, 0.5, 0.7, 1.0, 1.5, 2.0 mm	90°	Thin walls horizontal to re-coating direction
461	4	soft	Overhangs	45°, 40°, 35°, 30°, 25°	0°	Overhangs parallel to re-coating direction
461	5	hard	Overhangs	45°, 40°, 35°, 30°, 25°	90°	Overhangs horizontal to re-coating direction
463	1	hard	Thin walls	0.3, 0.5, 0.7, 1.0, 1.5, 2.0 mm	0°	Thin walls parallel to re-coating direction
463	2	hard	Thin walls	0.3, 0.5, 0.7, 1.0, 1.5, 2.0 mm	45°	Thin walls at 45° angle to re-coating direction
463	3	hard	Thin walls	0.3, 0.5, 0.7, 1.0, 1.5, 2.0 mm	90°	Thin walls horizontal to re-coating direction
463	4	hard	Overhangs	45°, 40°, 35°, 30°, 25°	0°	Overhangs parallel to re-coating direction
463	5	hard	Overhangs	45°, 40°, 35°, 30°, 25°	90°	Overhangs horizontal to re-coating direction

Publication IV

For Publication IV, an experimental build job was designed to study the impact of the laser focal point position on the quality of parts produced. The build layout is shown in **Figure 18**. An elevated platform pre-heat temperature was not used. Border and contour vectors were removed from the scanning strategy, leaving only the core vectors.

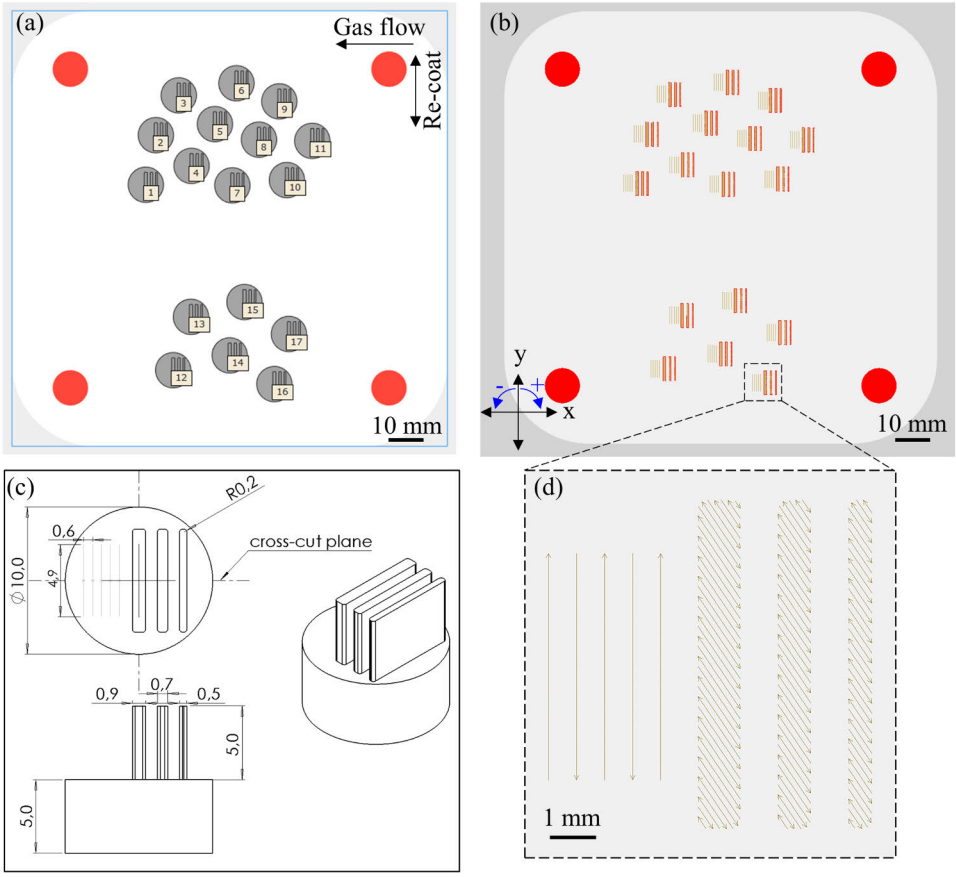

Figure 18. Build layout in Publication IV: (a) specimen placement on the building platform, (b) placement of the single tracks on layer number 168, (c) specimen geometry and main dimensions, and (d) detailed view of the single tracks and the scanning strategy used with only the core vectors.

For specimens 1−11, the focal point position was the only intended variable. For specimens 12−17 the focal point position was set constant at −3 mm, while the laser beam scanning speed, laser power, and hatch distance were intended variables. **Table 5** lists the parameters used for all the specimens, along with their intended purpose in the design of experiments. The various energy density parameters *VED*, *PD*, *ED*, and $\Delta H/h_s$ were calculated from the laser parameters. To calculate $\Delta H/h_s$ the values used for the material constants were: absorptivity $\alpha = 0.4$, density $\rho = 8.0$ g/cm³, thermal diffusivity $D = 3.5*10^{-6}$ m²/s, specific heat capacity $C = 800$ J/kgK, and latent heat of fusion $L_m = 260$ kJ/kg.

Table 5. List of specimens and corresponding process parameters in Publication IV.

ID	Focus [mm]	Beam diam. [mm]	Power [W]	Speed [mm/s]	Hatch [mm]	VED [J/mm^3]	PD [kW/mm^2]	ED [J/mm^2]	$\Delta H/h_s$	Purpose in relation to focal point position hypothesis
1	−5.0	0.138	200	800	0.12	69.4	13.3	16.7	4.0	Neg. focus position
2	−3.0	0.100	200	800	0.12	69.4	25.6	32.0	6.2	Neg. focus position
3	−2.0	0.085	200	800	0.12	69.4	35.1	43.8	8.1	Neg. focus position
4	−1.0	0.077	200	800	0.12	69.4	42.6	53.2	10.1	Neg. focus position
5	−0.5	0.076	200	800	0.12	69.4	43.7	54.7	10.3	Neg. focus position
6	0.0	0.078	200	800	0.12	69.4	42.3	52.9	10.5	Nominal ref.
7	+0.5	0.085	200	800	0.12	69.4	42.4	52.9	10.3	Pos. focus position
8	+1.0	0.097	200	800	0.12	69.4	35.6	44.5	10.1	Pos. focus position
9	+2.0	0.116	200	800	0.12	69.4	27.1	33.8	8.1	Pos. focus position
10	+3.0	0.156	200	800	0.12	69.4	19.0	23.7	6.2	Pos. focus position
11	+5.0	0.100	200	800	0.12	69.4	10.4	13.0	4.0	Pos. focus position
12	−3.0	0.100	150	600	0.12	69.4	19.2	32.0	5.4	same VED as ref.
13	−3.0	0.100	250	1000	0.12	69.4	32.0	32.0	7.0	same VED as ref.
14	−3.0	0.100	250	800	0.15	69.4	32.0	39.9	7.8	same VED as ref.
15	−3.0	0.100	400	800	0.12	138.9	51.1	63.9	12.4	Same PD, same ED as ref.
16	−3.0	0.100	400	1000	0.12	111.1	51.1	51.1	11.1	Same PD as ref.
17	−3.0	0.100	400	800	0.15	111.1	51.1	63.9	12.4	Same PD, same ED as ref., high hatch

3.2.3 Process monitoring

Publications III and IV included an element of process monitoring, with the purpose of studying the potential of certain process monitoring methods to capture process deviations caused by the studied variables.

For Publication III, a model SWL12R183NDU-211216 CIS contact image sensor (CIS) from Weihai Hualing Opto-Electronics Co., Ltd. combined with a National Instruments model USB-6351 data acquisition module (DAQ) was used to acquire high-resolution (1200 dpi, 21 μm/pixel) layer-based images of the entire re-coated powder bed (scanning width 184 mm) for process monitoring purposes. The DAQ was also connected to the SLM 125 HL control to read the re-coater position, which was used as the trigger signal for image acquisition. The selected CIS sensor

unit had a compact footprint of $l = 200$ mm, $w = 18$ mm, and $h = 14$ mm, and could be mounted to the re-coater of the SLM 125 HL system without blocking any of the active build area or in any way disturbing the build cycle. Furthermore, due to the sufficiently high line-scanning frequency of the sensor of 4.5 kHz, a practically relevant linear re-coating speed of 95 mm/s could still be maintained. As the CIS has a short depth of focus, the blurred, out of focus areas that correspond to locations where the powder layer height deviated from the nominal could be detected. These areas were automatically detected and quantified from the images with a modified Laplacian focus measure operator (FMO), as proposed in [104], and implemented as a Python script. The setup is illustrated in **Figure 19**.

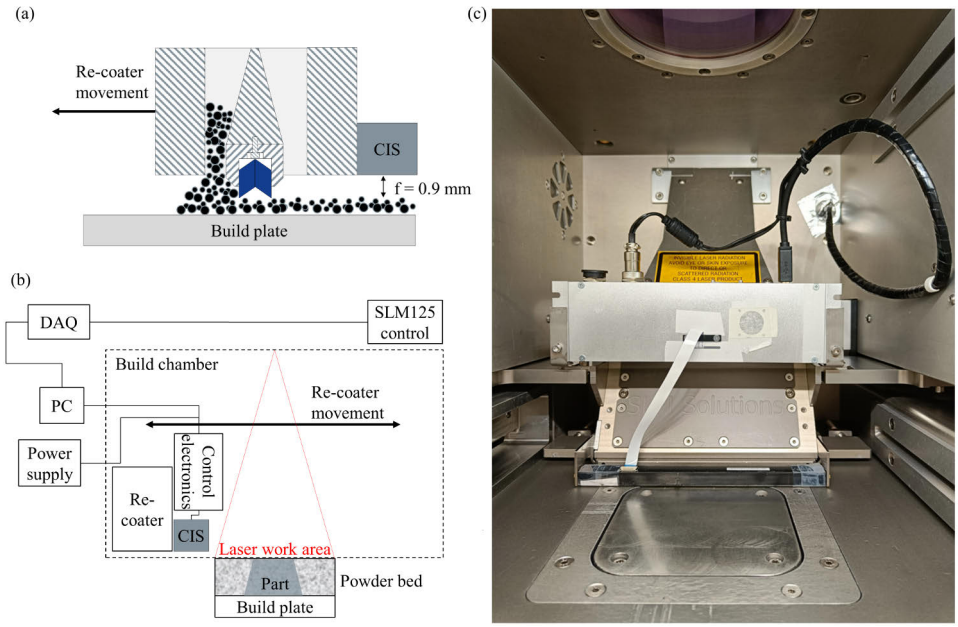

Figure 19. Contact image sensor retrofitted on the re-coating mechanism of the SLM 125 HL PBF-LB system, used for powder bed monitoring for Publication III.

For Publication IV, a SigmaLabs Inc. PrintRite3D melt pool monitoring system was used to capture the thermal emissions from the PBF-LB process. The system was retrofitted on the SLM 125 HL machine via the camera adapter port that is located between the galvanometer scanner and the dynamic focusing unit, as shown in **Figure 20**. The MPM system consists of three photodiodes, named Thermal Energy Density (TED) and Thermal Energy Planck high and low (TEP high and low). The TED sensor monitors a wide range of wavelengths in the visible to near-infrared region for the purpose of capturing the total thermal emissions from the process. The TEP high and low sensors have bandpass filters in front of them to limit

the sensor response to only specific, narrow wavelength bands that are different but close to one another. The ratio between the TEP high and low signal intensities could be utilized as a two-color pyrometer to allow for transfer of the signal response to actual temperature following Planck's law. As the selected wavelengths are close to one another, the emissivity can be assumed to be equal and removed from the equation. For this thesis, the photodiode signal intensities were used as the response metric, without any attempt to convert them into absolute temperatures.

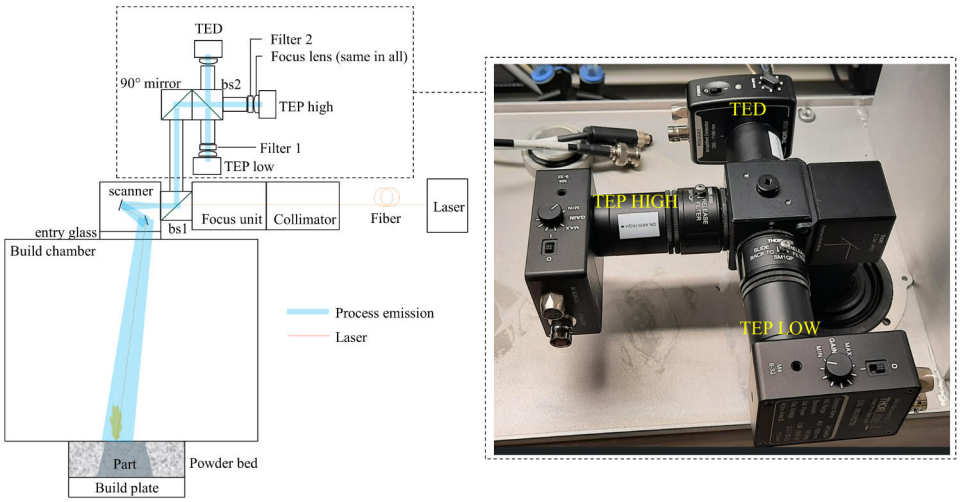

Figure 20. Sigma Labs Printrite3D melt pool monitoring system (dashed) retrofitted on the optical path of the SLM 125 HL PBF-LB system, used for monitoring electromagnetic radiation originating from the melt pool in Publication IV.

Table 6 lists the relevant optical components with the corresponding optical information in the system configuration at the time the experiments were conducted for this thesis. Since then, the hardware has seen some updates.

Table 6. List of optical components in the PrintRite3D MPM system retrofitted on the optical path of the SLM 125 HL PBF-LB system via the camera adapter port.

Component	Model	Nominal optical range
TED	Thorlabs PDA36A2 Si-photodiode	350 – 1100 nm
TEP LOW	Thorlabs APD440A Si-photodiode	400 – 1000 nm
Filter 1 (TEP LOW)	Edmund Optics 65167, OD4, hard coated Bandpass filter	636 ± 5 nm
TEP HIGH	Thorlabs APD440A Si-photodiode	400 – 1000 nm
Filter 2 (TEP HIGH)	Edmund Optics 65170, OD4, hard coated Bandpass filter	650 ± 5 nm
Focus lenses	Thorlabs LA1951-A - N-BK7 Plano-Convex Lens, Ø1", f = 25 mm	AR Coating: 350 – 700 nm
Beam splitter (bs2)	Thorlabs BPD254S-G - Polka Dot Beamsplitter, 1" x 1", B270 Glass	350 nm – 2 µm
Camera adapter (bs1)	Scanlab Camera adapter	1030 – 1110 nm & 450 – 900 nm

3.3 Material testing and characterization

3.3.1 Powder analysis

The powders used were characterized in terms of morphology, internal porosity, particle size distribution (PSD), flowability, and tap/packing density, with varying comprehensiveness depending on the Publication type. At a minimum, the PSD was measured. The most comprehensive powder analysis was conducted for Publication II, where the powder was an intended variable.

The morphology and internal porosity of the powders were qualitatively assessed from SEM images acquired with an SEM 4 Zeiss Ultra Plus in Publication II and a JEOL JSM-636OLV in Publication III. The PSD of the powders was analyzed with laser diffraction using a Malvern Mastersizer 3000.

Powder flowability was measured in Publication II with the Hall-flow test following ISO standard 4490 and the Carney funnel test following ASTM standard B964. Apparent and tap densities were measured according to ASTM standard B212. The powder bed packing density was measured with a specifically designed hollow powder container, as described in [119].

3.3.2 Optical microscopy

A ZEISS Axio Observer Inverted Microscope was used for optical microscopy. Depending on the Publication, porosity, melt pool geometry, and microstructural features were analyzed from the acquired microscopy images.

To measure porosity, the cross-sections of the samples were polished to a mirror finish, after which panorama images with x5 magnification were acquired to capture the complete sample cross-section. The acquired 8-bit grayscale images were processed with ImageJ (GNU General Public License) software. Thresholding was used to convert the images to a binary scale where black corresponded to voids and white to solid material. Identification and classification of defect types was not conducted, rather all voids identified with the method were treated as a singular group of defects, and the total fraction of these defects (i.e. the void fraction) reported as the total porosity. The amount of porosity, or void fraction, within the sample cross-section was calculated using the Particle Analyzer function of the ImageJ software.

After porosity analysis of polished cross-sections, Aqua Regia was used as the etchant to reveal the microstructure and specifically the melt pool boundaries of the single-tracks. Images with x20 and x50 magnifications of the region of interest were acquired and used to measure the melt pool geometry (width, depth, and cross-sectional area) with ImageJ (GNU General Public License) software.

3.3.3 Computed x-ray tomography

For Publications III and IV, xCT was used to identify voids and measure porosity in the specimens. Identification and classification of defect types was not conducted, rather all voids identified with the method were treated as a singular group of defects, and the total fraction of these defects (i.e. the void fraction) reported as the total porosity. In Publication III the xCT data was also used for dimensional analysis. The major advantage of xCT over OM in measuring porosity is that it can be used to analyze the whole 3D volume of the specimen for the presence of voids, instead of only a 2D slice as in optical microscopy. Furthermore, xCT is a non-destructive analysis method. A GE Phoenix v|tome|x s system equipped with a 240 kV direct microfocus tube and either a 1.0 or 0.5 mm Cu filter was used, depending on specimen geometry, to reduce the effect of beam hardening. For Publication III the complex shaped specimens were scanned with helical scanning, while for Publication IV axial scanning was used for the cylindrical samples. ImageJ (GNU General Public License) software was used to analyze the 8-bit TIF image stack that was the output data from the xCT scan. The achievable voxel resolution for the scans depends (among other aspects) on the specimen geometry, and was 7.5 µm for the

cylindrical specimens in Publication IV, and 11 µm for the thin-walled specimens and 16 µm for the overhang specimens in Publication III.

3.3.4 Tensile testing

Tensile testing for Publication II was conducted with an Instron 1185 universal materials testing machine. The strain rate and other testing conditions were in accordance with ISO standard 6892-1:2016 for room temperature testing. The specimens were tested in machined surface condition, with a 5 mm gauge diameter and 25 mm gauge length. Yield strength, ultimate tensile strength, and elongation at fracture were measured in the test. The sample size was N=5.

3.3.5 Impact toughness testing

For Publication II, impact toughness was measured with Charpy-V specimens in machined surface condition, with dimensions 10x10x55 mm and notch dimensioning as required by ISO standard 148-1:2016. Testing was conducted at room temperature using a Losenhausenwerk-MFL 1959 machine with a 300 J impact pendulum. The sample size was N=3.

3.3.6 Scanning electron microscopy

A Zeiss Crossbeam 540 scanning electron microscope (SEM) was used for Publication II. The SEM was equipped with an EDAX Hikari Plus electron backscatter diffraction (EBSD) detector and a solid-state four-quadrant backscatter detector (BSD). BSD images were acquired at a magnification of 50–5000x. EBSD was performed at 500x and 125x magnifications with a step size of 0.3 and 1 µm, respectively. Inversed pole figure (IPF) and kernel average misorientation (KAM) images at a scale of 0–5° were produced from the data using TSL OIM Analysis 8 software. The equipment was used to analyze the microstructure, fracture surfaces, and size/composition of inclusions in the specimens, and their evolution with different heat treatment conditions was compared in Publication II. For microstructural analysis, the cross-sections of the samples were ground and then polished with a 0.05 µm, non-crystallizing amorphous colloidal silica suspension. Fracture surfaces were imaged in the as-fractured condition.

3.3.7 Chemical composition

For Publication II, the chemical composition of the manufactured specimens was measured with optical emission spectrometry using an OES ARL ISpark 8860 for

heavy elements, and the O and N contents were measured with the carrier gas method using a Leco TC-500. The chemical composition of the powder used for Publication III was measured with inductively coupled plasma-optical emission spectrometry (ICP-OES) using a Thermo-Fischer iCAP7400 Duo for heavy elements, with inert gas fusion LECO ONH-836 for gases O, N, and H, and with combustion non-dispersive infrared detection using LECO CS 744 for C and S.

3.3.8 Summary

Each of the methods described above were utilized in one or more of the publications covered in this thesis. **Table 7** provides a summary of the materials testing and characterization methods used in each publication.

Table 7. Summary of analysis methods used in each publication.

No.	Powder analysis	Poro-sity	Material testing	Micro-structure	Melt pool geometry	Process monitoring	Others
I	PSD	OM	None	OM	OM	None	Gas flow speed measurement
II	PSD, SEM, composition	OM	Tensile, impact, fracture surfaces	OM, SEM, EBSD, EDS	None	None	Powder flow, tap and packing density analysis
III	PSD, SEM, composition	xCT	None	None	None	Powder bed imaging	Dimensional analysis
IV	PSD	OM, xCT	None	OM	OM	Melt pool monitoring	Laser beam characterization, spectrometry

4 Results

4.1 Effect of shielding gas flow on porosity and melt pool geometry

Publication I studied the effect of shielding gas flow on quality of parts produced. **Figure 21** summarizes the results of varying the shielding gas flow speed while operating at constant laser parameters, but at different locations of the building platform. **Figure 21** (a–b) first shows the shielding gas flow speed as measured above the building platform at the nine specimen locations for two different gas flow speeds and (c) shows that there is a linear correlation between the gas flow speed setting monitored in the machine (measured at the inlet pipe) and the actual gas flow speed measured above the build area. As seen in **Figure 21** (d), the porosity remains low (<0.07%) at all locations when the gas flow speed is above 2.5 m/s. When the gas flow speed is decreased to 2.0 m/s and below the porosity increases exponentially. The trend is the same regardless of location. Location 1 shows somewhat higher porosities in the 1.0 and 2.0 m/s gas flow condition, and location 4 in the 1.0 m/s condition, compared to the rest. **Figure 21** (e–f) further shows the melt pool dimensions as a function of location on the building platform. For gas flow speeds between 4.0 m/s and 2.5 m/s, the melt pool penetration depth and width remain fairly constant. The penetration decreases dramatically and the weld width increases to some degree when the gas flow speed is reduced below 2.0 m/s. No correlation between the building platform location and the melt pool dimensions can be inferred as the intra-specimen variations are much higher than any differences between the locations.

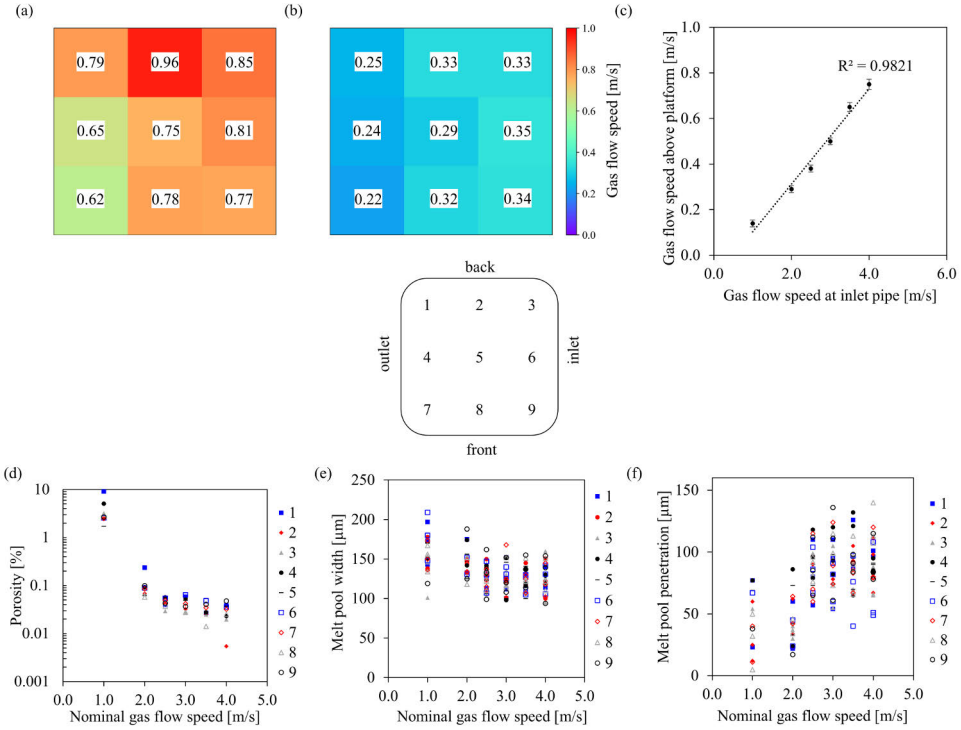

Figure 21. Effect of shielding gas flow speed on porosity and melt pool geometry at nine different locations on the building platform. The gas flow speeds as measured at specific locations with a (a) 4 m/s and (b) 2 m/s nominal gas flow speed setting, and (c) the linear correlation between the set speed and speed measured at the building platform, where R^2 is the coefficient of determination for the goodness of the fit. The corresponding (d) porosity, (e) melt pool width, and (f) melt pool penetration are also given as a function of the set shielding gas flow speed at the nine different locations. Notice the logarithmic scale for porosity in (d). The laser scanning parameters were constant at p = 175 W, v = 750 mm/s, and h = 0.12 mm. Adapted from Publication I.

Figure 22 shows the effect of gas flow speed on (a–b) melt pool geometry and (c) porosity for various laser power and scanning combinations, characterized by the line energy $LE=P/v$. Similarly, as already observed in **Figure 21**, the penetration remains essentially constant for gas flow speeds between 2.5 and 4.0 m/s. Once reduced to 2.0 m/s and below, a sharp decrease in the penetration depth is observed for specimens with line energies >0.2 J/mm. The higher the line energy above this threshold, the greater the decrease in penetration depth. For low line energies (<0.1 J/mm) the shielding gas flow speed has no effect on the penetration depth. Similarly, with high line energy, the melt pool width increases as the gas flow speed decreases. At low line energies, the shielding gas flows speed has no impact on the melt pool width. Examples of melt pool cross-sections as a function of the gas flow speed at high and low line energies are included.

Next, **Figure 22** (c) shows the porosity at different line energies as a function of gas flow speed. The general trend at all line energies is that the porosity increases as the nominal gas flow speed decreases. The trends are, however, different depending on the line energy used. At medium line energy (0.1–0.35 J/mm) there is an exponential increase in porosity after the nominal gas flow speed is decreased to 2.0 m/s and below, similar to **Figure 21** (d). At low (≤0.1 J/mm) line energy, the exponential increase at 2.0 m/s is not clear, rather the porosity has a more continuous, almost linear, increase associated with each subsequent decrease in gas flow. At high line energy (>0.35 J/mm), in contrast, the porosity first decreases when the gas flow speed is reduced to 2.0 m/s, only to increase again once reduced further to 1.0 m/s.

Figure 22 (d) further highlights the impact of the shielding gas flow speed on the melt pool area at different laser powers. Although the relationship between laser power and melt pool size is always linear, the slope changes dramatically depending on the shielding gas flow speed used. The melt pool area decreases by 30–50% when the shielding gas flow speed is decreased from 4 m/s to 2 m/s, depending on the laser power used. With high laser powers the loss of penetration associated with a decreased shielding gas cross-flow is more dramatic.

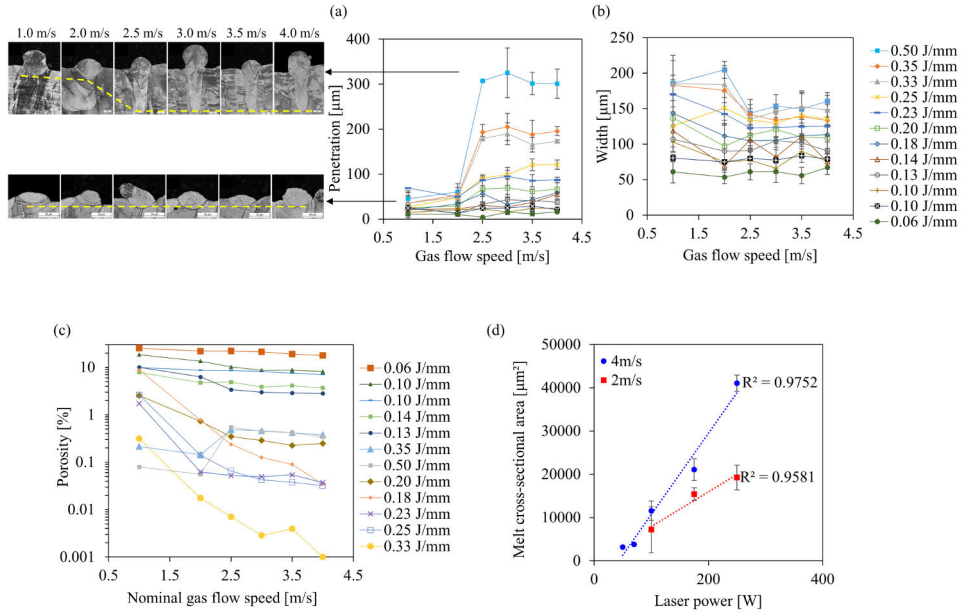

Figure 22. Effect of shielding gas flow speed on (a) melt pool penetration, (b) melt pool width, and (c) porosity (notice the logarithmic scale) at various laser energy densities, and (d) linear fit to melt pool cross-sectional area as a function of laser power at 4 m/s and 2 m/s gas flow speeds, where R^2 is the coefficient of determination for the goodness of the fit. Adapted from Publication I.

4.2 Effect of heat treatments on variability in mechanical properties

Publication II studied the effects of different machine-powder combinations and post-process heat treatments on the quality of parts produced. **Figure 23** summarizes the mechanical properties of parts produced utilizing different machine-powder combinations, and the impact of standardized post-process heat treatments on the properties. In the stress-relieved (SR) condition the maximum differences in the properties between the studied machine-powder combinations were ~7% in ultimate tensile strength (R_m), yield strength (Rp0.2), and elongation after fracture (A). Solution annealing (SA) reduced the absolute values of R_m by 4–7% and $Rp_{0.2}$ by 15–26%, while elongation increased by 14–20% compared to the SR condition. Hot isostatic pressing (HIP) reduced the R_m by 3–8% and the $Rp_{0.2}$ by 43–47%, and it increased elongation by 17–32% compared to the SR condition. It is worth noting that all the tested specimens regardless of condition met and exceeded the minimum requirements defined in ASTM F3184-16 for AM 316L. The intra-specimen variation in tensile properties within each heat treatment condition was small. The standard deviations were from 0.6–7.7 MPa for $Rp_{0.2}$, 0.6–3.0 MPa for R_m, and 0.6–3.2% for elongation, indicated by the error bars in **Figure 23** (a–c).

Figure 23 (d) shows that the porosity for all conditions was generally low, at ≤0.07%. It can be also seen that the HIP condition resulted in clearly lower porosity (0.01%) than the other conditions, as might be expected. The EOS powder in the SLM machine resulted in slightly higher porosity, while the EOS machine resulted in similar porosities regardless of the powder used.

Figure 23 (e) shows that the impact toughness was higher for specimens produced with the EOS machine, regardless of the power and heat treatment used. Even after HIP, the impact toughness was ~10% higher for specimens manufactured with the EOS machine.

In the baseline SR condition, the impact toughness using the EOS machine was 10% higher when using SLM powder, and 25% higher when using EOS powder, compared to the SLM machine. SA and HIP both reduced the absolute impact toughness values compared to the SR condition.

Finally, **Figure 23** (f) summarizes the impact of the studied heat treatments in terms of reducing the variability in mechanical properties, characterized by the coefficient of variation (CV). HIP significantly reduced the variation between the conditions for all properties except tensile elongation. Compared with the baseline SR condition, SA effectively reduced the variation in ultimate tensile strength and porosity, while the variation in yield strength, impact toughness, and elongation increased.

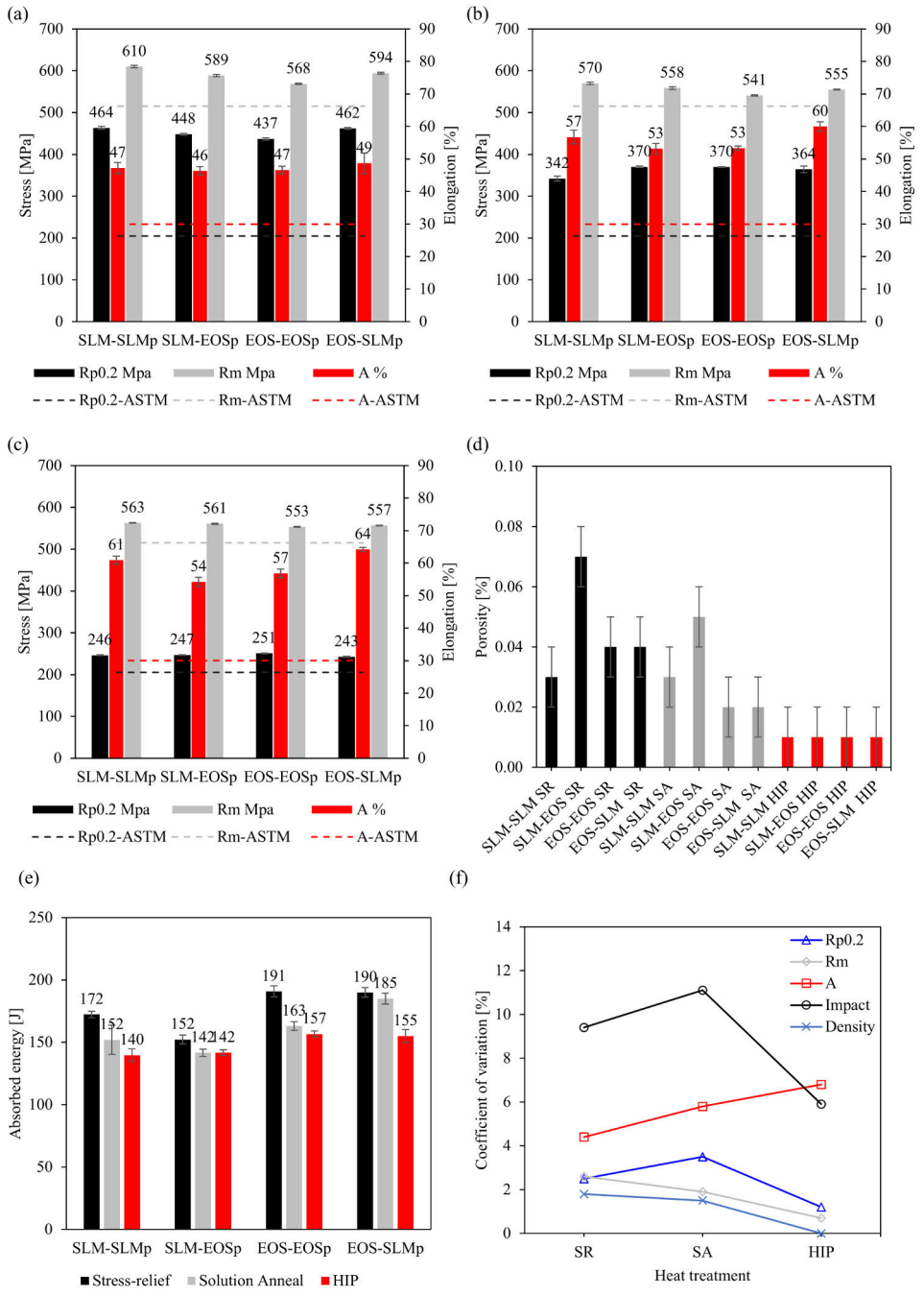

Figure 23. Effect of different machine-powder combinations and post-process heat treatments on (a–c) tensile properties, (d) porosity and (e) impact toughness of PBF-LB processed 316L stainless steel, while (f) shows the impact of the different heat treatments on the coefficient of variation of the properties. Adapted from Publication II.

The microstructures of the different heat-treatment conditions as analyzed with optical microscopy and SEM/BSD are shown in **Figure 24**, while **Figure 25** shows the EBSD images. In the etched OM images, the individual melt pool boundaries from the PBF-LB process are visible in the SR condition, but not anymore in the SA and HIP conditions. In the SR and SA conditions, the grains were mostly columnar along the built direction and highly textured, as seen in the BSD images. A clear difference in the microstructure was observed for the HIP condition, where annealed grains along with annealing twins were observed. For the HIP condition the BSD images also clearly showed that the round inclusions were much larger than in the SA and SR conditions. Furthermore, the inclusion size in the SA condition seemed slightly larger than in the SR condition. From the EBSD analysis, the KAM images indicate the release of residual strain/stress specifically inside the grains after solution annealing. A slightly more equiaxed grain structure can be observed for the SA condition compared with the SR condition, indicating partial recovery after solution annealing. The highly textured and columnar grain structure generated along the build direction in the PBF-LB process remains in the stress-relieved condition and generally also in the solution annealed condition, but disappeared after HIP. The HIP treatment involves re-crystallization and the formation of equiaxed grains of approximately 100 μm in size. However, features of the cellular sub-grain structure remain, as can be seen in the BSD images.

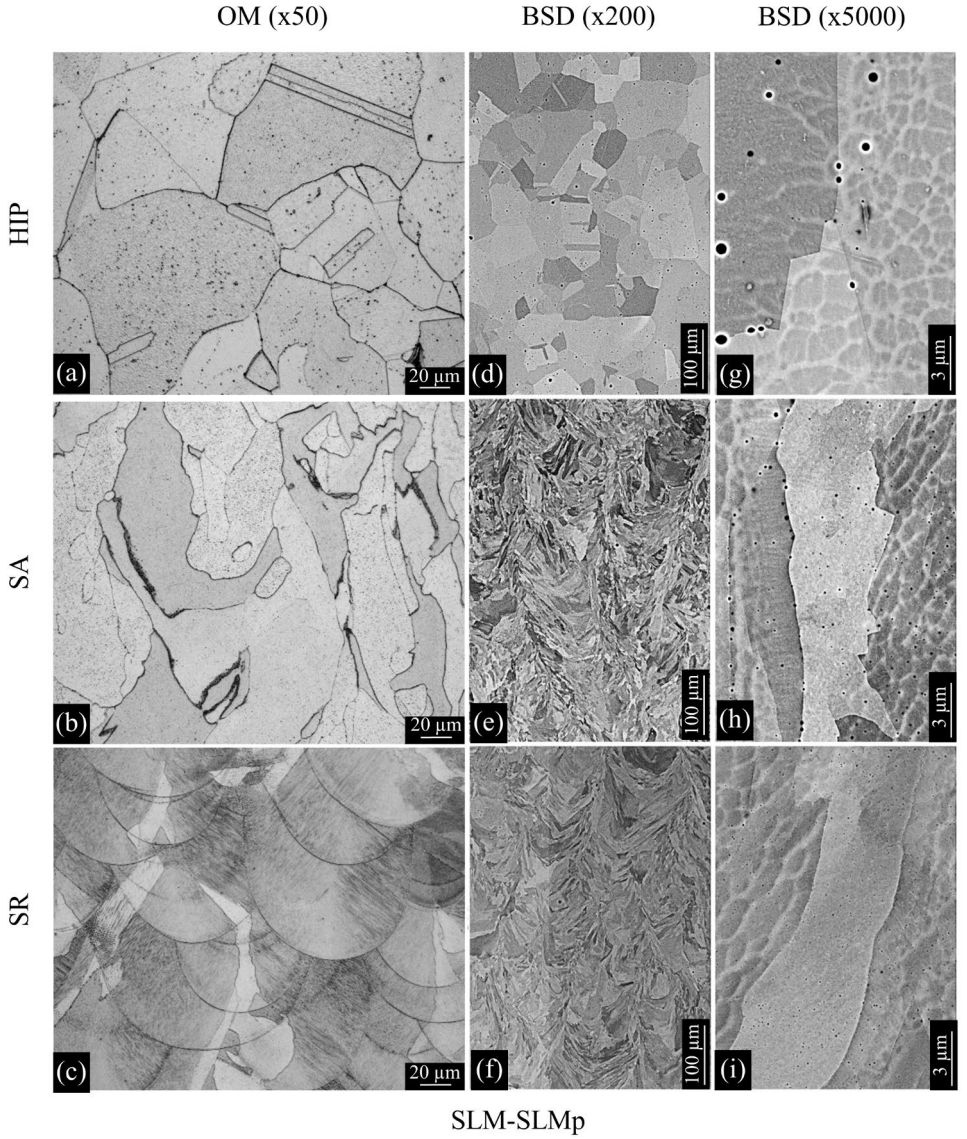

Figure 24. Microstructures of the SLM-SLMp machine-powder combination specimen imaged with (a–c) an optical microscope and (d–i) SEM/BSD at two magnifications for the SR, SA, and HIP heat-treatment conditions. The build direction is from bottom to top in the images. Adapted from Publication II.

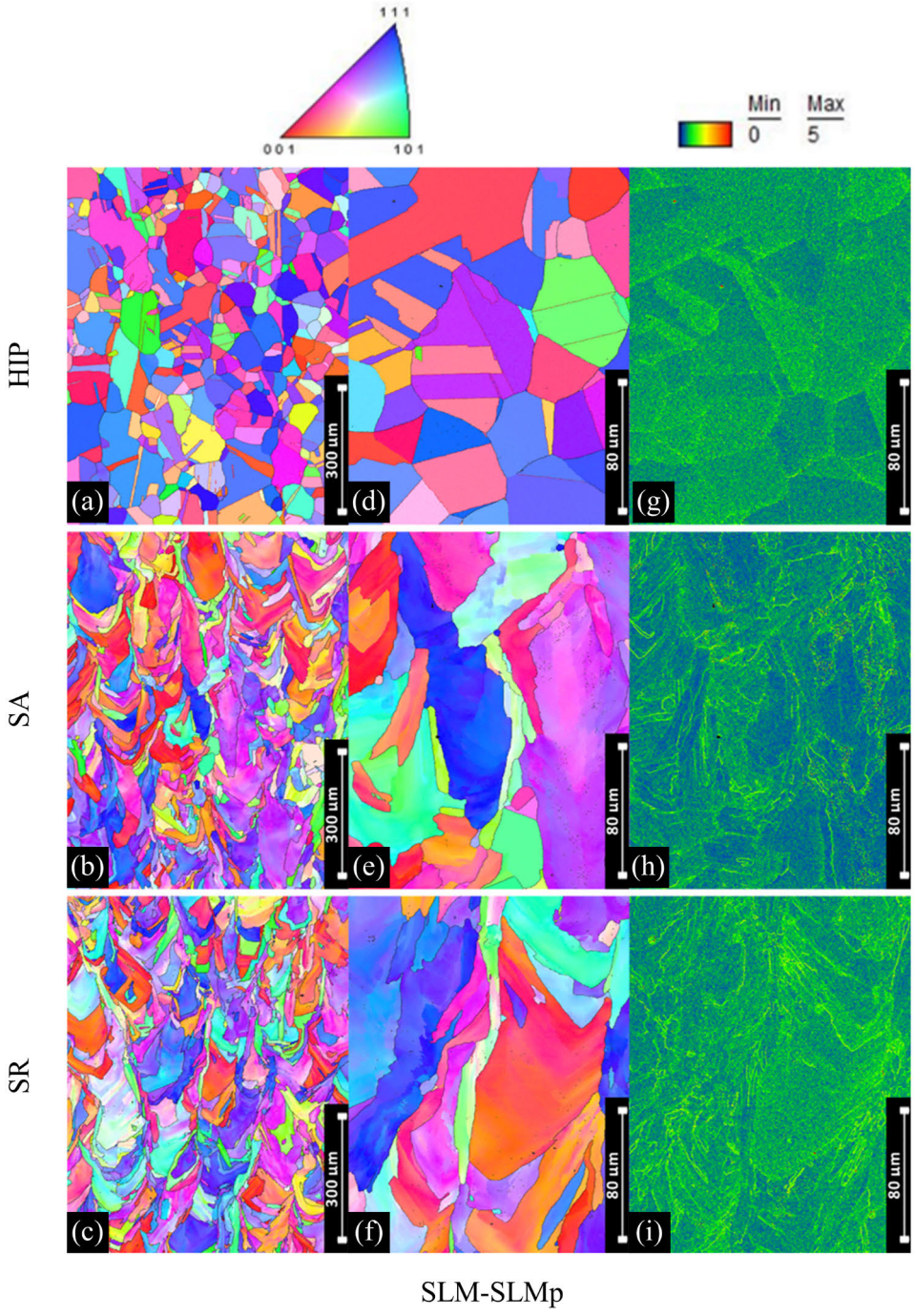

Figure 25. EBSD images displaying (a–f) inverse pole figure (IPF) maps at two magnifications and (g–i) kernel average misorientation (KAM) maps of the SLM-SLMp machine-powder combination specimen for the SR, SA, and HIP heat-treatment conditions. The build direction is from bottom to top in the images. Adapted from Publication II.

Figure 26 shows SEM images of typical impact specimen fracture surfaces. Ductile dimple fracture was the dominant failure mode observed for all studied conditions. However, it was observed that the dimples showed a size difference between the heat treatment conditions with HIP > SA > SR, which indicates coarsening of the sub-grain cellular structure and inclusions, also visible in the BSD images of **Figure 24**.

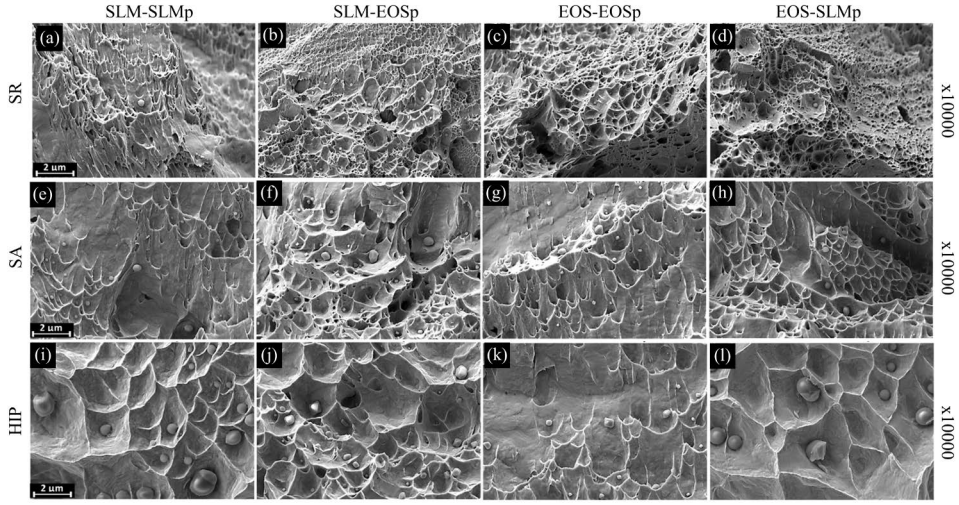

Figure 26. SEM-SE images of typical impact specimen fracture surfaces for all the studied machine-powder combinations in SR, SA, and HIP heat-treatment conditions. Adapted from Publication II.

Higher magnification SEM images (shown in **Figure 27**) revealed inclusions mainly located at the dimples. From the images, the sizes of the inclusions were measured to be around 400–1600 nm for HIP, 300–600 nm for SA, and 50–300 nm for the SR condition. The oxide inclusions were also observed to be larger in specimens produced with the SLM powder (SLMp), regardless of the machine used. The inclusions were mostly round oxides in the specimens produced from the SLM powder, whereas for the EOS powder the inclusions were more angular in shape. Analysis of the composition of the oxide inclusions with EDS confirmed the spherical inclusions to be Si-oxides, while the angular ones were Mo-Mn-Fe-oxides.

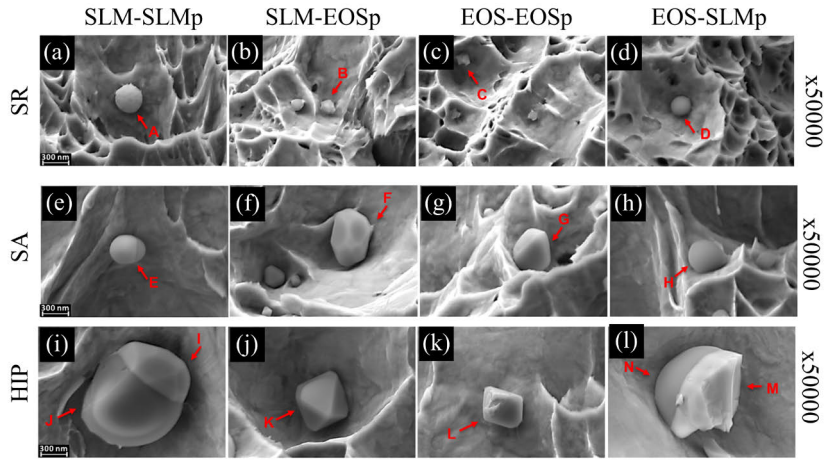

Condition	Specimen	Point	C	O	Al	Si	Cr	Mn	Fe	Ni	Mo
SR	SLM-SLMp	A	1.6	45.0	-	33.1	12.8	3.8	3.1	-	-
	SLM-EOSp	B	2.4	28.6	2.3	21.6	12.9	6.1	21.8	4.0	<1
	EOS-EOSp	C	2.2	37.2	2.1	6.6	25.2	7.5	16.4	1.2	1.6
	EOS-SLMp	D	3.0	42.7	1.0	36.7	8.7	<1	5.9	<1	-
SA	SLM-SLMp	E	1.8	21.6	-	19.6	8.5	11.0	3.5	-	34.0
	SLM-EOSp	F	1.8	1.5	-	-	5.7	24.2	2.6	-	64.0
	EOS-EOSp	G	1.5	2.7	-	-	6.9	19.9	4.2	<1	64.2
	EOS-SLMp	H	1.5	43.2	1.2	43.0	6.0	-	4.3	<1	-
HIP	SLM-SLMp	I	1.1	1.9	-	<1	7.3	18.9	1.0	-	69.0
		J	-	51.6	1.3	45.9	-	-	<1	-	-
	SLM-EOSp	K	2.7	64.5	1.7	-	29.1	1.9	-	-	-
	EOS-EOSp	L	3.1	66.1	-	-	28.7	1.0	1.2	-	-
	EOS-SLMp	M	<1	2.7	-	1.6	5.9	8.9	4.7	<1	74.4
		N	1.9	39.9	2.5	31.2	6.0	2.4	<1	-	15.2

Figure 27. SEM images of the inclusions on the impact specimen fracture surfaces for all studied machine-powder combinations for the SR (a–d), SA (e–h), and HIP (i–l) heat-treatment conditions. EDS analysis of the elemental composition (wt-%) at points (A–N) is included. Adapted from Publication II.

4.3 Effect of re-coater blade type on porosity and processability

Publication III studied the impact of the re-coater blade type used on the quality of parts produced. The processability of selected challenging features was assessed by simply observing whether the features could be successfully manufactured. When building with the soft re-coater blade, all the parts in the build job were manufactured until the end of the build job; however, some features damaged the re-coater blade upon collision. When building with the hard re-coater blade, a collision between the unyielding blade and a feature of a part rising from the powder bed caused an

interruption to the build cycle three times, and the parts that collided had to be discontinued. After this initial assessment, images obtained with the CIS-based process monitoring setup (see Section 3.2.3) were used to further analyze the processability of the features.

Figure 28 (a–f) shows various types of anomalies on the spread powder layer identified in the CIS images. These include spatter deposition on (a) a part surface and (b) re-deposition by the re-coater at other locations, (c) insufficient powder deposition on a part surface, (d) powder bed disturbances caused by a re-coater broken due to collision with part features rising from the powder bed, (e) broken part features due to collision with the re-coater, and (f) disturbances in the powder bed due to contact between the re-coater and part features protruding from the powder bed. **Figure 28** (g–h) shows the quantified metric derived from the images based on the Laplacian focus measure of disturbances in the powder bed caused by collisions between a protruding thin feature and the re-coater blade. Such disturbances in the powder bed were seen frequently with the hard re-coater blade, but were rarer with the soft blade. During the first 200 layers of the build, which correspond to the solid bottoms of the specimens, the proportion of out-of-focus area in the images remains low for both re-coater blades. After the thin walls and overhang features start (layers >200), the proportion of out-of-focus area in the image increases dramatically for the hard blade due to frequent disturbances in the powder bed, while remaining relatively stable for the soft blade. Furthermore, with the hard blade there is high variance between individual layers, which means that collisions between the protruding features and the hard blade occurred only on some layers. Examples of Laplacian focus measure images from selected layers (layers number 50, 212, and 360) of the builds processed with either the hard or soft blade are included.

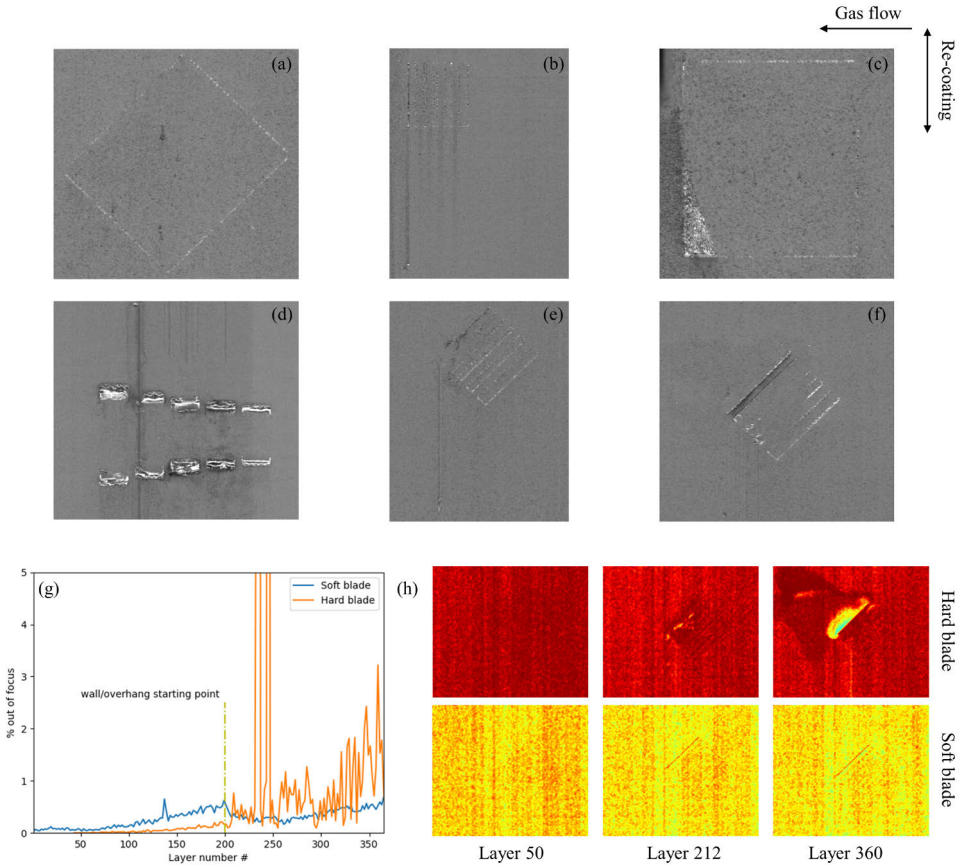

Figure 28. Qualitative examples (a–f) of various types of powder bed anomalies identifiable in the CIS images and (g–h) quantification of powder bed disturbances as proportion of out-of-focus area based on the Laplacian focus measure calculated for the powder bed images as a function of re-coater blade type, for the type of anomaly shown in (f). Adapted from Publication III.

Figure 29 shows the dimensional accuracy of the thin walls produced using the hard and soft blades. With both re-coater blades and for all the part orientations studied, the variation in cross-sectional area along the wall height increases when the wall thickness is decreased. Increasing the wall thickness to >1.0 mm decreases the dimensional error to below 0.4% for the soft blade, after which it does not decrease much even as the wall thickness is further increased. The dimensional inaccuracy increases exponentially when producing walls thinner than 1.0 mm. For a given wall thickness, the part orientation together with the re-coater blade type used have an impact on the magnitude of the dimensional inaccuracy. The lowest accuracy is observed for the combination of 45° part orientation and hard re-coater blade. Comparison of the soft and hard re-coater blades reveals that the soft blade resulted

in higher dimensional accuracy in all the studied part orientations. The same can be said for the surface roughness, as the walls built using the soft blade have smoother surfaces than those built using the hard blade.

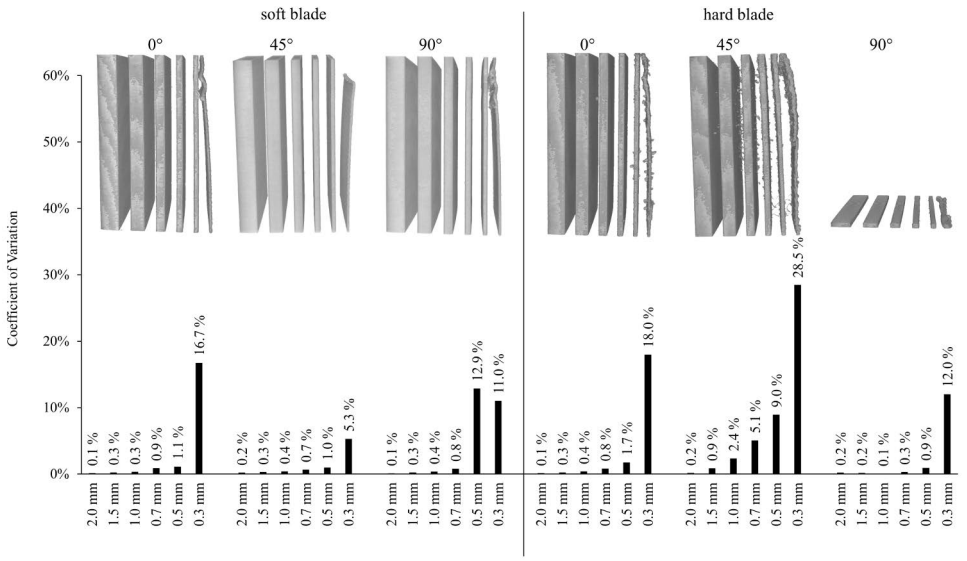

Figure 29. Dimensional accuracy as represented by the coefficient of variation in the cross-sectional area of the thin walls as a function of wall thickness, part orientation, and soft or hard blade. Adapted from Publication III.

Figure 30 shows the dimensional accuracy of the overhangs. Only ~30 layers of the specimen oriented horizontally in relation to the hard re-coater blade could be built before a severe collision between a protruding overhang feature and the hard blade caused the build to stop. For this reason, only the specimens with parallel orientation could be analyzed and compared. With this orientation the hard re-coater blade could process the overhangs for ~ 100 layers, after which a collision resulted in a build interruption. The soft re-coater blade was able to process the features successfully until the end with both orientations, although deterioration of the geometrical accuracy of the features was observed. For quantitative comparison, the distance of each overhang from the beginning to the point where the geometrical accuracy started to deteriorate was measured. The soft blade resulted in longer feature distance and better surface quality for the 45° and 40° overhangs. For the steeper overhangs (≤35°), the hard re-coater blade resulted in longer feature distances before severe geometrical inaccuracy was observed. The bottom surface quality was better for the overhangs produced using the hard blade.

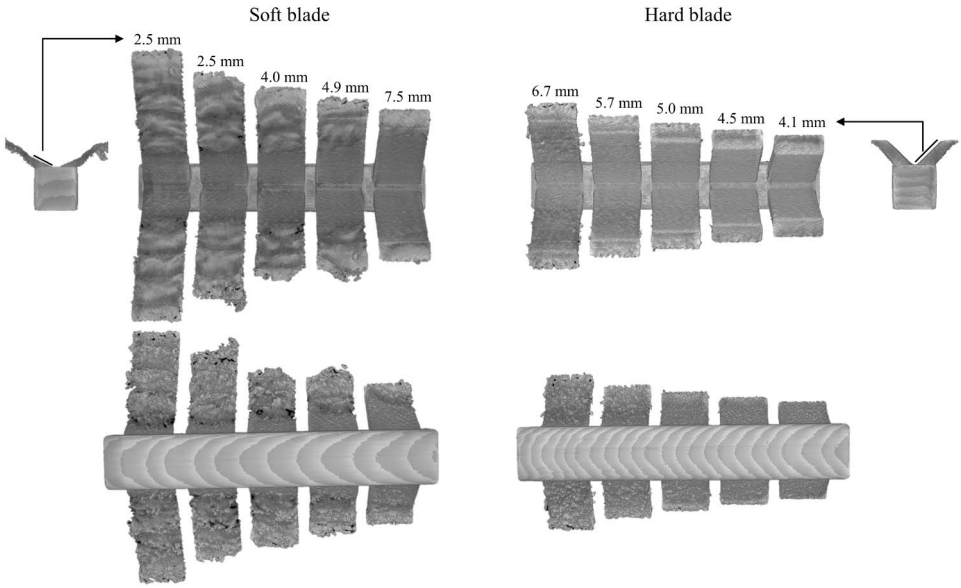

Figure 30. 3D-rendering of the xCT data showing qualitatively the (left) bottom and (right) top surface qualities of the overhang features manufactured with the soft and hard blades. The length of the overhang properly produced is measured from the top surface for quantitative comparison. Adapted from Publication III.

Table 8 lists the measured porosities of the thin walls as a function of part orientation and re-coater blade type. For the overhangs no meaningful total porosity calculation could be made as the features were so deformed that defining part outlines and measuring the part volume accurately was not possible. For the thin walls, it can be seen that the manufactured solid bottoms (bulk material without any intricate features) of the parts are practically fully dense (porosity $\leq 0.001\%$), with barely any voids identified with the xCT scan at 11 µm resolution. This was the case for both re-coater blade types and all studied part orientations. For wall thicknesses of 1.0 mm and above, porosity remains similar to the extremely low levels of the solid bottoms (i.e. bulk material), and no clear differences between blade types can be seen. Reducing the wall thickness below 1.0 mm causes an exponential increase in the porosity. Furthermore, in walls thinner than 1.0 mm, differences in porosity as a function of part orientation and re-coater blade type can be observed. Walls that were oriented parallel (0°) to the re-coating direction and built with the soft re-coater blade resulted in the lowest porosity. At the other extreme, the combination of hard blade and walls oriented horizontally (90°) in relation to the re-coating direction resulted in the highest porosity. The largest difference in porosity between the blades was observed for the wall thickness of 0.3 mm at 90° orientation, where the hard blade resulted in 412% higher porosity than the soft blade. In the case of the 45° and

90° part orientations, the soft re-coater blade resulted in equal or lower porosities for all wall thicknesses. At the 0° orientation, the hard blade resulted in slightly lower porosities in the 0.7 and 0.5 mm walls, while for the 0.3 mm wall thickness the soft blade again resulted in lower porosity.

Table 8. Overall porosity as a function of wall thickness, part orientation, and re-coater blade type.

	Soft blade			Hard blade		
Orientation	0°	45°	90°	0°	45°	90°
Solid bottom	0.001%	0.001%	0.000%	0.001%	0.000%	0.001%
2.0 mm wall	0.000%	0.000%	0.000%	0.000%	0.000%	0.002%
1.5 mm wall	0.001%	0.000%	0.000%	0.001%	0.004%	0.014%
1.0 mm wall	0.001%	0.000%	0.000%	0.001%	0.010%	0.027%
0.7 mm wall	0.004%	0.008%	0.164%	0.002%	0.034%	0.512%
0.5 mm wall	0.125%	0.288%	0.501%	0.054%	0.390%	1.484%
0.3 mm wall	0.434%	1.232%	0.458%	0.927%	1.722%	2.345%

The defect size distributions as a function of feature type, part orientation, and re-coater blade type are shown in **Figure 31**, while **Table 9** shows the mean and maximum defect size for all conditions. As explained in Chapter 0, the types of defect that the voids in the xCT data represent were not identified and classified, but rather treated as a singular group of voids in the material. It is worth noting that with the hard blade the walls of the 90° specimen could be only built for ~15 layers. To allow for comparison, the defect count was then divided by the number of layers built for each thin-walled specimen, characterized as defects per layer. When the wall thickness is decreased below 1.0 mm, the number of defects starts to increase exponentially. Also, the mean size of the defects starts to increase in thin walls below 1.0 mm. Both number and size of defects contribute to the aggregate value of total porosity shown in **Table 8**. Comparison between the re-coater blade types reveals that use of the soft blade results in significantly fewer defects, while the defect sizes are generally slightly smaller with the hard blade. Between the orientations, the 0° condition results in the smallest number and smallest mean size of defects with both blades.

With both blades the number of defects increases as a function of the overhang inclination angle. The steeper the overhang, the more defects were observed. The soft blade resulted in more and larger defects on the overhangs overall. Depending

on the overhang angle, the mean diameters of the defects were 1.3–2.0 times larger with the soft blade.

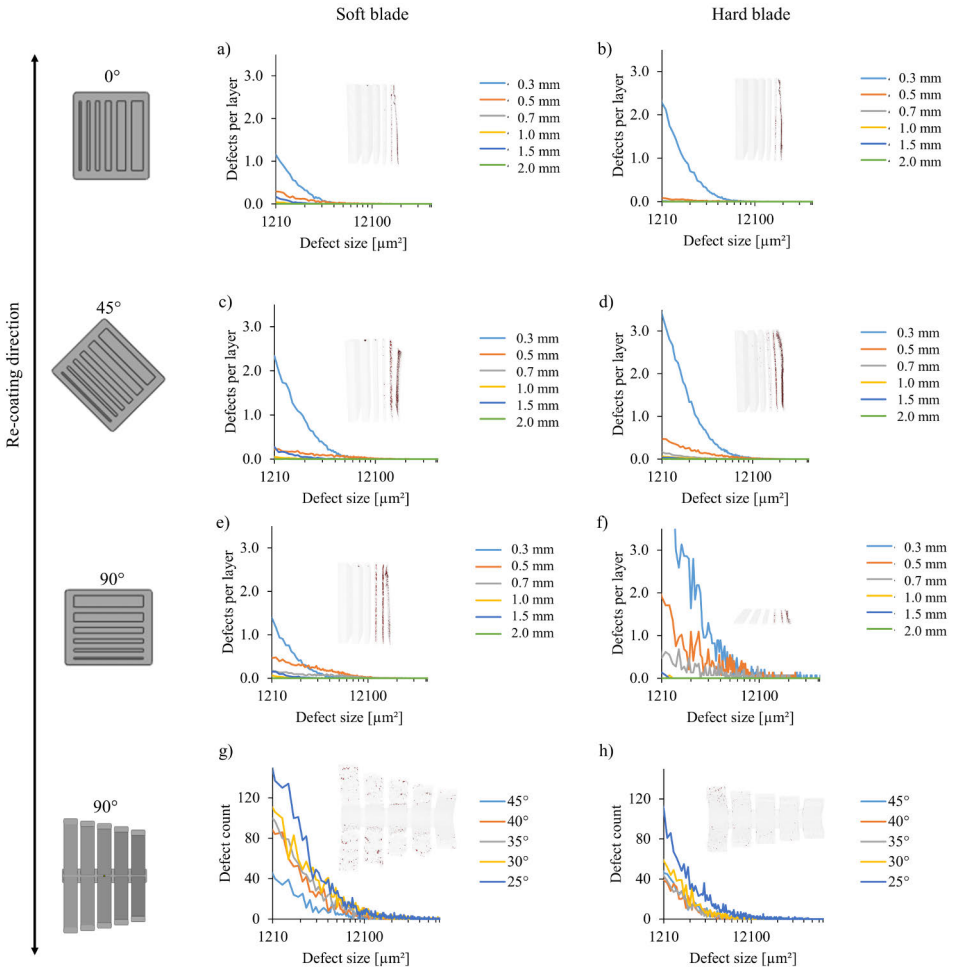

Figure 31. Number of defects having a cross-sectional area larger than 10 pixels (1210 µm^2) as a function of re-coater blade type, part orientation, and (a–f) wall thickness and (g–h) overhang inclination angle. Note that in (a–f) the y-axis is defect count normalized per layer, while in (g–h) it is defect count as such. Note the logarithmic scale on the x-axis in all cases. Transparent re-constructions of the parts and the defects (in red) within are included. Adapted from Publication III.

Table 9. Mean and maximum defect size as a function of feature, orientation, and re-coater blade, assuming a spherical defect shape.

	Soft blade						Hard blade					
Orientation	0°		45°		90°		0°		45°		90°	
Statistic [µm]	Mean	Max	Mean	Max	Mean	Max	Mean	Max	Mean	Max	Mean	Max
2.0 mm wall	15	79	16	46	15	35	16	46	19	48	16	35
1.5 mm wall	21	90	26	206	21	105	16	46	26	124	16	41
1.0 mm wall	19	62	22	90	20	73	15	30	29	179	15	43
0.7 mm wall	23	112	44	161	60	184	18	58	37	247	40	177
0.5 mm wall	43	183	67	234	59	232	42	161	55	260	43	190
0.3 mm wall	31	155	39	174	33	227	33	331	43	370	49	274
45° overhang	-	-	-	-	67	334	-	-	-	-	50	591
40° overhang	-	-	-	-	73	305	-	-	-	-	40	195
35° overhang	-	-	-	-	76	281	-	-	-	-	40	253
30° overhang	-	-	-	-	87	408	-	-	-	-	43	195
25° overhang	-	-	-	-	83	786	-	-	-	-	51	263

4.4 Effect of focal point position on porosity and melt pool geometry

Publication IV studied the impact of focal point position on quality of parts produced. **Figure 32** (a–c) shows the measured melt pool height, penetration, and width as a function of the focal point position. The beam diameter at the work plane associated with each focal point position is included in the figure as the solid line. When the focus position is changed, the melt pool depth inversely follows the hyperbolic trend of the beam diameter. The greatest melt pool depths are observed when the laser beam focal point is on the laser-material interaction plane, or slightly below it. When the focal point position is between +1 and −1 mm compared to the laser-material interaction plane, the variation in average melt pool penetration is 13% and in melt pool total height 8%. These are comparable to the observed intra-specimen variations of 10−23% for penetration depth and 5−9% for total height within the same focal point position range. Positioning the focal point above +1 mm or below −1 mm from the laser-material interaction plane causes a dramatic decrease in penetration and total depth. The decrease is more severe in the positive direction, with the lowest melt pool depth measured in the +5 mm condition. This corresponds to a decrease of 64% in penetration and 50% in depth compared to the +0.5 mm focus position, where the melt pool was deepest. The impact of focal point position

on melt pool width is subtle. On average, the smallest melt pool widths are measured for conditions where the focal point position is at or close to the laser-material interaction plane, and only increase slightly when moving above or below the laser-material interaction plane. However, the intra-specimen scatter in the width measurements is relatively high and hence a statistically significant difference was not found. The melt pool width was narrowest at the +0.5 mm focal point position and widest at +5 mm, with a 15% difference in the averages.

Figure 32 (d–f) shows the photodiode signal intensities obtained with the MPM setup detailed in Chapter 3.2.3 as a function of the focal point position and beam diameter at the work plane. As the focal point position is varied, the signal intensity at the TEP high and TEP low sensors follows a hyperbolic trend in the beam diameter. The TEP low and high signals separately provide a better inverse correlation with the changing beam diameter (caused by the change in the focal point position) than the TEP ratio. The photodiode signals remain fairly constant when the focal point position is between +1 mm and −1 mm. Deviating the focal point position more than this in either direction causes an increase in the TEP high and low signals. When the focal point of the laser beam is positioned below the work plane, the gradient of the increase in the TEP signals is slightly higher compared with when the focal point is positioned above the work plane. This aligns well with the slight asymmetry in the beam diameter between the directions.

In general, the trend observed for all the photodiode signals matches well with the melt pool depth and penetration response. For the TED sensor signal there are two data points that deviate from the trend. At the +0.5 mm focus position, the TED signal is higher than the hyperbolic trend would suggest (the red circle in **Figure 32** (f)). Further analyses (See the Appendix of Publication IV) showed that this anomaly was caused by a change in photodiode intensity close to the middle of the building platform where this specimen was located. Another deviation is seen at the +5 mm focus position, where the TED signal no longer follows the hyperbolic trend. The cause of this could not be identified within the study.

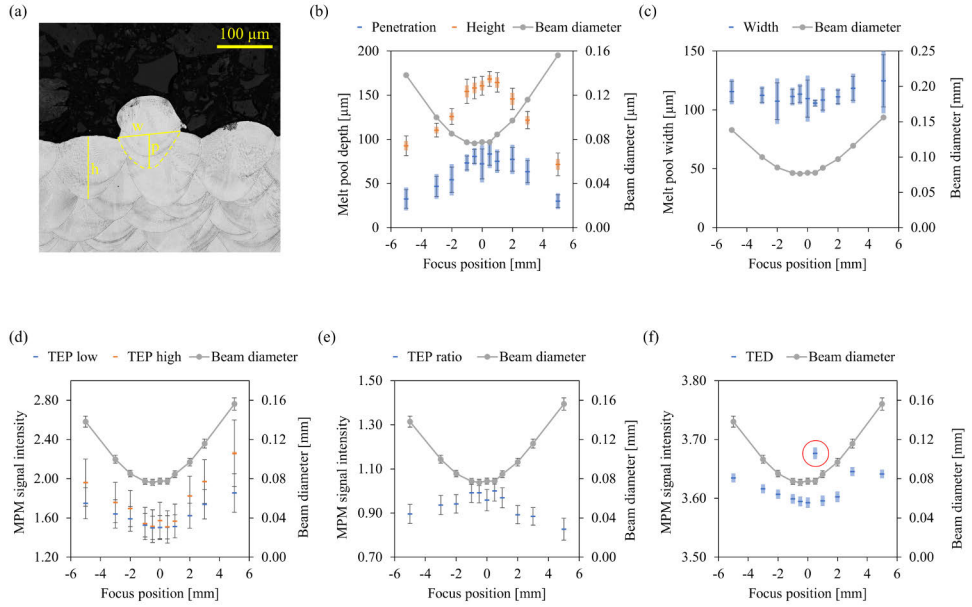

Figure 32. (b−c) Melt pool dimensions (height *h*, width *w*, and penetration *p* measured as shown in (a)) and (d−f) melt pool monitoring (MPM) photodiode signal intensities as a function of focus position and beam diameter at the work plane. In (b−f), the line marks the mean, the transparent blue/orange error bar is the (95% for melt pool dimensions, 99% for MPM signals) confidence interval of the mean, and the whiskers mark the sample standard deviation of the data. For the beam diameters the whiskers mark the error associated with the measuring device. The red circle in (f) marks an anomaly identified in the data. Adapted from Publication IV.

In **Figure 33**, the beam area-normalized melt pool width and penetration as a function of the studied energy density parameters (see Chapter 2.6) are plotted. VED shows no clear correlation with the melt pool dimensional response when the beam diameter (via the focal point position adjustment) is included as a variable. This is understandable, as the metric does not consider beam diameter in the equation at all. For the other energy density parameters *PD*, *ED*, and $\Delta H/h_s$, and the new TED/πa^2 introduced in this thesis, there is a strong positive linear correlation between the melt pool width for the whole range of parameters studied, while for melt pool penetration the strong linear trend starts to break down at the highest energy densities studied, corresponding to a threshold of $\Delta H/h_s$ ~12. The coefficients of determination (R^2) for the linear regression analysis are included in **Table 10**.

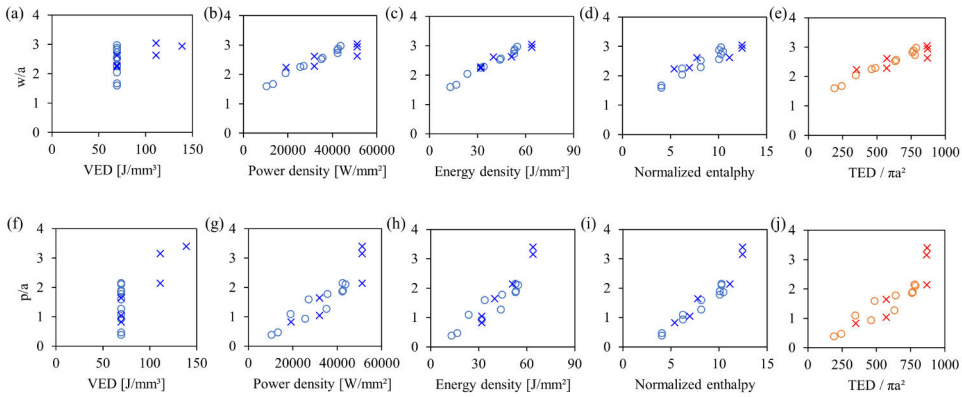

Figure 33. Laser beam radius *a*-normalized melt pool (a−e) width *w* and (f−j) penetration *p* as a function of energy density parameters (blue) introduced in previous studies and (orange) the normalized energy density parameter based on the photodiode melt pool monitoring signal introduced in this thesis. The circles mark specimens where the focal point position is a variable, while crosses mark specimens where the laser power, scanning speed, and hatch distance were the intended variables. Adapted from Publication IV.

Table 10. Coefficients of determination (R^2) for linear regression analysis between the studied energy density parameters and the normalized melt pool width and penetration.

Energy density parameter	**R^2 for linear regression**		
Response	***w/a***	***p/a***	***p/a, while $\Delta H/h_s < 12$***
VED	0.19	0.56	0.11
PD	0.87	0.82	0.86
ED	0.95	0.86	0.87
$\Delta H/h_s$	0.86	0.91	0.95
$TED/\pi a^2$	0.90	0.80	0.87

Porosity as a function of the studied focal point positions is shown in **Figure 34**. For all the studied conditions, the cylinders (i.e. bulk material) were practically fully dense, with porosities of ≤0.004%. In the thin walls the porosity increased ten-fold for all the studied conditions. The differences in porosity, caused by a change in the focal point position, become more evident in the thin-walled geometries. Between the −5 mm and −0.5 mm focal point positions the porosity remains fairly constant. Between 0 mm and +2 mm the porosity decreases slightly. In the +3 mm focal point position the porosity increases slightly, and in the +5 mm condition a significant increase can already be observed. **Figure 34** (a, b) shows the defect sizes for the studied focus positions. As explained in Chapter 0, the types of defect that the voids

in the xCT data represent were not identified and classified, but rather treated as a singular group of voids in the material. The focal point position does not have a major impact on defect size. The defects are relatively small (mean diameter 15−21 µm) in all conditions. It can be seen, however, that the number of larger defects (>60 µm mean diameter) is higher in the thin walls. The largest defect in the thin walls was ~110 µm in diameter, in the specimen produced with the +5 mm focal point position. Finally, **Figure 34** (d) shows the number of defects as a function of focal point position. The trend aligns well with the trend in total porosity, which means that an increase in number of defects rather than an increase in defect size is responsible for the measured differences in total porosity between the studied focal point positions.

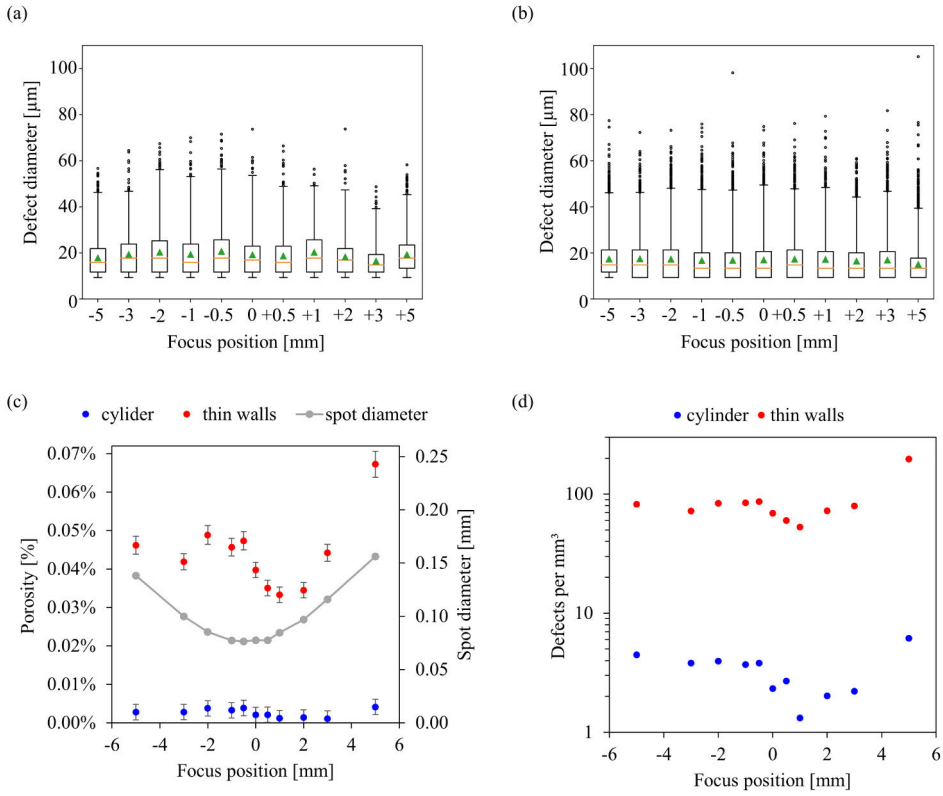

Figure 34. Defect size distributions for (a) cylinder and (b) thin-walled sections of the specimens as a function of the focal point position. Total porosity as a function of focal point position is shown in (c), along with the associated change in beam diameter. Number of defects per unit volume of material as a function of focal point position is shown in (d). In (a−b), the lines mark the median, the triangles the mean, the boxes the 25th and 75th and the whiskers the 1st and 99th percentiles of the data, while outliers are marked with dots. In (c) the whiskers mark the error associated with the porosity measurement method. Notice the logarithmic scale of the y-axis in (d). Adapted from Publication IV.

From the xCT data it was observed that in all the specimens the majority of the defects were concentrated at part edges. This is shown in **Figure 35** for the specimens produced at the different focal point positions. Although in all cases most defects are concentrated at the edges, it can be seen that for the +5 mm focal point position the number of defects in the core also increased significantly.

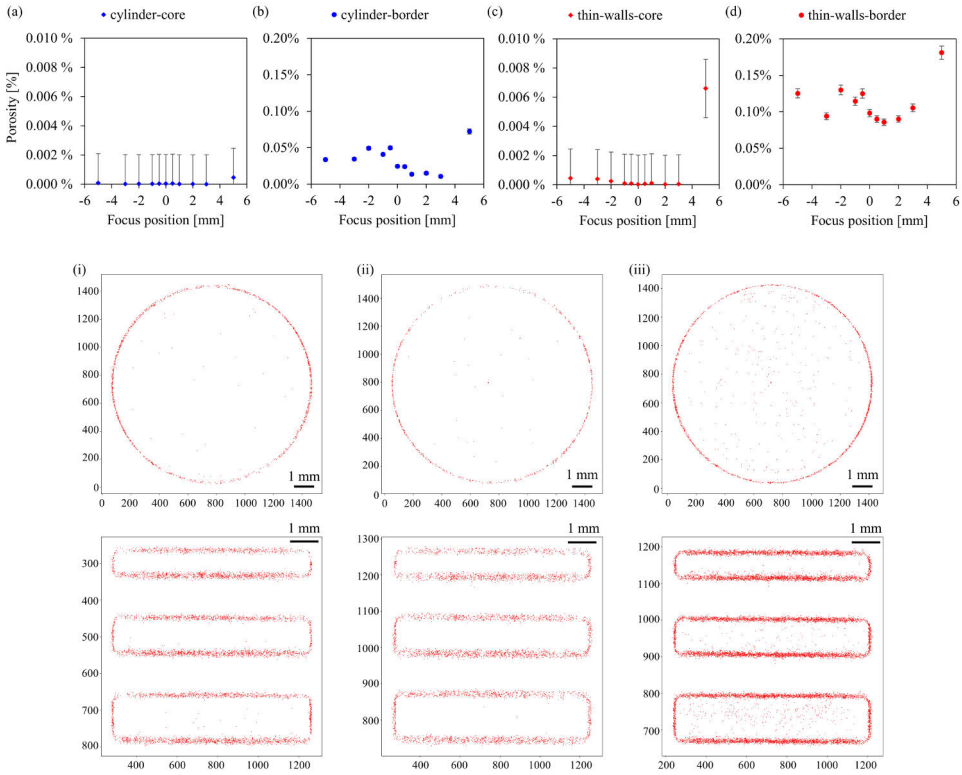

Figure 35. Total porosity for (a, c) the core and (b, d) border regions in the (a−b) cylinder and (c−d) thin-walled sections of the specimens, as a function of focal point position. Defects in an area within 0.15 mm from the part edge were classified as border defects, the rest as core. Defect locations projected from the build direction on the xy-plane for the cylinder and thin-walled sections are shown as examples for specimens produced with (i) −5 mm, (ii) 0 mm, and (iii) +5 mm focal point positions. Adapted from Publication IV.

Furthermore, when analyzing the single tracks from the xCT, defects formed at the ends of the laser vectors were identified. Such defects were frequently seen in the laser vector endings, never at the beginnings. This is shown in **Figure 36** (a−b). These defects were more frequent in specimens produced with high laser powers above 200 W. Three types of behavior in the single tracks where such defects were present were observed in transverse cross-sections of the vector endings in the xCT data. Firstly, it was observed that the keyhole, caused by the vapor-induced pressure

during the laser melting, had remained open after solidification at the laser vector end. Examples of this are shown in **Figure 36** (c, f, g). Secondly, it was observed that the keyhole had closed from the middle in some single-track endings, but the bottom had remained open during solidification, leaving behind a void underneath the surface. Examples of this can be seen in **Figure 36** (d, e, h). And thirdly, in some single tracks the keyhole had closed and only a minor dent, if anything, was visible at the laser vector end. Finally, **Figure 36** (i–l) shows examples of such defects located at the edges of the macroscopic part, where the laser vectors end.

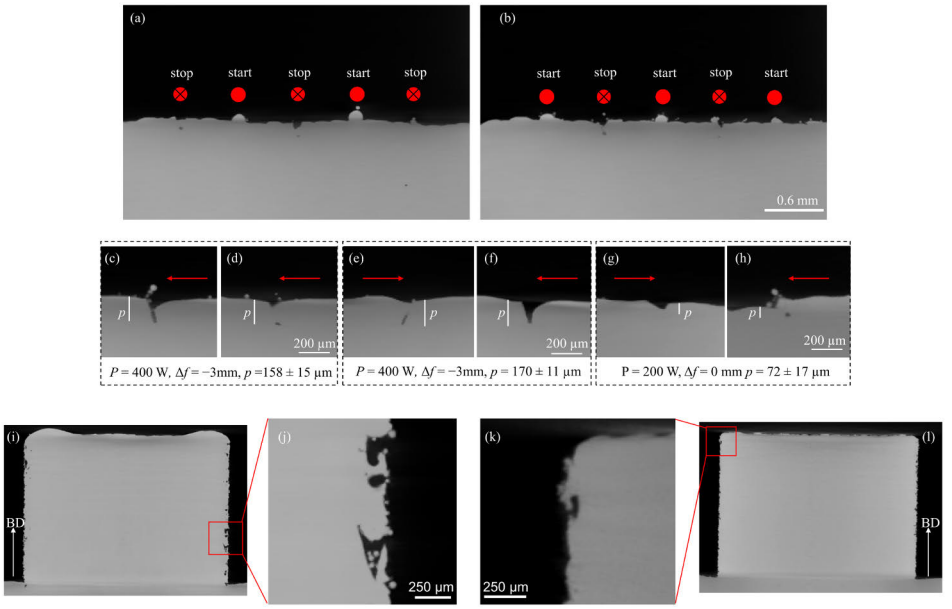

Figure 36. Perpendicular (a–b) views of the xCT data in relation to the single-track cross-sections showing openly solidified keyholes and associated keyhole pores at the ends (never at the beginnings) of the laser vectors. Transverse (c–h) views of the xCT data in relation to the single-track cross-sections showing examples of (c, f, g) keyholes solidified open at the surface and (d, e, h) keyholes where only the bottom has solidified open. Examples of border defects at (i, j) the 0 mm focal point position with 200 W laser power and (k, l) the −3 mm focal point position with 400 W laser power. BD indicates build direction, the red arrows the scanning direction, and the white line shows the penetration *p* measured for the associated single tracks from the etched cross-sections. Adapted from Publication IV.

5 Discussion

5.1 Machine architecture-defined process parameters as sources of variability

The *machine architecture-defined process parameters* studied in this thesis were the shielding gas flow speed, re-coater blade type, and focal point position. This chapter discusses their contribution to the observed variation in part properties in the PBF-LB process, and how these parameters should be treated with regard to quality control.

Gas flow

The shielding gas flow is a crucial part of the PBF-LB process, and the flow speed has a significant effect on the melt pool geometry and porosity. The shielding gas flow settings used should therefore always be reported in the Methods section of PBF-LB studies as standard, along with laser power and scanning speed. The influence of the shielding gas flow speed on the melt pool geometry depends on the values of the laser parameters used. When operating at high (>0.35 J/mm) and medium (0.1–0.35 J/mm) line energy, corresponding to keyhole and transition mode melting, the shielding gas flow speed plays a crucial role in removing the vapor plume from the laser beam path. In these conditions, when the shielding gas flow speed is reduced below a certain threshold there is a drastic loss of penetration and an increase in weld width and instability due to insufficient removal of the vapor plume. The plume attenuates and scatters the laser beam, effectively reducing the energy density at the work plane, which causes loss of penetration if not adequately removed. This loss of penetration is severe enough to cause excessive lack of fusion, which results in an exponential increase in porosity at part level. Increasing the shielding gas flow speed further above the threshold does not result in additional significant changes in the melt pool geometry; however, the porosity continues to decrease, although at a smaller magnitude than that associated with the loss of penetration. This smaller impact on porosity is most likely associated with the continued improvement in the removal of the spatter and denudated powder particles from the build area, which are known to also cause stochastic lack-of-fusion defects

[84]. This could also explain the somewhat higher porosities observed in low gas flow conditions at locations 1 and 4 on the build area in **Figure 21** on the build area, which are located down-stream in relation to the cross-flow of shielding gas and the other parts being scanned, where most such spatter and denudated particles will land [84].

When operating at low energy densities (i.e. in the conduction mode melting regime) the shielding gas flow speed has no impact on the melt pool width and penetration. In conduction mode, the temperature in the melt pool is below the boiling point, meaning there is no vaporization or keyhole formation that leads to deep penetration in high energy density conditions. Therefore, there is no vapor plume to be removed by the shielding gas flow, no keyhole or penetration to be lost, and hence no systematic lack of fusion results. However, porosity still increased slightly in conduction mode melting when the gas flow speed was reduced. This could also be associated with the decreased removal of spatters and denudated powder (i.e. powder particles entrained to the gas flow by the pressure of the vapor plume from the vicinity of the melt pool) that cause stochastic lack of fusion, as explained above.

Finally, it was observed that for the highest energy densities explored, the porosity decreased when the shielding gas flow speed was reduced below the threshold where loss of penetration occurs. In such high energy density conditions the keyhole is too deep and unstable and keyhole porosity forms [120] in high gas flow conditions. When the gas flow speed is insufficient to remove the plume, the keyhole and associated deep penetration is lost. This also eliminates the keyhole porosity, however if the energy density is high enough, the melt pool remains deep enough to avoid excessive lack of fusion. Only when the gas flow was reduced even further did the loss of penetration, even in these conditions, became severe enough to start causing lack of fusion.

From a quality control perspective, control of the shielding gas flow speed and homogeneity over the build area is absolutely necessary to reduce variability in part properties. The shielding gas flow is 1) an essential parameter, 2) prone to variations within and between machines, and 3) hard to set constantly and describe quantitatively. Although the build area of the SLM 125 HL machine used in this study is rather small at 125x125 mm, some location-dependent variation in the gas flow speed above the build area was already seen. In more recent studies, it has been shown that for machines with larger build areas, the variation in flow conditions at different locations of the build area are much more severe, and result in significant melt pool geometry [121] and porosity [122] variations within the build area at constant gas flow speed settings. In recent studies the inhomogeneous shielding gas flow conditions have been identified as the main contributor to the variability in the properties of the PBF-LB parts produced [59][60][123].

In terms of process control, there seems to be a threshold above which the shielding gas flow speed is sufficient to avoid systematic lack of fusion; however, further increasing the gas flow speed is seen as beneficial in also reducing stochastic lack of fusion, as long as the flow above the build area remains homogenous and no recirculation zones are generated. However, this is highly dependent on the hardware, that is, the design of the flow paths in the machine. In addition to controlling the shielding gas flow speed, the design of the flow paths in the machine must be such that they produce a homogenous and sufficient crossflow of shielding gas at all locations of the build area without re-circulation zones. It is recommended that the shielding gas flow speed be measured at various locations of the build volume to verify this. At a minimum, measurements should be taken in a grid above the build plate using, for example, a hot wire anemometer, as was done for Publication I and later also recommended in the ISO/ASTM 52941 standard for acceptance tests of PBF-LB machines for aerospace applications [124].

Specifying the shielding gas flow speed as a grid over the build plate to the AMPS is a good starting point; however, this may be an insufficient description as it does not take into account the possible presence of re-circulation zones in the gas flow. Another option would be to specify the type of machine hardware used in conjunction with the shielding gas flow rate, as recommended by SAE International in aerospace material specification AMS7003 [43]. This, however, would mean that control of the shielding gas flow conditions necessitates use of a fixed machine model. However, this approach does not help in reducing inter-machine variation, as it does not allow the use of different machine models for part production. This is a highly conservative and inflexible approach that does not allow for distributed manufacturing; however, if the shielding gas flow configurations between different PBF-LB machines are not standardized, it may be the only option to ensure consistency in the shielding gas flow conditions.

Re-coater blade type

When processing bulk material, that is, parts without any intricate features, the hard and soft re-coater blades performed equally well. The porosity remained extremely low ($\leq 0.001\%$), no issues were detected in the processability of the parts, and the powder bed conditions remained stable. However, significant differences in porosity and processability arose when building thin walls (<1.0 mm in thickness) and overhanging features (<45° inclination). Furthermore, the orientation of these features in relation to the re-coating direction had a significant impact. This highlights the need to assess the impact of certain PBF-LB process parameters, such as the re-coater blade type in this case, on the properties of parts with intricate features typical in real-world applications. Conclusions based solely on studies using

primitive cubes or cylinders for which porosity or other relevant properties are investigated may be misleading, or at least limited in their applicability to only such primitive shapes. Based on such studies one may conclude that the re-coater blade type is a non-essential parameter; however, as shown in this study, it most certainly is an essential parameter when features such as thin walls or overhangs are present in the part.

When processing thin walls, the soft blade resulted in less porosity, higher dimensional accuracy, and a better surface finish than the hard blade. When the thin walls were oriented perpendicular to the re-coating direction, the hard blade resulted in such a forceful collision with the part being built that the build job could not be finished, while the soft blade was able to finish even in this orientation. In terms of build orientation, the most beneficial setup was to place the thin walls parallel to the re-coating direction. The use of a soft blade is therefore recommended for thin walls. Contact between the unyielding hard blade and the protruding thin features led to severe disturbances in the surrounding powder bed, causing variations in effective layer thickness at these locations, which manifests as increased porosity due to uneven melting conditions.

With the overhangs, there was a compromise between the processability, dimensional accuracy, and porosity of the features depending on which re-coater blade was used. With the steepest overhangs, the unyielding hard re-coater blade is prone to collisions severe enough to stop the build altogether, whereas the soft blade was able to finish under all the studied conditions. However, contact with a feature rising from the powder bed results in damage to the yielding soft blade, which leads to uneven powder spreading and effective powder layer thickness, which may cause defects. Furthermore, the dimensional accuracy and surface finish of overhangs produced with the soft blade was poorer than with the hard blade. Although the overhangs could be built for a longer distance with the soft blade, the porosity was higher compared to when using the hard blade. Therefore, it could be said that the hard blade resulted in better quality overhangs if it was able to process them at all. The risk of fatal build interruption with the hard blade is significantly higher, while the soft blade may finish the feature, but with reduced quality.

From a process control perspective, controlling the re-coater blade type and specifying it to the AMPS (material and shape) is relatively easy. Despite this ease, the re-coater blade type used is regularly omitted in Methods sections of PBF-LB studies and reports dealing with the properties of PBF-LB processed materials. It is recommended that at a minimum the material and blade tip geometry of the re-coater blade used be reported (along with the associated re-coating parameters). From a control perspective, much more challenging is the fact that if the part contains intricate features such as thin walls of <1.0 mm in thickness, the orientation of these features in relation to the re-coating direction was shown to have a significant impact

on the porosity, dimensional accuracy, and surface finish obtained. This indicates that to obtain constant properties in such features, the part orientation would need to be fixed. This may be practically impossible without severely limiting freedom of design, as depending on the design of the part, it may contain such features in multiple orientations and hence regardless of how it is oriented on the building platform multiple orientations in relation to the re-coating direction will be present. It may therefore be necessary to accept higher variation in part properties in thin walls compared to bulk material if the design freedom of AM is to be preserved.

Focal point position

The focal point position in relation to the work plane was shown to have a significant impact on melt pool penetration when deviated by more than ±1 mm (while using a laser beam with a ~3 mm Rayleigh length). Within this range, the change in the diameter is small in a Gaussian beam (see **Figure 7**), however it makes sense to relate the distance to the Rayleigh length of the beam in question. For the laser beam used in this study, a 1 mm deviation from the focal point along the beam propagation axis is ~30% of the Rayleigh length. Variations smaller than ±1 mm in the focal point position resulted in a <13% variation in the melt pool penetration, which is comparable with the intra-specimen variation (10−23%). This is the normal level of variation one can expect in the penetration of the individual melt pools that constitute the part. The effect of varying the focus position within the studied range (±5 mm) on melt pool width was more subtle and statistically not significant.

Between −5 mm and −0.5 mm (i.e. above the work plane), the porosity remained fairly stable. Slightly below the work plane, between 0 mm and +2 mm, the porosity even decreased slightly, and then started to increase at +3 mm. A significant increase in porosity compared to the nominal was only seen once the focal point position was deviated to +5 mm. In this condition, the penetration was already reduced by more than 50%, which was enough to start causing stochastic, although not yet systematic, lack-of-fusion defect formation. This is the case when operating at laser parameters that are firmly in the middle of the optimal processing zone in terms of laser power and scanning speed (see **Figure 5**). It can be expected that with a non-optimal P/v combination, the loss of penetration that starts after shifting the focal point position by more than $\pm 0.3 z_R$ may result in lack of fusion even at smaller focus shifts than the +5 mm used in this study.

Although not the main objective of the focal point position study, upon analysis of the xCT data a defect formation mechanism at the ends of the laser vectors due to openly or semi-openly solidified keyholes was identified. This was found to be the main contributor to the approximately one order of magnitude higher porosity at the part edges compared to the core in all of the specimens, as the vector endings were

always located at part edges. In this particular experiment (Publication IV), separate border vectors were not used, and the part scanning consisted of only the core vectors. In the other experiments discussed in this thesis (Publications I−III) border and contour vectors were included in the scanning pattern, as described in Chapter 0. A similar increase in border porosity was therefore not seen in those experiments. The application of additional border and contour vectors that melt around the part edges could be beneficial in eliminating such defects which form at the core vector endings. This also highlights the fact that any kind of difference in the scanning strategy, not only in the core scanning parameters shown in **Figure 4**, may contribute towards increased porosity formation in actual parts. Such differences in scanning strategies between machines are also potential contributors towards the observed variations in part properties and should be investigated in more detail. While scanning strategy was defined in this thesis as a parameter that is programmatically controllable by the operator, some aspects of it, such as the Sky Writing technique used in this thesis, may have limited control opportunities depending on the galvanometer scanner hardware used in the particular PBF-LB machine.

As the focal point position has a significant impact on the melt pool geometry and eventually on porosity formation and hence part quality, it is an essential parameter in the PBF-LB process. In terms of process control, the focal point position parameter is easy to nominally set to a given position and even control programmatically in PBF-LB machines with a dynamic focusing optic. Despite this ease, the focal point position in relation to the work plane is rarely reported in the Methods sections of PBF-LB studies. It is recommended that this parameter be included routinely, as is the case with laser power and scanning speed, when listing the main processing parameters used in any given study. As the laser beam is the most fundamental tool of the PBF-LB process, at a minimum the characteristics of a focused Gaussian beam described in Chapter 0 (wavelength, beam waist diameter, Rayleigh length, beam quality) which are required to describe this tool adequately should be included in AMPS.

However, controlling the stability of the focal point position is slightly more challenging due to thermal lensing [88]. Nevertheless, there is some tolerance within which, based on this study, the focal point position can vary without significantly impacting the melt pool geometry. A practical tolerance limit of 30% of the Rayleigh length from the nominal laser-material interaction plane in either direction is therefore recommended. Recently, Berez et al. [125] showed that the variation in the focal point position along the build area in a commercial PBF-LB machine (an EOS M280 in their case) can be as much as +1.6 mm to −1.7 mm due to the non-optimal flat view correction applied by the F-theta lens used. The stability of the focal point position is therefore a real issue which must be controlled to maintain stable processing conditions and part quality within and between machines.

When studying the effectiveness of the various proposed energy density models (see Chapter 2.6) in terms of predicting the melt pool geometry response, it was clear that *VED* is insufficient to capture the trends when focal point position and the associated change of beam diameter at the work plane are taken into consideration. On the other hand, the metrics *PD*, *ED*, and $\Delta H/h_s$, which include a term for the beam area, showed strong linear correlation with beam size-normalized melt pool width and penetration. In the case of penetration, the trend started to break down at the highest energy densities studied ($\Delta H/h_s \sim 12$). This aligns well with the transition in the linear trend identified at $\Delta H/h_s > 10$ by Hann et al. [93]. Here the melting mode develops from transition mode to fully developed keyhole mode, which causes a sharp increase in absorptivity that leads to the sharp increase in penetration. In this thesis, a new energy density parameter called the normalized thermal energy density (TED^*) was introduced, which showed with similarly strong confidence ($R^2 = 0.8–0.9$) a linear correlation between beam size-normalized melt pool penetration and width. Although the normalized enthalpy showed a slightly better linear fit ($R^2 = 0.86–0.95$), TED^* is fundamentally different as it has no predictive power but instead is introduced and intended as a quality control metric; a means of continuously *monitoring* possible *variations* in the melt pool during the PBF-LB process.

5.2 Reducing variability with heat treatments

The variation in tensile properties in the stress-relieved condition between the machine-powder combinations studied was relatively small, the CoV being 2.6% for ultimate tensile strength, 2.5% for yield strength, and 4.4% for tensile elongation. For impact toughness, the CoV was higher at 9.4%. As recently shown in other studies on fatigue life [60], the variation may be exponentially higher. This highlights the importance of testing dynamic loading conditions and establishing the variation in properties in addition to the quasi-static tensile test, especially if the application field involves such loading conditions.

The solution annealing treatment investigated had no clear impact in terms of reducing the variation in the properties, while the HIP treatment used significantly reduced the variation in all properties studied except tensile elongation. This is partly due to effective re-crystallization (and hence homogenization) of the microstructure, but more importantly, to a reduction in porosity, neither of which are accomplished with the solution annealing cycle studied. This once again highlighted the important role of porosity in terms of the properties of PBF-LB processed material. The increased variation in elongation with solution annealing and also with HIP treatment is most probably due to the observed growth in inclusion size associated with the high temperature heat treatments. The increased variation in elongation after heat-

treating PBF-LB processed 316L stainless steel was also associated with oxide inclusions in the study by Montero-Sistiaga et al. [126].

The results indicate that post-processing the PBF-LB 316L material with HIP treatment is effective in reducing variation in some of the studied properties. However, it must be emphasized that the reduction in variation is accompanied by a reduction in absolute properties, specifically yield strength. In the stress-relieved condition, the sub-micron-sized cellular dislocation network [26] and other unique hierarchically heterogeneous features in the PBF-LB microstructure [25] remain and result in an excellent combination of strength and ductility. The reduction in yield strength after HIP was 43−47% compared to the SR condition, while elongation improved by 17−32%. It is therefore reasonable to ask whether the associated large decrease in yield strength is justified when aiming to reduce variation in properties with post-process heat treatments such as HIP, especially as the variation in elongation even increased.

As it seems that elimination of porosity is key to reducing variation in the mechanical properties of PBF-LB processed material, attempts to reduce this variation should focus on means of reducing porosity. Arguably, HIP can achieve this, but it comes with an associated loss of the unique, high-strength microstructure that is formed during solidification in PBF-LB. The other drawback associated with HIP was the observed growth in the size of the oxide inclusions, which are detrimental to the impact toughness of the material.

The large number of oxide inclusions in PBF-LB processed 316L is the cause of reduced impact toughness compared to wrought material [127]. The main source of oxygen in the PBF-LB process is oxygen already present in the powder after gas atomization [127][128]. Therefore, from a control perspective, to control the amount of oxide inclusions in the PBF-LB processed material requires control of the oxygen and oxide-forming elements (such as Si, Mn) during powder production. The most impactful means of control that the PBF-LB practitioners have in this regard is the selection of high purity, high quality powder. The oxygen pick-up associated with powder storage, handling, or from the PBF-LB build chamber have a smaller impact [128].

5.3 Detecting variability with process monitoring

To control the outputs from a manufacturing process is to control the input parameters. However, the controllable input parameters in a manufacturing machine may be intermediate and only act indirectly on the unit processes that need to be controlled. The fundamental unit processes in the PBF-LB process are the spread powder layer and the melt pool. The machine operator cannot programmatically set the desired powder layer homogeneity or the desired melt pool geometry and

temperature. Instead, the operator is limited to adjusting the re-coating parameters and the laser beam scanning parameters respectively. More direct measurement of the fundamental unit processes can be achieved with in-situ process monitoring. In this thesis, powder bed imaging with a contact image sensor and melt pool monitoring using co-axial photodiodes were investigated.

The TED^* metric introduced in this thesis, based on the thermal energy density emitted from the melt pool and captured by the photodiode, showed strong linear correlation with the resulting melt pool penetration and width for a range of input laser parameter conditions while $\Delta H/hs < 12$. In addition, it was shown that all the photodiode signals, especially the photodiodes with narrow band filters in front of them in the MPM system used, correlated well with the hyperbolic response to a change in the beam diameter at the work plane caused by a change in the focal point position. It therefore provides a potential means to continuously monitor unwanted focal drift in PBF-LB systems caused by, for example, thermal lensing due to dirt on or degradation of the optics. Nowadays it is customary for the stability of the focal point position to only be measured (and corrected for, if focus shift is detected) during the 6- or 12-monthly machine maintenance. Utilizing process monitoring based on co-axial photodiodes provides a means to detect possible deviations in the process or machine hardware even during a build job. Recent studies by Stutzman [114] and Reijonen [115] have also shown that the photodiode signal response is sensitive to the shielding gas flow conditions in the PBF-LB process. This finding paves the way for the utilization of MPM to monitor the shielding gas flow conditions in the build chamber, which will be an extremely important process signature to monitor in the future, as this thesis established that the shielding gas flow parameter is a major contributor to the intra- and inter-machine variation in part properties.

The other process monitoring method investigated was powder bed imaging using a contact image sensor (CIS). It was shown that various types of anomalies in the powder bed could be identified from the images. These included spatter re-depositions, powder depletion on part surfaces, features of the part curling up from the powder bed, scratches on the powder bed caused by a damaged re-coater blade, features breaking off from the part due to re-coater collision, and other types of disturbances to the powder bed caused by contact between the re-coater blade and a part feature. Specifically, in this thesis the focus was on quantifying powder bed disturbances caused by collisions between a thin feature and the re-coater blade by utilizing the short focal distance of the sensor. Areas that are closer or further away from the sensor focus (set to the nominal powder bed surface) show as blurred areas in the image. The magnitude of blur can be automatically quantified from the images utilizing, for example, the Laplacian focus measure introduced in [104]. Such a

numerical metric can be used to monitor the effective powder layer thickness during the PBF-LB process and detect variations in the powder bed caused by, for example, re-coater collision. A study by Yang et al. [107] also showed that the same CIS-based process monitoring setup can be used to correlate features of the laser-melted part surface to part density, when analyzed at multiple scales by performing wavelet transformation on the images. Similarly, other types of image processing schemes could be developed to quantify and automatically identify the different types of variations seen in the images obtained by the CIS-based process monitoring setup.

Powder bed imaging itself is nothing new in the PBF-LB process, however the usage of contact image sensors mounted on the re-coater blade to acquire images offers a few key practical advantages over cameras placed at a distance and off-axis: constant illumination conditions, high resolution for an extended area, and an axial view of the powder bed. In terms of advancement in the use of contact image sensors for powder bed imaging, the setup introduced in this thesis enables high-resolution (1200 dpi, 21 µm/pixel) images of a 184 mm wide area at the powder bed to be acquired, and most importantly at a practically relevant linear re-coating speed of 95 mm/s with a compact footprint (18 mm sensor width) without blocking any active build area in the process. This makes it possible to retrofit the setup to a commercial PBF-LB machine used for production, not solely for research purposes.

5.4 Synthesis

Based on the results and analysis of the research conducted in this thesis and the discussion of these results in relation to prior knowledge, a synthesis on the impacts of the *machine architecture-defined* process parameters on the PBF-LB process can be drawn. This is presented in **Table 11**.

Table 11. Summary of the impacts of the machine architecture-defined process parameters on the PBF-LB process, their contribution to variability, practical recommendations for control, and the potential of the process monitoring methods studied to capture the induced variations.

Parameter	Impact on process	Type of variability	Recommended tolerance for control	Process monitoring
Shielding gas flow speed and configu-ration	Insufficient gas flow rate leads to insufficient removal of the vapor plume and other process by-products. The plume attenuates and scatters the laser beam, causing loss of penetration and wider and more unstable melt pools, ultimately leading to lack of fusion. Other process by-products landing on the build area alter the local melting conditions and may cause lack of fusion.	May vary within a build, between builds, and between machines.	Maintain gas flow speed above threshold** at all locations on the building platform. Ensure laminar flow without re-circulation zones above the build area.	Variations in shielding gas flow conditions can be detected with photodiode-based melt pool monitoring [114][115].
Re-coater blade type	Controls powder spreading and may result in powder bed disturbances due to contact between the re-coater blade and the part being built, ultimately leading to porosity, reduced dimensional accuracy, poor surface finish, or even build failure. The nature of the impact depends on the combination of re-coater blade type, part features, and orientation.	May vary between builds* and between machines.	Discrete (fixed blade material and tip profile).	Variations in the spread powder layer, caused by re-coater collisions, can be detected with contact-image sensor-based powder bed imaging.
Focal point position	A shift in the focal point position in either direction will alter the effective beam diameter at the work plane. An increase in the effective beam diameter leads to loss of penetration, leading ultimately to lack of fusion.	May vary within a build, between builds, and between machines.	±30% of the Rayleigh length of the laser beam used.	Variations in the focal point position can be detected with melt pool monitoring.

*In some PBF-LB machines various re-coater blade types can be used by the operator.
**Threshold above which melt pool penetration and width remain stable. Threshold to be identified for the given machine model and laser melting parameters used.

Post-process heat treatments, especially hot-isostatic pressing, were shown to be effective in reducing variation in some (but not all) mechanical properties of 316L stainless steel due to reduction of porosity and homogenization of the microstructure. However, this results in loss of the unique as-built PBF-LB 316L microstructure, and the exceptionally high yield strength associated with it.

6 Summary/Conclusions

High variation in the mechanical properties of parts produced using PBF-LB AM is a major hindrance to the advancement and wider adoption of this manufacturing technology. Addressing this topic is a necessity for this technology to fulfill its potential of being the next paradigm shift in manufacturing; truly digitalized, decentralized, customizable, on-demand manufacturing, with associated unparalleled design freedom in terms of part geometries.

The objectives of this thesis were to 1) identify the root causes of the observed variation in the properties by establishing the effects of *machine architecture-defined* parameters on the process, 2) study the potential to reduce the variation using standardized post-process heat treatments, and 3) develop in-situ process monitoring methods capable of detecting variations in the process.

Based on the experiments described in this thesis and relating these findings to those made in other studies, the following specific conclusions can be drawn.

Objective 1:

- Shielding gas flow is an essential parameter in the PBF-LB process. Reducing the shielding gas flow rate below a certain threshold causes significant loss of penetration leading to lack-of-fusion porosity. Melt pool width and instability are also increased. The root cause is insufficient removal of the vapor plume. When the shielding gas flow lacks sufficient momentum to effectively remove the vapor plume from the beam path the plume will extensively attenuate and scatter the laser, reducing the energy density that reaches the material.
- When manufacturing bulk material without any intricate geometrical features, the use of either a soft or hard re-coater blade results in stable powder bed conditions and equally low porosity. However, significant differences in porosity and processability arose when building thin walls (<1.0 mm in thickness) and overhanging features (<45° inclination). Furthermore, the orientation of these features in relation to the re-coating direction and the re-coater blade type used had a significant impact. For the thin walls, the soft blade had better processability and resulted in

lower porosity and better surface finish and dimensional accuracy. For the overhangs, the hard blade resulted in lower porosity and better surface finish and dimensional accuracy. However, the hard blade was unable to build the overhangs to extended distances due to collision between the protruding feature and the unyielding hard blade, while the soft blade was able to process the features, but with low quality.

- Deviation in the focal point position by more than ±1 mm (±30% of the Rayleigh length of the beam used) from the work plane causes significant reduction in melt pool penetration and a minor increase in melt pool width. The penetration decreases gradually the more the focal point position deviates from the beam-material interaction plane in either direction. With the beam and laser parameters used in this study, a focus shift of +5 mm started to result in a significant increase in porosity caused by lack of fusion.

Objective 2:

- When cross-testing PBF-LB machines and powders with 316L material, the coefficient of variation in tensile strength was quite small, moderate for tensile elongation, and already rather high (~10%) for impact toughness. In terms of fatigue life, it has previously been shown [60] that the variability can be extremely high. The more dynamic the loading conditions, the more variation in mechanical properties can be expected. This is caused by high variability in the shapes, sizes, and locations of internal defects in PBF-LB manufactured parts (when excluding the effect of surface roughness), which dictate performance in dynamic loading conditions. It was shown that post-process heat treatment using HIP effectively re-crystallizes and homogenizes the microstructure, reduces internal porosity, and hence reduces variability in all other properties studied except elongation, due to the coarsening of oxide inclusions during HIP. However, the reduction in variability gained is associated with other drawbacks. HIP destroys the sub-micron-sized cellular dislocation network and other unique hierarchically heterogeneous features in the PBF-LB microstructure and causes coarsening of oxide inclusions. This results in a significant reduction in the absolute yield strength and impact toughness of the material.

Objective 3:

- Melt pool monitoring based on co-axial photodiodes and powder bed monitoring based on contact image sensors can be used to continuously monitor the PBF-LB process and detect unwanted variations in

processing conditions that may lead to defect formation. The TED^* metric introduced in this thesis, utilizing the MPM signal, showed strong linear correlation with the resulting beam size-normalized melt pool penetration and width for a range of input laser parameter conditions while $\Delta H/hs < 12$. The MPM signals were also able to capture the trend of shifting focal point position. Various powder bed disturbances could be identified in the images obtained with the contact-image sensor. Quantification of the powder bed disturbances, caused by collisions between a thin feature and the re-coater blade, from the images was demonstrated using the Laplacian focus measure introduced in [104].

To control the variability in output properties of the PBF-LB process requires control of the variation of the input parameters. The *machine architecture-defined* process parameters shielding gas flow rate and configuration, re-coater blade type, and (stability of) the focal point position in relation to the work plane were identified as essential parameters. Their set values and acceptable variation limits should be included in additive manufacturing procedure specifications or other process control measures aimed at assuring repeatability and stability of properties in parts produced using PBF-LB AM. These parameters should also be routinely reported in the Methods sections of scientific PBF-LB studies to allow for replication. Standardized post-process heat treatments may provide some reduction in the variability in properties, however they are associated with other drawbacks. Process monitoring utilizing co-axial photodiode-based melt pool monitoring and contact-image sensor-based powder bed imaging offer effective means to directly and continuously monitor the state of the actual fundamental unit processes in the PBF-LB process: the spreading of the powder layer and the selective laser melting of it. The continuous, alternating execution of these two fundamental unit processes in a stable and repeatable manner is key to additively manufacturing 3-dimensional parts to high quality using the PBF-LB process.

The experiments described in this thesis were conducted on only one material (316L stainless steel), which is a limitation of the study. Further studies should verify whether the findings hold for a variety of alloys typically processed in PBF-LB AM. In this thesis it was established that the three *machine architecture-defined* process parameters studied have a significant impact on part porosity. The impact on mechanical properties, both static and dynamic, should be further studied. The potential of utilizing process monitoring, especially the normalized thermal energy density from the photodiode signal introduced in this thesis, as a means for quality control should be further explored.

Acknowledgements

I would like to express my deepest gratitude to my supervisor Professor Antti Salminen, who has been providing his excellent guidance on my laser materials processing research path already for a decade – starting from my B.Sc. and M.Sc. theses back in Lappeenranta University of Technology and now culminating in the doctoral thesis at the University of Turku. I would also like to express my gratitude to my supervisors Sini Metsä-Kortelainen and Heli Helaakoski at VTT Technical Research Centre of Finland Ltd. for their continuous support and encouragement.

I am grateful to Asst. Prof. Jaime Berez and Prof. Johannes Henrich Schleifenbaum for pre-examination of the thesis and Prof. Milan Brandt for agreeing to act as the opponent in the public defense.

The research that constitutes this thesis was conducted at VTT as part of the Advanced Manufacturing Technologies research group, where I have had the privilege to work on a variety of interesting and challenging research projects on metal additive manufacturing. I would like to thank all the research colleagues at VTT that I have had the opportunity to work with along the years. In particular, I would like to thank Atte Antikainen for valuable discussions on research and everything else, Kimmo Ruusuvuori for all the excellent help and guidance in laboratory work related to additive manufacturing and Seija Kivi and Hanna Iitti for metallography. I would also like to thank Jukka Kuva from GTK for xCT scanning. A special thanks to all the laboratory technicians, engineers and researchers who have contributed to the experiments of this thesis.

I am grateful to all my co-authors, Roy Björkstrand and Mika Salmi from Aalto University, Pasi Puukko, Zaiqing Que, Alejandro Revuelta and Tuomas Riipinen from VTT for their valuable contributions to the scientific publications of the thesis.

The financial support of VTT Technical Research Centre of Finland Ltd. is gratefully acknowledged. I would also like to thank Walter Ahlström Foundation for the financial support towards finalizing this thesis.

9.12.2024
Joni Reijonen

List of References

[1] ISO/ASTM 52900:2021. Additive manufacturing. General principles. Fundamentals and vocabulary, 2021.

[2] H. Kodama, Stereoscopic figure drawing device, JPS56144478A, 1980.

[3] C. Hull, Apparatus for production of three-dimensional objects by stereolithography, US4575330A, 1984.

[4] C. Deckard, Method and apparatus for producing parts by selective sintering, US4863538A, 1986.

[5] P. Haase, Selective laser sintering of metal powders, The University of Texas at Austin, 1989.

[6] J.A. Manriquez-Frayre, D.L. Bourell, Selective Laser Sintering of Binary Metallic Powder, in: Proc. 1st Solid Free. Fabr. Symp., 1990: pp. 99–106.

[7] W. Meiners, K. Wissenbach, A. Gasser, Selective Laser Sintering at Melting Temperature, EP0946325A1, 1996.

[8] B. Van der Schueren, J.-P. Kruth, Laser based selective metal powder sintering: a feasibility study, Proc. Laser Assist. Net Shape Eng. (1994) 517–523.

[9] R.H. Morgan, A. Papworth, C. Sutcliffe, P. Fox, B. O'Neill, Direct metal laser re-melting of 316L stainless steel powder. Part 2: analysis of cubic primitives, in: Proc. 12th Solid Free Form Fabr. Symp., 2001: pp. 283–295.

[10] E. Santos, F. Abe, Y. Kitamura, K. Osakada, M. Shiomi, Mechanical Properties of Pure Titanium Models Processed by Selective Laser Melting, in: Proc. 13th Solid Free Form Fabr. Symp., 2002: pp. 180–186.

[11] G.N. Levy, R. Schindel, J.P. Kruth, Rapid manufacturing and rapid tooling with layer manufacturing (LM) technologies, state of the art and future perspectives, CIRP Ann. - Manuf. Technol. 52 (2003) 589–609. https://doi.org/10.1016/S0007-8506(07)60206-6.

[12] S. Das, J.J. Beaman, M.W.D.L. Bourell, Direct laser freeform fabrication of high performance metal components, Rapid Prototyp. J. 4 (1998) 112–117. https://doi.org/10.1108/13552549810222939.

[13] R.H. Morgan, A.J. Papworth, C. Sutcliffe, P. Fox, W. O'Neill, High density net shape components by direct laser re-melting of single-phase powders, J. Mater. Sci. 37 (2002) 3093–3100. https://doi.org/10.1023/A:1016185606642.

[14] T. Syvänen, M. Heugel, R. Domröse, Diode pumped fiber laser in direct metal laser sintering (DMLS) process, in: Proc. ICALEO 2004 - 23rd Int. Congr. Appl. Laser Electro-Optics, 2004.

[15] C.-J. Kong, C.J. Tuck, I.A. Ashcroft, R.D. Wildman, R. Hague, High density TI6AL4V via SLM processing: Microstructure and mechanical properties, in: Proc. 22nd Solid Free. Fabr. Symp., 2011: pp. 475–483.

[16] E.C. Santos, K. Osakada, M. Shiomi, Y. Kitamura, F. Abe, Microstructure and mechanical properties of pure titanium models fabricated by selective laser melting, Proc. Inst. Mech. Eng. Part C J. Mech. Eng. Sci. 218 (2004) 711–719.

[17] M. Latikka, J. Kotila, T. Syvänen, O. Nyrhilä, J. Hänninen, Direct Metal Laser Sintering – New Possibilities In Part Manufacturing, in: Proc. Euro Powder Metall. Congr. Exhib. Euro PM 2005, 2005.

[18] K. Kempen, L. Thijs, B. Vrancken, S. Buls, J. Van Humbeeck, J.P. Kruth, Producing crack-free, high density M2 HSS parts by Selective Laser Melting: Pre-heating the baseplate, in: Proc. 24th Solid Free. Fabr. Symp., 2013: pp. 131–139.

[19] R. Rothfelder, F. Nahr, L. Chechik, A Brief History of the Progress of Laser Powder Bed Fusion of Metals in Europe, J. Manuf. Sci. Eng. 145 (2023) 1–11. https://doi.org/10.1115/1.4062788.

[20] H. Schleifenbaum, W. Meiners, K. Wissenbach, C. Hinke, High power selective laser melting: A new approach for individualized series production, in: ICALEO 2009 - 28th Int. Congr. Appl. Lasers Electro-Optics, 2009. https://doi.org/10.2351/1.5061585.

[21] J.P. Kruth, L. Froyen, J. Van Vaerenbergh, P. Mercelis, M. Rombouts, B. Lauwers, Selective laser melting of iron-based powder, J. Mater. Process. Technol. 149 (2004) 616–622. https://doi.org/10.1016/j.jmatprotec.2003.11.051.

[22] I. Yadroitsev, P. Bertrand, I. Smurov, Parametric analysis of the selective laser melting process, Appl. Surf. Sci. 253 (2007) 8064–8069. https://doi.org/10.1016/j.apsusc.2007.02.088.

[23] J.P. Kruth, P. Mercelis, J. Van Vaerenbergh, L. Froyen, M. Rombouts, Binding mechanisms in selective laser sintering and selective laser melting, Rapid Prototyp. J. 11 (2005) 26–36. https://doi.org/10.1108/13552540510573365.

[24] B. Vandenbroucke, J.P. Kruth, Selective laser melting of biocompatible metals for rapid manufacturing of medical parts, Rapid Prototyp. J. 13 (2007) 196–203. https://doi.org/10.1108/13552540710776142.

[25] Y.M. Wang, T. Voisin, J.C. McKeown, N.P. Ye, Z. Calta, Z. Zeng, Y. Zhang, W. Chen, T.T. Roehling, R.T. Ott, K. Santala, P.J. Depond, M.J. Matthews, A. V Hamza, T. Zhu, Additively manufactured hierarchical stainless steels with high strength and ductility, Nat. Mater. 17 (2017) 63–71. https://doi.org/10.1038/nmat5021.

[26] L. Liu, Q. Ding, Y. Zhong, J. Zou, J. Wu, Y.L. Chiu, J. Li, Z. Zhang, Q. Yu, Z. Shen, Dislocation network in additive manufactured steel breaks strength–ductility trade-off, Mater. Today. 21 (2018) 354–361. https://doi.org/10.1016/j.mattod.2017.11.004.

[27] D. Montgomery, Introduction To Statistical Quality Control, 6th Editio, John Wiley & Sons, 2009.

[28] T. Prater, W. Tilson, Z. Jones, Characterization of Machine Variability and Progressive Heat Treatment in Selective Laser Melting of Inconel 718, in: 62nd JANNAF Propuls. Meet., 2015.

[29] C.U. Brown, G. Jacob, M. Stoudt, S. Moylan, J. Slotwinski, A. Donmez, Interlaboratory Study for Nickel Alloy 625 Made by Laser Powder Bed Fusion to Quantify Mechanical Property Variability, J. Mater. Eng. Perform. 25 (2016) 3390–3397. https://doi.org/10.1007/s11665-016-2169-2.

[30] W.H. Kan, L.N.S. Chiu, C.V.S. Lim, Y. Zhu, Y. Tian, D. Jiang, A. Huang, A critical review on the effects of process-induced porosity on the mechanical properties of alloys fabricated by laser powder bed fusion, J. Mater. Sci. 57 (2022) 9818–9865. https://doi.org/10.1007/s10853-022-06990-7.

[31] S.A. Khairallah, A.T. Anderson, A. Rubenchik, W.E. King, Laser powder-bed fusion additive manufacturing: Physics of complex melt flow and formation mechanisms of pores, spatter, and denudation zones, Acta Mater. 108 (2016) 36–45. https://doi.org/10.1016/j.actamat.2016.02.014.

[32] J. V. Gordon, S.P. Narra, R.W. Cunningham, H. Liu, H. Chen, R.M. Suter, J.L. Beuth, A.D. Rollett, Defect structure process maps for laser powder bed fusion additive manufacturing, Addit. Manuf. 36 (2020) 101552. https://doi.org/10.1016/j.addma.2020.101552.

[33] D.E. Hardt, Manufacturing processes and process control, Lect. Notes from Subj. MIT 2.830 Control Manuf. Process. (1996) 1–6.

[34] D.E. Hardt, Modeling and Control of Manufacturing Processes: Getting More Involved, J. Dyn. Sys., Meas., Control. 115 (1993) 291–300. https://doi.org/doi.org/10.1115/1.2899069.

[35] S. Chowdhury, N. Yadaiah, C. Prakash, S. Ramakrishna, S. Dixit, L.R. Gupta, D. Buddhi, Laser powder bed fusion: a state-of-the-art review of the technology, materials, properties & defects,

and numerical modelling, J. Mater. Res. Technol. 20 (2022) 2109–2172. https://doi.org/10.1016/j.jmrt.2022.07.121.
[36] F. Ceccanti, A. Giorgetti, G. Arcidiacono, P. Citti, Laser Powder Bed Fusion: A Review on the Design Constraints, IOP Conf. Ser. Mater. Sci. Eng. 1038 (2021) 012065. https://doi.org/10.1088/1757-899x/1038/1/012065.
[37] J.P. Oliveira, A.D. LaLonde, J. Ma, Processing parameters in laser powder bed fusion metal additive manufacturing, Mater. Des. 193 (2020) 1–12. https://doi.org/10.1016/j.matdes.2020.108762.
[38] L. Wang, Y. Zhang, H.Y. Chia, W. Yan, Mechanism of keyhole pore formation in metal additive manufacturing, Npj Comput. Mater. 8 (2022). https://doi.org/10.1038/s41524-022-00699-6.
[39] M. Tang, P.C. Pistorius, J.L. Beuth, Prediction of lack-of-fusion porosity for powder bed fusion, Addit. Manuf. 14 (2017) 39–48. https://doi.org/10.1016/j.addma.2016.12.001.
[40] W. Zhang, W. Hou, L. Deike, C. Arnold, Understanding the Rayleigh instability in humping phenomenon during laser powder bed fusion process, Int. J. Extrem. Manuf. 4 (2022). https://doi.org/10.1088/2631-7990/ac466d.
[41] I. Yadroitsev, A. Gusarov, I. Yadroitsava, I. Smurov, Single track formation in selective laser melting of metal powders, J. Mater. Process. Technol. 210 (2010) 1624–1631. https://doi.org/10.1016/j.jmatprotec.2010.05.010.
[42] N. Ahmed, I. Barsoum, G. Haidemenopoulos, R.K.A. Al-Rub, Process parameter selection and optimization of laser powder bed fusion for 316L stainless steel: A review, J. Manuf. Process. 75 (2022) 415–434. https://doi.org/10.1016/j.jmapro.2021.12.064.
[43] SAE International, AMS7003. Aerospace material specification. Laser Powder Bed Fusion Process., 2018.
[44] A. Keshavarzkermani, E. Marzbanrad, R. Esmaeilizadeh, Y. Mahmoodkhani, U. Ali, P.D. Enrique, N.Y. Zhou, A. Bonakdar, E. Toyserkani, An investigation into the effect of process parameters on melt pool geometry, cell spacing, and grain refinement during laser powder bed fusion, Opt. Laser Technol. 116 (2019) 83–91. https://doi.org/10.1016/j.optlastec.2019.03.012.
[45] J.J.S. Dilip, S. Zhang, C. Teng, K. Zeng, C. Robinson, D. Pal, B. Stucker, Influence of processing parameters on the evolution of melt pool, porosity, and microstructures in Ti-6Al-4V alloy parts fabricated by selective laser melting, Prog. Addit. Manuf. 2 (2017) 157–167. https://doi.org/10.1007/s40964-017-0030-2.
[46] A. du Plessis, Effects of process parameters on porosity in laser powder bed fusion revealed by X-ray tomography, Addit. Manuf. 30 (2019) 100871. https://doi.org/10.1016/j.addma.2019.100871.
[47] A. Leicht, M. Rashidi, U. Klement, E. Hryha, Effect of process parameters on the microstructure, tensile strength and productivity of 316L parts produced by laser powder bed fusion, Mater. Charact. 159 (2020) 110016. https://doi.org/10.1016/j.matchar.2019.110016.
[48] R. Esmaeilizadeh, A. Keshavarzkermani, U. Ali, B. Behravesh, A. Bonakdar, H. Jahed, E. Toyserkani, On the effect of laser powder-bed fusion process parameters on quasi-static and fatigue behaviour of Hastelloy X: A microstructure/defect interaction study, Addit. Manuf. 38 (2021) 101805. https://doi.org/10.1016/j.addma.2020.101805.
[49] S. Siddique, M. Imran, E. Wycisk, C. Emmelmann, F. Walther, Influence of process-induced microstructure and imperfections on mechanical properties of AlSi12 processed by selective laser melting, J. Mater. Process. Technol. 221 (2015) 205–213. https://doi.org/10.1016/j.jmatprotec.2015.02.023.
[50] J. Liu, G. Li, Q. Sun, H. Li, J. Sun, X. Wang, Understanding the effect of scanning strategies on the microstructure and crystallographic texture of Ti-6Al-4V alloy manufactured by laser powder bed fusion, J. Mater. Process. Technol. 299 (2022). https://doi.org/10.1016/j.jmatprotec.2021.117366.
[51] ASME, Boiler and Pressure Vessel Code Section IX, 2021.
[52] S.A.M. Tofail, E.P. Koumoulos, A. Bandyopadhyay, S. Bose, L. O'Donoghue, C. Charitidis, Additive manufacturing: scientific and technological challenges, market uptake and opportunities, Mater. Today. 21 (2018) 22–37. https://doi.org/10.1016/j.mattod.2017.07.001.

[53] EN ISO 15607:2019. Specification and qualification of welding procedures for metallic materials. General rules., 2019.
[54] ISO/ASTM 52904:2019. Additive Manufacturing – Process Characteristics and Performance: Practice for Metal Powder Bed Fusion Process to Meet Critical Applications, 2019.
[55] A.L.R. Prathyusha, G. Raghu Babu, A review on additive manufacturing and topology optimization process for weight reduction studies in various industrial applications, Mater. Today Proc. 62 (2022) 109–117. https://doi.org/10.1016/j.matpr.2022.02.604.
[56] L. Dowling, J. Kennedy, S. O'Shaughnessy, D. Trimble, A review of critical repeatability and reproducibility issues in powder bed fusion, Mater. Des. 186 (2020) 108346. https://doi.org/10.1016/j.matdes.2019.108346.
[57] S. Siddique, M. Imran, M. Rauer, M. Kaloudis, E. Wycisk, C. Emmelmann, F. Walther, Computed tomography for characterization of fatigue performance of selective laser melted parts, Mater. Des. 83 (2015) 661–669. https://doi.org/10.1016/j.matdes.2015.06.063.
[58] T. Voisin, N.P. Calta, S.A. Khairallah, J.B. Forien, L. Balogh, R.W. Cunningham, A.D. Rollett, Y.M. Wang, Defects-dictated tensile properties of selective laser melted Ti-6Al-4V, Mater. Des. 158 (2018) 113–126. https://doi.org/10.1016/j.matdes.2018.08.004.
[59] T.P. Moran, D.H. Warner, A. Soltani-Tehrani, N. Shamsaei, N. Phan, Spatial inhomogeneity of build defects across the build plate in laser powder bed fusion, Addit. Manuf. 47 (2021) 102333. https://doi.org/10.1016/j.addma.2021.102333.
[60] J. Berez, L. Sheridan, C. Saldaña, Extreme variation in fatigue: Fatigue life prediction and dependence on build volume location in laser powder bed fusion of 17-4 stainless steel, Int. J. Fatigue. 158 (2022) 1–14. https://doi.org/10.1016/j.ijfatigue.2022.106737.
[61] Y. Murakami, M. Endo, Effects of defects, inclusions and inhomogeneities on fatigue strength, Int. J. Fatigue. 16 (1994) 163–182. https://doi.org//10.1016/0142-1123(94)90001-9.
[62] N. Sanaei, A. Fatemi, N. Phan, Defect characteristics and analysis of their variability in metal L-PBF additive manufacturing, Mater. Des. 182 (2019) 108091. https://doi.org/10.1016/j.matdes.2019.108091.
[63] F. Calignano, V. Mercurio, An overview of the impact of additive manufacturing on supply chain, reshoring, and sustainability, Clean. Logist. Supply Chain. 7 (2023) 100103. https://doi.org/10.1016/j.clscn.2023.100103.
[64] M.C. Sow, T. De Terris, O. Castelnau, Z. Hamouche, F. Coste, R. Fabbro, P. Peyre, Influence of beam diameter on Laser Powder Bed Fusion (L-PBF) process, Addit. Manuf. 36 (2020) 101532. https://doi.org/10.1016/j.addma.2020.101532.
[65] J. Grünewald, V. Blickle, M. Allenberg-Rabe, P. Wagenblast, K. Wudy, Flexible and highly dynamic beam shaping for Laser-Based Powder Bed Fusion of metals, Procedia CIRP. 111 (2022) 65–70. https://doi.org/10.1016/j.procir.2022.08.124.
[66] V. Holla, P. Kopp, J. Grünewald, K. Wudy, S. Kollmannsberger, Laser beam shape optimization in powder bed fusion of metals, Addit. Manuf. 72 (2023). https://doi.org/10.1016/j.addma.2023.103609.
[67] F. Galbusera, L. Caprio, B. Previtali, A.G. Demir, The influence of novel beam shapes on melt pool shape and mechanical properties of LPBF produced Al-alloy, J. Manuf. Process. 85 (2023) 1024–1036. https://doi.org/10.1016/j.jmapro.2022.12.007.
[68] J. Bi, L. Wu, S. Li, Z. Yang, X. Jia, M.D. Starostenkov, G. Dong, Beam shaping technology and its application in metal laser additive manufacturing: A review, J. Mater. Res. Technol. 26 (2023) 4606–4628. https://doi.org/10.1016/j.jmrt.2023.08.037.
[69] S. Patel, H. Chen, M. Vlasea, Y. Zou, The influence of beam focus during laser powder bed fusion of a high reflectivity aluminium alloy — AlSi10Mg, Addit. Manuf. 59 (2022) 103112. https://doi.org/10.1016/j.addma.2022.103112.
[70] G.E. Bean, D.B. Witkin, T.D. McLouth, D.N. Patel, R.J. Zaldivar, Effect of laser focus shift on surface quality and density of Inconel 718 parts produced via selective laser melting, Addit. Manuf. 22 (2018) 207–215. https://doi.org/10.1016/j.addma.2018.04.024.

[71] A. Paraschiv, G. Matache, M.R. Condruz, T.F. Frigioescu, I. Ionică, The influence of laser defocusing in selective laser melted in 625, Materials (Basel). 14 (2021) 1–14. https://doi.org/10.3390/ma14133447.
[72] J. Metelkova, Y. Kinds, K. Kempen, C. de Formanoir, A. Witvrouw, B. Van Hooreweder, On the influence of laser defocusing in Selective Laser Melting of 316L, Addit. Manuf. 23 (2018) 161–169. https://doi.org/10.1016/j.addma.2018.08.006.
[73] L.C. Capozzi, A. Sivo, E. Bassini, Powder spreading and spreadability in the additive manufacturing of metallic materials: A critical review, J. Mater. Process. Technol. 308 (2022) 117706. https://doi.org/10.1016/j.jmatprotec.2022.117706.
[74] M.Y. Shaheen, A.R. Thornton, S. Luding, T. Weinhart, The influence of material and process parameters on powder spreading in additive manufacturing, Powder Technol. 383 (2021) 564–583. https://doi.org/10.1016/j.powtec.2021.01.058.
[75] D. Jansen, T. Hanemann, M. Radek, A. Rota, J. Schröpfer, M. Heilmaier, Development of actual powder layer height depending on nominal layer thicknesses and selection of laser parameters, J. Mater. Process. Technol. 298 (2021). https://doi.org/10.1016/j.jmatprotec.2021.117305.
[76] H. Fox, A.B. Kamaraj, D. Drake, Investigating the effect of powder recoater blade material on the mechanical properties of parts manufactured using a powder-bed fusion process, Manuf. Lett. 00 (2022) 561–568. https://doi.org/10.1016/j.mfglet.2022.07.071.
[77] M. Dańa, I. Zetková, P. Hanzl, The influence of a ceramic recoater blade on 3D printing using direct metal laser sintering, Manuf. Technol. 19 (2019) 23–28. https://doi.org/10.21062/ujep/239.2019/a/1213-2489/mt/19/1/23.
[78] S.A.R. Shamsdini, M.H. Ghoncheh, M. Mohammadi, Effect of recoater-blade type on the mechanical properties and microstructure of additively manufactured maraging steels, Mater. Sci. Eng. A. 812 (2021) 141104. https://doi.org/10.1016/j.msea.2021.141104.
[79] B. Ferrar, L. Mullen, E. Jones, R. Stamp, C.J. Sutcliffe, Gas flow effects on selective laser melting (SLM) manufacturing performance, J. Mater. Process. Technol. 212 (2012) 355–364. https://doi.org/10.1016/j.jmatprotec.2011.09.020.
[80] A. Ladewig, G. Schlick, M. Fisser, V. Schulze, U. Glatzel, Influence of the shielding gas flow on the removal of process by-products in the selective laser melting process, Addit. Manuf. 10 (2016) 1–9. https://doi.org/10.1016/j.addma.2016.01.004.
[81] A. Bin Anwar, Q.C. Pham, Selective laser melting of AlSi10Mg: Effects of scan direction, part placement and inert gas flow velocity on tensile strength, J. Mater. Process. Technol. 240 (2017) 388–396. https://doi.org/10.1016/j.jmatprotec.2016.10.015.
[82] P. Shcheglov, Study of Vapour-Plasma Plume during High Power Fiber Laser Beam Influence on Metals, BAM Federal Institute for Materials Research and Testing, 2012.
[83] A.T. Sutton, C.S. Kriewall, M.C. Leu, J.W. Newkirk, B. Brown, Characterization of laser spatter and condensate generated during the selective laser melting of 304L stainless steel powder, Addit. Manuf. 31 (2020) 100904. https://doi.org/10.1016/j.addma.2019.100904.
[84] Z. Snow, L. Scime, A. Ziabari, B. Fisher, V. Paquit, Observation of spatter-induced stochastic lack-of-fusion in laser powder bed fusion using in situ process monitoring, Addit. Manuf. 61 (2023) 103298. https://doi.org/10.1016/j.addma.2022.103298.
[85] B. Roidl, T. Fauner, Continuous Improvement in Gas Flow Design, 2021.
[86] X. Zhang, B. Cheng, C. Tuffile, Simulation study of the spatter removal process and optimization design of gas flow system in laser powder bed fusion, Addit. Manuf. 32 (2020). https://doi.org/10.1016/j.addma.2020.101049.
[87] P. Bidare, I. Bitharas, R.M. Ward, M.M. Attallah, A.J. Moore, Fluid and particle dynamics in laser powder bed fusion, Acta Mater. 142 (2018) 107–120. https://doi.org/10.1016/j.actamat.2017.09.051.
[88] L.R. Goossens, Y. Kinds, J.-P. Kruth, B. Van Hooreweder, on the Influence of Thermal Lensing During Selective Laser, in: Proc. 29th Solid Free. Fabr. Symp., 2018: pp. 2267–2274.

[89] M.J. Matthews, G. Guss, S.A. Khairallah, A.M. Rubenchik, P.J. Depond, W.E. King, Denudation of metal powder layers in laser powder bed fusion processes, Acta Mater. 114 (2016) 33–42. https://doi.org/http://dx.doi.org/10.1016/j.actamat.2016.05.017.

[90] E. Kivirasi, H. Piili, P. Ylander, J. Kotila, An approach for a better understanding of spattering phenomena: Spatter analysis system development for direct metal laser sintering, in: Proc. Euro PM 2018 Congr. Exhib., 2018.

[91] Y. Kawahito, M. Mizutani, S. Katayama, Elucidation of high-power fibre laser welding phenomena of stainless steel and effect of factors on weld geometry, J. Phys. D. Appl. Phys. 40 (2007) 5854–5859. https://doi.org/10.1088/0022-3727/40/19/009.

[92] M.M.A. Khan, L. Romoli, G. Dini, M. Fiaschi, A simplified energy-based model for laser welding of ferritic stainless steels in overlap configurations, CIRP Ann. - Manuf. Technol. 60 (2011) 215–218. https://doi.org/10.1016/j.cirp.2011.03.112.

[93] D.B. Hann, J. Iammi, J. Folkes, A simple methodology for predicting laser-weld properties from material and laser parameters, J. Phys. D. Appl. Phys. 44 (2011). https://doi.org/10.1088/0022-3727/44/44/445401.

[94] L. Thijs, F. Verhaeghe, T. Craeghs, J. Van Humbeeck, J.P. Kruth, A study of the microstructural evolution during selective laser melting of Ti-6Al-4V, Acta Mater. 58 (2010) 3303–3312. https://doi.org/10.1016/j.actamat.2010.02.004.

[95] M. Naderi, J. Weaver, D. Deisenroth, N. Iyyer, R. McCauley, On the Fidelity of the Scaling Laws for Melt Pool Depth Analysis During Laser Powder Bed Fusion, Integr. Mater. Manuf. Innov. 12 (2023) 11–26. https://doi.org/10.1007/s40192-022-00289-w.

[96] J.S. Weaver, J.C. Heigel, B.M. Lane, Laser spot size and scaling laws for laser beam additive manufacturing, J. Manuf. Process. 73 (2022) 26–39. https://doi.org/10.1016/j.jmapro.2021.10.053.

[97] B. Lane, L. Jacquemetton, M. Piltch, D. Beckett, Thermal Calibration of Commercial Melt Pool Monitoring Sensors on a Laser Powder Bed Fusion System, NIST Adv. Manuf. Ser. 100 (2020) 17. https://doi.org/10.6028/NIST.AMS.100-35.

[98] R. McCann, M.A. Obeidi, C. Hughes, É. McCarthy, D.S. Egan, R.K. Vijayaraghavan, A.M. Joshi, V. Acinas Garzon, D.P. Dowling, P.J. McNally, D. Brabazon, In-situ sensing, process monitoring and machine control in Laser Powder Bed Fusion: A review, Addit. Manuf. 45 (2021). https://doi.org/10.1016/j.addma.2021.102058.

[99] M. Abdelrahman, E.W. Reutzel, A.R. Nassar, T.L. Starr, Flaw detection in powder bed fusion using optical imaging, Addit. Manuf. 15 (2017) 1–11. https://doi.org/10.1016/j.addma.2017.02.001.

[100] Q.Y. Lu, N. V. Nguyen, A.J.W. Hum, T. Tran, C.H. Wong, Optical in-situ monitoring and correlation of density and mechanical properties of stainless steel parts produced by selective laser melting process based on varied energy density, J. Mater. Process. Technol. 271 (2019) 520–531. https://doi.org/10.1016/j.jmatprotec.2019.04.026.

[101] F.G. Fischer, N. Birk, L. Rooney, L. Jauer, J.H. Schleifenbaum, Optical process monitoring in Laser Powder Bed Fusion using a recoater-based line camera, Addit. Manuf. 47 (2021) 102218. https://doi.org/10.1016/j.addma.2021.102218.

[102] F.G. Fischer, M.G. Zimmermann, N. Praetzsch, C. Knaak, Monitoring of the powder bed quality in metal additive manufacturing using deep transfer learning, Mater. Des. 222 (2022) 111029. https://doi.org/10.1016/j.matdes.2022.111029.

[103] D.B. Pedersen, E.R. Eiriksson, H. Aanaes, H.N. Hansen, IN-situ monitoring in additive manufacturing using contact image sensors, in: Proc. ASPE/Euspen 2016 Summer Top. Meet. Dimens. Accuracy Surf. Finish Addit. Manuf., 2016: pp. 114–118.

[104] T.-P. Le, M. Seita, A high-resolution and large field-of-view scanner for in-line characterization of powder bed defects during additive manufacturing, Mater. Des. 164 (2019) 107562. https://doi.org/10.1016/j.matdes.2018.107562.

[105] T.-P. Le, X. Wang, K.P. Davidson, J.E. Fronda, M. Seita, Experimental analysis of powder layer quality as a function of feedstock and recoating strategies, Addit. Manuf. 39 (2021) 101890. https://doi.org/10.1016/j.addma.2021.101890.

[106] Q. Lu, M. Grasso, T.P. Le, M. Seita, Predicting build density in L-PBF through in-situ analysis of surface topography using powder bed scanner technology, Addit. Manuf. 51 (2022) 102626. https://doi.org/10.1016/j.addma.2022.102626.
[107] H. Yang, J. Reijonen, A. Revuelta, Multi-resolution Quality Inspection of In-situ Layerwise Builds for Additive Manufacturing, J. Manuf. Sci. Eng. (2023) MANU-22-1587. https://doi.org/10.1115/1.4057013.
[108] P. Mercelis, Control of selective laser sintering and selective laser melting processes, Katholieke Universiteit Leuven, 2007.
[109] T. Craeghs, A Monitoring System for On-line Control of Selective Laser Melting, Katholieke Universiteit Leuven, 2012.
[110] S. Clijsters, T. Craeghs, S. Buls, K. Kempen, J.P. Kruth, In situ quality control of the selective laser melting process using a high-speed, real-time melt pool monitoring system, Int. J. Adv. Manuf. Technol. 75 (2014) 1089–1101. https://doi.org/10.1007/s00170-014-6214-8.
[111] J. Reijonen, A. Revuelta, H.P.N. Nagarajan, Towards data driven quality monitoring: alignment and correlation of photodiode-based co-axial melt pool monitoring signals to part quality in laser powder bed fusion, IOP Conf. Ser. Mater. Sci. Eng. 1296 (2023) 012009. https://doi.org/10.1088/1757-899X/1296/1/012009.
[112] K. Gutknecht, L. Haferkamp, M. Cloots, K. Wegener, Determining process stability of Laser Powder Bed Fusion using pyrometry, Procedia CIRP. 95 (2020) 127–132. https://doi.org/10.1016/j.procir.2020.01.147.
[113] K. Gutknecht, M. Cloots, K. Wegener, Relevance of single channel signals for two-colour pyrometer process monitoring of laser powder bed fusion, Int. J. Mechatronics Manuf. Syst. 14 (2021) 111–127. https://doi.org/10.1504/IJMMS.2021.119152.
[114] C. Stutzman, A. Przyjemski, A.R. Nassar, Effects of gas flow speed on bead geometry and optical emissions during laser powder bed fusion additive manufacturing, Rapid Prototyp. J. 29 (2023) 1386–1394. https://doi.org/10.1108/RPJ-02-2022-0047.
[115] J. Reijonen, Effect of laser parameters and shielding gas flow on co-axial photodiode-based melt pool monitoring signals in laser powder bed fusion, Addit. Manuf. Lett. 11 (2024) 100244. https://doi.org/10.1016/j.addlet.2024.100244.
[116] ASTM E3353:2022. Standard Guide for In-Process Monitoring Using Optical and Thermal Methods for Laser Powder Bed Fusion, 2022.
[117] A.M. Mancisidor, F. Garciandia, M.S. Sebastian, P. Álvarez, J. Díaz, I. Unanue, Reduction of the residual porosity in parts manufactured by selective laser melting using skywriting and high focus offset strategies, Phys. Procedia. 83 (2016) 864–873. https://doi.org/10.1016/j.phpro.2016.08.090.
[118] J. Trapp, A.M. Rubenchik, G. Guss, M.J. Matthews, In situ absorptivity measurements of metallic powders during laser powder-bed fusion additive manufacturing, Appl. Mater. Today. 9 (2017) 341–349. https://doi.org/10.1016/j.apmt.2017.08.006.
[119] G. Jacob, A. Donmez, J. Slotwinski, S. Moylan, Measurement of powder bed density in powder bed fusion additive manufacturing processes, Meas. Sci. Technol. 27 (2016). https://doi.org/10.1088/0957-0233/27/11/115601.
[120] Y. Huang, T.G. Fleming, S.J. Clark, S. Marussi, K. Fezzaa, J. Thiyagalingam, C.L.A. Leung, P.D. Lee, Keyhole fluctuation and pore formation mechanisms during laser powder bed fusion additive manufacturing, Nat. Commun. 13 (2022) 1–11. https://doi.org/10.1038/s41467-022-28694-x.
[121] C.J. Elkins, J. Mireles, H.H. Estrada, D.W. Morgan, H.C. Taylor, R.B. Wicker, Resolving the three-dimensional flow field within commercial metal additive manufacturing machines: Application of experimental Magnetic Resonance Velocimetry, Addit. Manuf. 73 (2023) 103651. https://doi.org/10.1016/j.addma.2023.103651.

[122] Y. Yang, Z. Chen, Z. Liu, H. Wang, Y. Zhang, D. Wang, Influence of shielding gas flow consistency on parts quality consistency during large-scale laser powder bed fusion, Opt. Laser Technol. 158 (2023) 108899. https://doi.org/10.1016/j.optlastec.2022.108899.
[123] Z. Chen, X. Wu, C.H.J. Davies, Process variation in Laser Powder Bed Fusion of Ti-6Al-4V, Addit. Manuf. 41 (2021) 101987. https://doi.org/10.1016/j.addma.2021.101987.
[124] ISO/ASTM 52941:2020. Additive manufacturing. System performance and reliability. Acceptance tests for laser metal powder-bed fusion machines for metallic materials for aerospace application, 2020.
[125] J. Berez, E. Dushaj, E. Jost, C. Saldaña, K. Fu, Measurement of focal plane error in laser powder bed fusion machines, Addit. Manuf. Lett. 9 (2024). https://doi.org/10.1016/j.addlet.2024.100196.
[126] M.L. Montero Sistiaga, S. Nardone, C. Hautfenne, J. Van Humbeeck, Effect of heat treatment of 316L stainless steel prodocued by selective laser melting (SLM), in: Proc. 27th Solid Free. Fabr. Symp., 2016: pp. 558–565.
[127] X. Lou, P.L. Andresen, R.B. Rebak, Oxide inclusions in laser additive manufactured stainless steel and their effects on impact toughness and stress corrosion cracking behavior, J. Nucl. Mater. 499 (2018) 182–190. https://doi.org/10.1016/j.jnucmat.2017.11.036.
[128] P. Deng, M. Karadge, R.B. Rebak, V.K. Gupta, B.C. Prorok, X. Lou, The origin and formation of oxygen inclusions in austenitic stainless steels manufactured by laser powder bed fusion, Addit. Manuf. 35 (2020) 101334. https://doi.org/10.1016/j.addma.2020.101334.

TURUN
YLIOPISTO
UNIVERSITY
OF TURKU

Painosalama, Turku, Finland 2024

ISBN 978-952-02-0021-3 (PRINT)
ISBN 978-952-02-0022-0 (PDF)
ISSN 2736-9390 (Painettu/Print)
ISSN 2736-9684 (Sähköinen/Online)